Hierarchical Self-Assembly Pathways to Colloidal Open Crystals

James Shaw

A thesis presented to the
University of Birmingham
for the degree of
Doctor of Philosophy

School of Chemistry
College of Engineering and Physical Sciences
University of Birmingham
January 2020

Abstract

The self-assembly of colloidal particles provides promising bottom-up routes to three-dimensional structures from simple building blocks. Colloidal open crystals are periodic ordered structures composed of low-coordinated colloidal particles, thus having a maximum density less than what is achieved at close packing. The study of colloidal open crystals has drawn much interest in recent years because of their attractive photonic, phononic and mechanical properties, giving rise to a variety of potential applications.

This thesis extensively uses Brownian dynamics simulations of triblock patchy particles, complemented by a global optimisation method for structure prediction, to establish the versatility of a hierarchical self-assembly scheme encoded in triblock patchy particles to realise a variety of colloidal open crystals via colloidal molecules. The scheme employs a hierarchy of patch-patch interactions programmed into designer triblock patchy particles and tunes the range of these interactions along with the patch sizes. The key to the success of this bottom-up route to yield colloidal crystals is the self-limiting growth of small colloidal clusters, known as colloidal molecules, in the first stage of assembly. The thesis presents a detailed analysis of crystallisation pathways into a variety of colloidal open crystals, namely body-centred cubic, simple cubic and tetrastack crystals and explores any bias towards the cubic or hexagonal polymorph in the case of the tetrastack crystal. In the light of the synthetic realisability of triblock patchy particles and the versatility of the hierarchical self-assembly pathways established here, it is envisaged that the present body of work will underpin novel routes to colloidal open crystals.

Contents

List of Figures

Acknowledgements

My thanks are wholeheartedly given to my Ph.D. supervisor Dr Dwaipayan Chakrabarti. His infectious desire to always be learning something new inspired me to undertake this Ph.D. through which he has been an exceptional mentor, and I have benefited immeasurably from his experience and academic insight. I also owe my thanks to Prof. Roy Johnston, who's encyclopedic knowledge on a wide variety of matter from science to literature and obscure films provided a great deal of insight and joy.

I would also like to thank members of both the Chakrabarti and Johnston research groups who provided a simulating and engaging work environment. In particular I would like to thank Dr Daniel Morphew and Dr Abhishek Rao for their collaborative efforts with much of this work, along with Christopher Avins, Andreas Neophytou and Wesley Flavell for active input into many of the chapters within. Thanks are also due to John Hey, Callum Campbell and Dr Marcus Taylor, who's good humour and support throughout my Ph.D. studies has been invaluable.

Support from the Engineering and Physical Sciences Research Council of the UK and the University of Birmingham for funding, and BlueBEAR and MidPlus+ for HPC facilities is gratefully acknowledged. Finally, I thank Laura for her love, patience and positively.

Chapter 1

Introduction

Whilst colloidal suspensions have been in use for thousands of years in paints and inks discovered in tombs of the ancient Egyptians, the study of colloidal systems, and the origin of the term 'colloid', can be said to have begun in the 19th century with Thomas Graham [1]. In an experiment studying diffusion of particles through parchment, the British Chemist observed that 'true solutions' diffused easily through the parchment, whilst some solutions appeared to be 'glue-like' and did not pass so easily through the parchment. Graham coined the term 'colloids' for the latter, deriving from the Greek word for glue, '$\kappa\acute{o}\lambda\lambda\alpha$'. In modern usage, colloidal dispersions include a wide range of systems, varying in terms of the dispersed phase and the continuous phase. The present body of work is concerned with colloidal suspensions, having solid particles dispersed in a liquid medium. The solid particles are significantly larger in size than what comprises the liquid medium; the particles are typically in the range from 1 to 1000 nm.

Self-assembly refers to the spontaneous emergence of ordered structures or patterns from simpler building blocks [3]. Examples of self-assembly are widespread in nature [4], at times leading to structural hierarchy, for example in bones as illustrated in figure

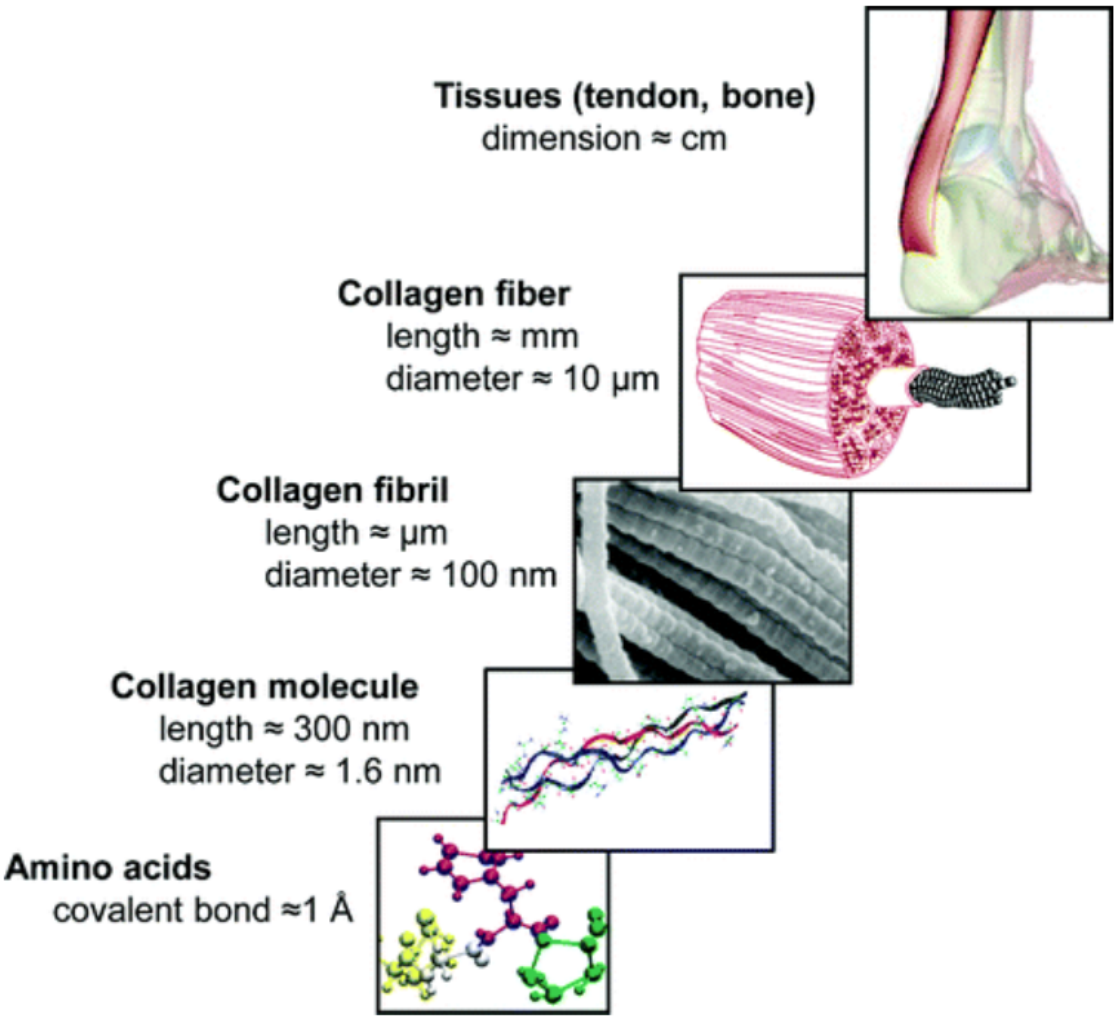

Figure 1.1: Multiple levels of structural hierarchy in bone. Image reproduced from Gautieri *et al.* [2].

1.1. Self-assembly offers a bottom-up route to yield a desired structure if the required information can be encoded in the building blocks of choice for them to self-assemble into the target structure [5] Such a bottom-up approach has the potential of offering a low-cost fabrication route in contrast to 'top-down' approaches, such as micro-robotics, nano- and micro-lithographic methods, all of which are typically time intensive and can be prohibitively expensive for large scale applications [6]. Colloidal particles are promising building blocks for programming self-assembly to yield a target structure

following a bottom-up route because the interactions between colloidal particles can be manipulated [7, 8, 5]. A thorough understanding of the interactions between colloidal particles is critical to the design of building blocks for their programmed self-assembly into a target structure. Encoding hierarchical self-assembly, which often proceeds in stages to produce higher-order structures, in colloidal building blocks is therefore an area of both fundamental and practical interests [9].

1.1 Colloids as Big Atoms

Colloids as "big atoms", a portrayal established by the pioneering work of Einstein and Perrin in the early 20th century [10, 11], have appealed as model systems for studying a range of physical phenomena over the years [12]. For example, colloidal model systems have played a key role in developing our fundamental understanding of thermodynamics and kinetics of phase transitions as well as the glass transition [13, 14, 15, 16, 17]. In a seminal experimental study in 1986 [13], the observation of crystallisation of nearly hard-sphere colloids from a fluid phase at a higher volume fraction, as shown in figure 1.2, firmly established the phenomenon of hard-sphere freezing, originally predicted in computer simulation studies in the 1950s [18, 19]. This experimental validation also lent support to the concept of entropy-driven phase transitions [20], the origin of which dates back to the work of Onsager [21].

The experimental study by Pusey and van Megen realised nearly hard-sphere interactions with sterically stabilised polymethylmethacrylate (PMMA) spheres in the presence of refractive index matching [13]. They investigated a number of samples with different concentrations of the particles. As the concentration increased, there was a transition from the fluid phase to crystal phase through a region having the two phases in coexistence; a glassy state was observed at still higher concentrations, as evident in

Figure 1.2: Several samples of suspensions of nearly hard-sphere colloids with the concentration of the particles increasing from right to left, illustrating crystallisation at moderate concentrations. Reproduced from Pusey and van Megen [13].

figure 1.2.

Hard spheres with purely excluded volume interactions form face-centred cubic (FCC) and hexagonal close-packed (HCP) crystals, both having 12 nearest neighbours but differing in the stacking of close-packed planes. The calculations of the free-energy difference between the two crystal phases proved challenging. It is now well-established that the the FCC crystal of hard spheres is only marginally more stable relative to the corresponding HCP crystal [22]. As a result of this marginal free-energy difference, random stacking faults are observed in hard-sphere crystals in simulations and experiments, even for crystals grown slowly [23].

In a computational study, Auer and Frenkel investigated the nucleation of hard-sphere colloids, predicting absolute crystal nucleation rates and characterising the structure of the critical nucleus [24]. They observed large discrepancies between the

calculated nucleation rates and those measured experimentally. Moreover, they noted that in contrast to the prediction of classical nucleation theory, the critical nucleus was found to have a random hexagonal close-packed (rHCP) structure, which transformed into the stable FCC structure at a later stage [24]. They suggested that this was a manifestation of Ostwald's step rule, which relaxes the requirement of the nucleation of the thermodynamically stable phase directly [25].

The size of the colloidal particles lends themselves to facile direct observation, providing a gateway to understanding crystallisation processes in great detail [26, 27, 15, 28]. Gasser *et al.* studied the nucleation and growth of nearly hard-sphere colloidal crystals in real space using confocal microscopy and were able to identify the critical nuclei and follow their evolution [15]. They found the critical nuclei to have non-spherical shape and rHCP structure. In a more recent study, Tan *et al.* experimentally investigated the crystallisation pathways in systems of hard-sphere as well as soft-sphere colloids, involving homogeneous nucleation [28]. The kinetic pathways they observed with single-particle resolution revealed the emergence of relatively ordered precursor structures with different symmetries, which subsequently transformed into metastable solids [28].

As alluded to earlier, while sterically stabilised PMMA spheres remain the closest realisation hard-sphere interactions the experimental these particles 'hard spheres', an element of softness in the interparticle interactions is invariably present, requiring the use of an effective hard-sphere diameter [29]. A feature of all sterically stabilised systems is that the compressibility of the stabilisation material can impact the range of the repulsion. In a recent review, Royall *et al.* noted that the compressibility of polymer chains could extend the effective hard-sphere radius by as much as 10% [29]. As such, these particles are frequently referred to as 'nearly hard spheres' in literature [13, 15].

It is also of interest to note here that while studies of nearly hard-sphere colloidal systems in the spirit of colloids as big atoms have played a crucial role to develop of our fundamental understanding of various phenomena occurring in atomic systems, observations, which present contrasts to atomic systems, have also been made even with isotropic interactions. For example, Leunissen *et al.* found that the stoichiometry of colloidal crystals formed by oppositely charged particles was not governed by charge neutrality [30].

1.2 Colloidal Molecules

Since the term "colloidal molecules" was coined by van Blaaderen [31] in the context of pioneering work by Manoharan *et al.* [32], considerable efforts have been undertaken to investigate finite systems of spherical colloidal particles [33, 34, 35, 36]. Manoharan *et al.* followed an emulsion route to study the packing of small numbers of polystyrene microspheres driven by capillary forces [32]. They observed a variety of polyhedra for finite numbers of microspheres, a selection of which is shown in figure 1.3. In this case, the packing was observed to minimise the second moment of mass distributions [32]. As the concept has matured since its inception, the particles are viewed as atoms, the attractive interactions that bind the particles together as bonds, and the different structures observed at equilibrium as isomers [36].

Meng *et al.* discussed the entropic contributions towards the formation of clusters of spherical colloidal particles with a hard core and a very short-ranged attraction in the context of their experimental observations [34], which also motivated subsequent theoretical work [37]. In this case, the energetic contribution is derived from the nearest-neighbour contacts. Of all the isomers having identical numbers of nearest neighbours, highly symmetric isomers are disfavoured because of rotational entropy

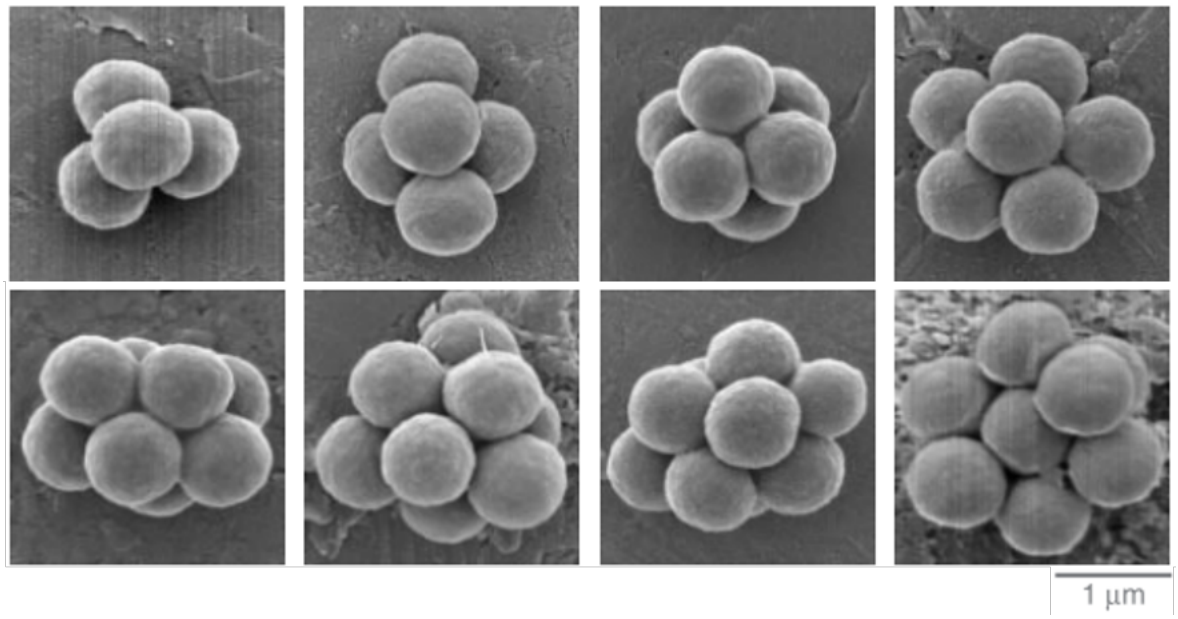

Figure 1.3: Structures of finite numbers of microspheres, as determined experimentally. Adapted from Manoharan *et al.* [32].

[34]; vibrational entropy also makes a contribution to the free energy, which governs the overall stability.

Malins *et al.* found that geometric frustration inhibited the access to the ground state structures with the maximum number of nearest-neighbour contacts for small colloidal clusters, which they investigated in a Brownian dynamics study with competing interactions, including a short-ranged attraction and a long-range repulsion [33]. The authors found that for high attractive interaction strengths the average bond lifetime approached the simulation run time, and these finite systems became non-ergodic. For those with 7 or more colloidal particles the yields of the structures were influenced by geometric frustration in this non-ergodic regime: geometric frustration led to kinetic trapping.

Kraft *et al.* developed a synthetic route to colloidal molecules, where cross-linked polystyrene spheres with liquid protrusion undergoes coalescence of the protrusions

[38]. By controlling the size of the liquid protrusions on the polymer spheres, they achieved control over the geometry of the colloidal molecules formed.

Named after the two-faced Roman god, Janus particles are typically spherical in shape and have two different hemispheres that are different in terms of the surface chemistry [39]. Hong *et al.* developed a route to synthesise Janus particles, which were hydrophobic on one half and charged on the other half, and demonstrated clustering of these colloidal Janus particles [40]. Chen *et al.* investigated the clustering behaviour of Janus colloidal spheres experimentally [41]. In this study, the Janus particles were comprised of a charged hemisphere on one face and a hydrophobic hemisphere on the other. The salt concentration of the medium was increased to reduce the range of the screened electrostatic repulsion, and hence trigger clustering. Notably, these authors observed the growth of triple helices, also called Bernal spirals, by face-sharing tetrahedra [41].

Colloidal clusters, where colloidal particles are chemically fused to form simple polyhedra, have been designed to mimic not only the geometry of small molecules (e.g. tetrahedral geometry of CH_4 and octahedral geometry of SF_6) but also a crude approximation of their valence [42, 43]. Wang *et al.* described the colloidal clusters formed as sp^2 and sp^3 hybridised, driving home the similarities between the colloidal clusters and their molecular counterparts. By incorporating 1-7 bonding sites around a spherical centre, DNA patches were formed at target locations, where the core particle remained non-bonding. The size of the bonding sites was controlled by the protrusion of the DNA coated components, offering a handle to govern the bonding properties of the colloidal cluster. By mixing clusters with different valencies, they were able to replicate bonding geometries prevalent in organic chemistry, such as the colloidal analogues of 'Cis' and 'Trans' bonds. The authors noted that large-scale synthesis of

colloidal particles with more than one binding site by this method suffered from the issue of polydispersity.

1.3 Colloidal Open Crystals

Colloidal open crystals are periodic ordered structures composed of low-coordinated colloidal particles, thus having a maximum density less than what is achieved at close packing [44]. There has been much interest in recent years on the study of colloidal open crystals because they have a range of photonic, phononic and mechanical properties [45, 46, 47], giving rise to a variety of potential applications [48]. In particular, the cubic diamond and cubic tetrastack lattices on the colloidal scale have served as target structures for colloidal self-assembly over the years as they support complete 3D photonic bandgaps, preventing photons of certain frequencies from propagating through the crystals irrespective of their polarisations [49, 50]. Such a bottom-up approach offers a low-cost route to photonic crystals compared to top-down fabrication methods [51]. However, rather low-coordination numbers of the particles in these open crystals, which make them mechanically unstable or leave them on the verge of mechanical instability as per the Maxwell counting rule [52], pose a challenge.

1.3.1 Self-Assembly of Colloidal Open Crystals

Over the last two decades, synthetic advances have made available a rich variety of colloidal building blocks, capable of offering highly directional interactions suitable for low-coordinated structures. In their 2007 Nature Materials paper, Glotzer and Solomon discuss the wide array of anisotropic building blocks synthetically available then [8], a representative collection of which is shown in figure 1.4. Branched particles, with

the example shown in the top row of figure 1.4 from Chen *et al.* [53] grown from gold nanocrystals, allow the formation of a variety of different particle geometries. Chen *et al.* report the formation of a variety of different particle shapes, including tadpole-like or teardrop-like monopods, 90^o L-shaped, 180^o I-shaped, and 120^o V-shaped multipods. In the third row, faceted polyhedra are displayed. These particles also deviate from the spherical colloidal particles discussed before. Gold cubes have been fabricated [54], and the dynamics of cubic colloids has been studied and phase diagrams investigated [55, 56] with respect to crystallisation. Glotzer *et al.* discuss the possibility of combining these various threads of anisotropy, permitting a wide range of potential exotic colloidal interactions to occur.

In one of the early studies of the so-called "patchy particles" [57], Zhang *et al.* demonstrated the self-assembly of a diamond crystal from a disordered phase in computer simulations that dealt with model particles, involving a hard spherical core with the surface of the spheres decorated with circular patches arranged tetrahedrally [58]. These particles are shown schematically in figure 1.5, where the size of the patches is defined by the angle δ. Although computational studies of the self-assembly of diamond crystals from patchy particles have received much attention [59, 60], the experimental realisation of diamond crystals has proved elusive, presumably due to the level of precision required for the particle synthesis.

In a seminal work, Granick and co-workers demonstrated that a colloidal kagome lattice, a 2D open lattice where each particle is bonded to 4 neighbours, can be self-assembled from spherical triblock Janus particles, as shown in figure 1.6 [61]. The triblock Janus spheres these authors considered had two attractive hydrophobic patches on the opposite poles across a charged middle band. The patches, fabricated using glancing angle deposition method [62], have tunable patch sizes, through which the

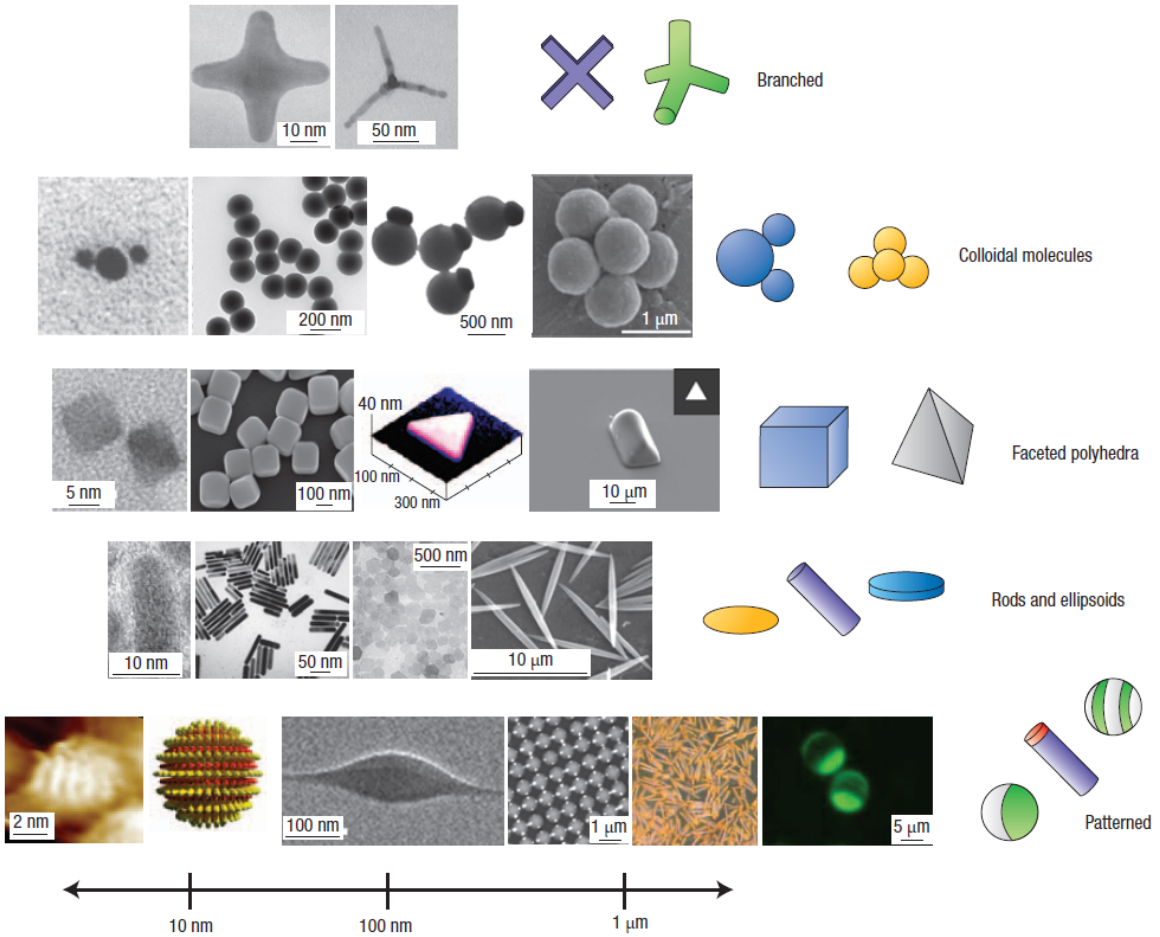

Figure 1.4: Figure from Glotzer *et al.* [8] showing representative experimental developments in anisotropic colloidal particles. Across the rows, the colloidal building blocks are shown schematically to highlight their different anisotropy attributes. Combining these various threads of anisotropy allows a wide range of exotic colloidal interactions.

'valency' of each patch could be controlled. By controlling the salt concentration in the medium and hence the range of screening electrostatic repulsion between the middle bands, self-assembly pathways were induced.

The authors noted that it was crucial to optimise the strength of the patch-patch interactions to allow for corrections of wrong contacts formed along the self-assembly pathways [61]. These pathways typically involved initial formation of web-like structures, including triangular bonding and strings with dangling bonds, and subsequent

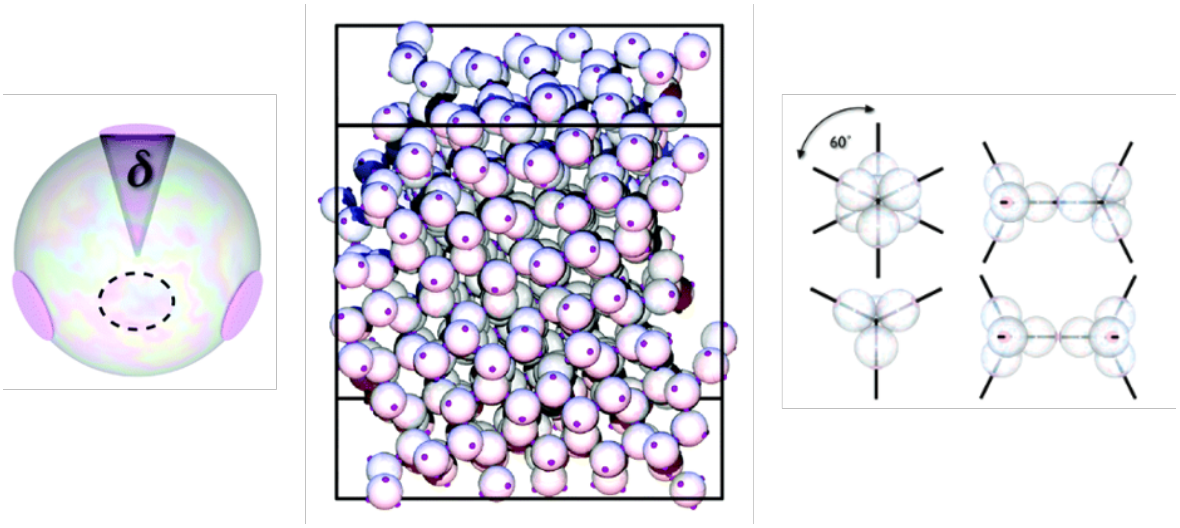

Figure 1.5: Patchy hard spheres with spherical patches arranged tetrahedrally. Left shows the elementary particle and the geometry of the patches. The centre shows the assembly of these particles into a diamond-like structure following the slow annealing protocol, with no seeding Right shows the rotation states present for tetrahedral colloidal molecules. Reproduced with permission from Zhang *et al.* [9]

maximisation of contacts, leading to a network structure of irregular voids. It was observed that the growth of the crystal structure proceeded via metastable intermediates, in contrast to the prediction of the classical nucleation theory [61], and more in keeping with Ostwald Step rule. Subsequent computational study, motivated by this work, observed the self-assembly of a kagome lattice at low temperatures and pressures [63].

In a notable contribution, Mao *et al.* rationalised the mechanical stability of the kagome lattice supported by the triblock Janus spheres in terms of entropic contributions [64]. Using an analytical theory founded on lattice dynamics, it was shown that a contribution from the rotation entropy stabilised the open lattice and another contribution from the vibrational entropy led to the selection of the open lattice over its closed-packed counterpart [64].

Sciortino and co-workers performed crystal structure prediction for Janus colloids

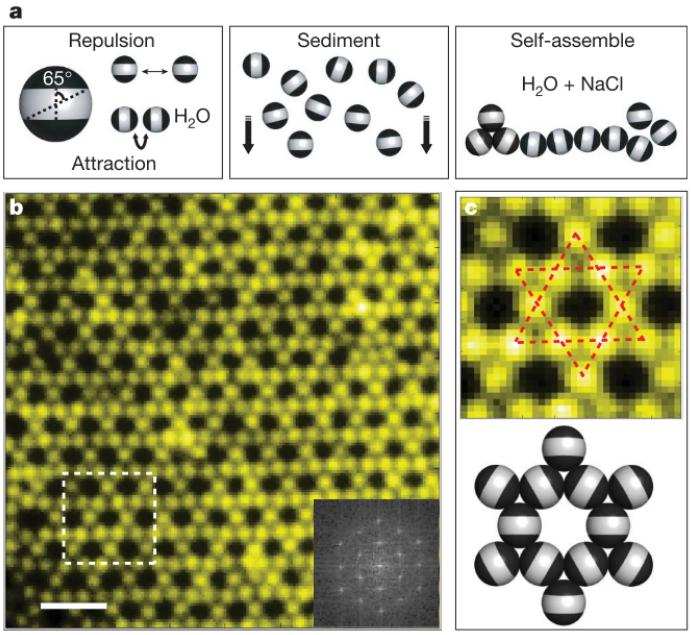

Figure 1.6: Experimental route to growth of Kagome lattice from triblock Janus colloids. a) Triblock Janus spheres hydrophobic on the poles (black, with an opening angle of 65°) and charged in the equator section (white), are allowed to sediment in deionized water. Then NaCl is added to screen electrostatic repulsion, allowing self-assembly by short-range hydrophobic attraction. b) Fluorescence image of a colloidal kagome lattice (main image) and its fast Fourier transform image (bottom right). Scale bar is 4 mm. The top panel in c shows an enlarged view of the dashed white rectangle in b. Dotted red lines in c highlight two staggered triangles. The bottom panel in c shows a schematic illustration of particle orientations. Reproduced with permission from Springer Nature [61].

[65]. Vissers *et al.* modelled these Janus particles through the Kern-Frenkel potential, discussed in greater detail in chapter 2, which describes the repulsive face as a hard-core interaction and the attractive face via square-well attraction. They used an attractive range of 20% of the particle diameter, suggesting an experimental analogue would be closer to the nanoscale range than the microscale, but still firmly within the colloidal regime. They justified this range as it restricted the coordination shell of the colloidal particles to their nearest neighbours only. They mapped a phase diagram to describe the stability of the Janus crystals. This phase diagram is shown in figure 1.7, where

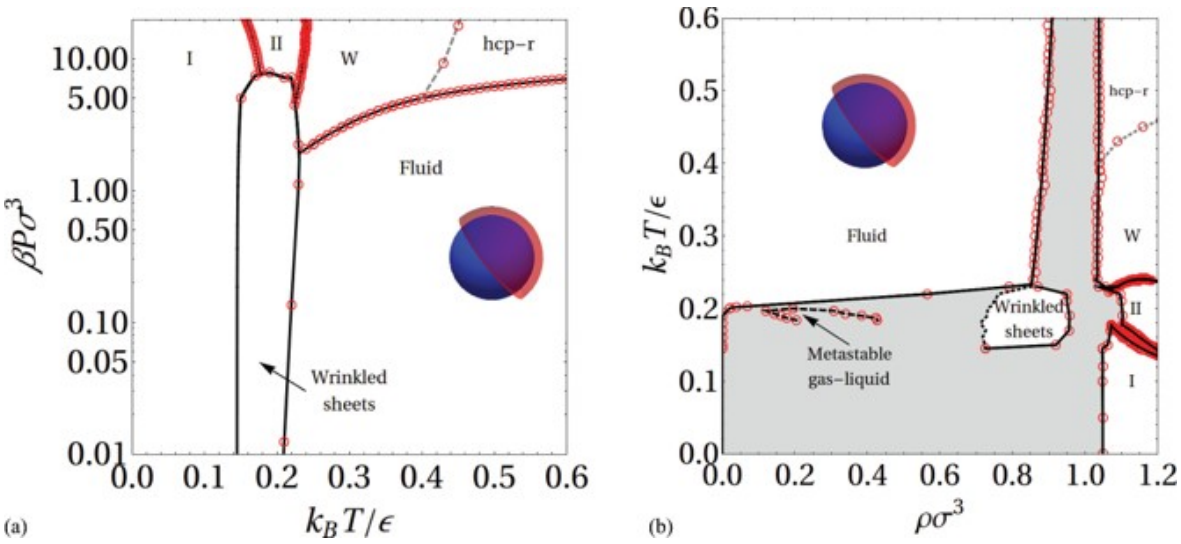

Figure 1.7: Phase diagram for Janus particles with interaction range 0.2σ. (a) The temperature-pressure representation. Units are in k_BT/ϵ and $\beta P\sigma^3$ for temperature and pressure, respectively, where $\beta = \frac{1}{k_BT}$ and σ is the diameter of the colloidal particle. The pressure is plotted on a logarithmic scale. The labels denote crystal I (FCC), II (HCP), W (HCP with 'wrinkles', a stacking defect), and the hexagonal-close-packed crystal with random orientations (rHCP). (b) The representation in the density-temperature plane. Units are in $\rho\sigma^3$ and k_BT/ϵ for density and temperature, respectively. The dotted line on the left boundary of the wrinkled bilayer sheet phase denotes an upper bound for the fluid-sheet coexistence region. Reprinted from Vissers *et al.*, with the permission of AIP Publishing [65].

all dense stable crystals are based on an underlying FCC or HCP structure except the wrinkled sheets phase, which has roughly 25% less density than the FCC and HCP crystals. The authors suggested the use of multiple patches in order to generate stable crystal structures with still lower densities.

In a computer simulation study, Reinhart and Panagiotopoulos investigated the phase space of triblock patchy particles in 3D [66]. They used a modified Kern-Frenkel potential, where each patch is an attractive square well potential with a repulsive hard core. Figure 1.8 shows a wide variety of crystal structures predicted for these triblock patchy particles, with equal-size patches on the poles. While close-packed crystal structures were reported, the authors identified an area of phase space, supporting

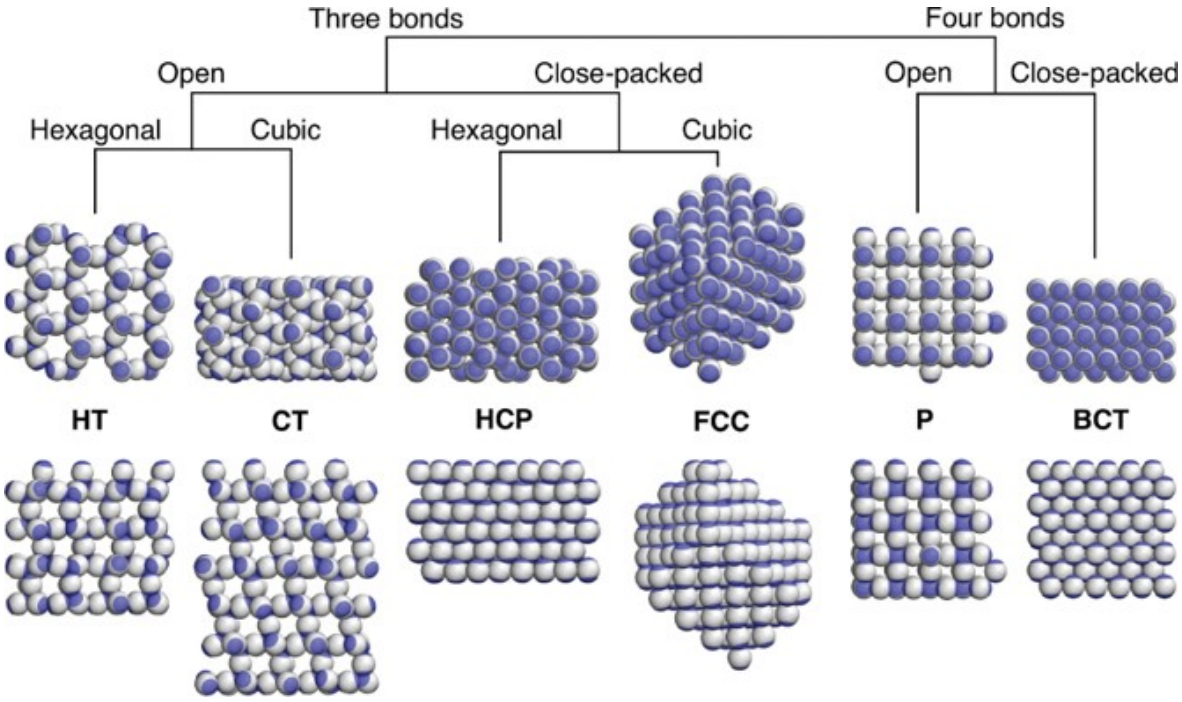

Figure 1.8: Snapshots of each of the stable solid structures for the two-patch Kern-Frenkel model. Top and bottom rows are different views of the same structures, rotated by 90° to show the three-dimensional arrangement of the particles. From left to right, the crystals are hexagonal and cubic tetrastack, hexagonal close packed, face centered cubic, perovskite, and body centred tetragonal. Each snapshot has N = 192 particles. Reprinted from Reinhart and Panagiotopoulos [66], with the permission of AIP Publishing.

stable open crystals of various kinds, including tetrastack and perovskite. The authors predicted competing polymorphs especially for the tetrastack lattice, with a marginal preference for the cubic tetrastack in terms of the free energy [66].

In an earlier work, Romano and Sciortino [67] used spherical triblock patchy particle with triangular patches on the opposite poles. They considered the triangular patches in the staggered arrangement to selectively stabilise cubic tetrastack structure and carried out Monte Carlo simulations to demonstrate the success of their "patterning symmetry" concept. While conceptually appealing, it has proven elusive so far from the perspective of experimental realisations, presumably due to the challenge of fabricating

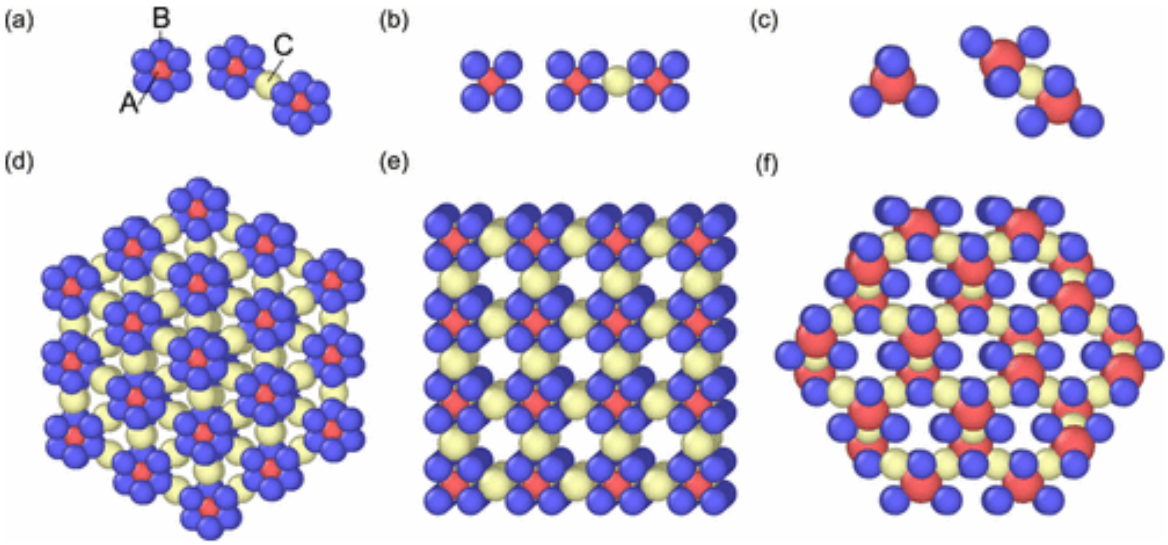

Figure 1.9: Colloidal Cluster Assembly: Colloidal clusters formed from central (Red, A), interacting shell (blue, B) and glue (yellow, C) particles. By tuning the particle sizes and interaction strengths, along with the shapes of the colloidal molecules (a-c), a variety of crystal structures can be targeted. Shown are BCC, SC and cubic diamond (d-f) [68]. Copyright (2016) American Chemical Society.

patch geometry to such a level of sophistication [67].

The use of DNA-mediated interactions allows the chemist significant control over colloidal interactions. Zanjani *et al.* [68] described a route to a simple cubic crystal using cubic colloidal clusters with the introduction of a third 'glue' colloidal particle. Their system is therefore described by the following: 'A' particles at the core; 'B' particles at the patch sites forming an octahedra around the central A particle; 'C' glue particles. This is shown in figure 1.9. In this computational study, by manipulating the interparticle interaction matrix and relative sizes of the three particles, the authors were able to demonstrate the self-assembly FCC, HCP, body-centred cubic (BCC) and simple cubic crystals when grown around appropriate seeds. In order to dissuade the formation of BCC crystal while targeting simple cubic crystal, they proposed two strategies, both focused on removing the energetic degeneracy of the central and corner lattice sites in BCC. The first involved shrinking the B particles and enabling A-C

interactions, thus favouring linear chains where the C particle was able to get closer to the central A particle. The strength of A-C interactions could be manipulated by controlling the density of DNA strands on the particles. The second approach used a lock-and-key approach, where half of the A-B cubes were prepassivated: C particles were already bound to the 6 faces of the cube. The remaining half of the A-B cubes had unbound faces and were therefore able to form a NaCl structure, where the A particles sit on simple cubic lattice points.

1.4 Hierarchical Self-Assembly of Colloids

In 2011 Miszta *et al.* [69] reported on multi-stage hierarchical self-assembly in a colloidal system. The group previously published a "one-pot" approach to the formation of monodisperse branched colloidal nanocrystals with the geometry of an octapod [70]. In their 2011 work, they discussed how these octapods, coated with hydrophobic surfactant molecules, interacted predimantly *via* van der Waals interactions and when dissolved in an appropriate solvent, formed linear chains. These chains are the first level of assembly, where each octapod in the chain is 'interlocked' with its two neighbouring octapods. The chains were observed to reach lengths of over 25 octapods, or 35 nm in length. The authors reported that no other superstructures beyond the interlocked chains were present in toluene, suggesting that the geometry of the octapods, or alternatively the interactions caused by this shape, lead to a good level of selectivity.

The second level of assembly was observed when acetonitrile was added to a system of octapod chains. The addition of this solvent precipitated out a 3D superstructure, where the chains of octapods came together to form a small crystals with octapods sitting on a tetragonal unit cell. The internal structure of the ordered 3D assemblies suggested that these were formed by aggregation of linear chains, rather than clustering

of individual octapods, while the acetonitrile increased the effecive van der Waals attraction that the octapods experience to one-another, essentially locking in the chains and reducing the frequency of octapod dissociation. These crystals, whilst an excellent example of multistage asembly, were prone to defects due to the non-uniform chain length in the first stage of assembly. The authors noted that in the 3D crystals observed, multiple vacant sites in the 3D structure were visible *via* SEM imaging.

Examples of multistage hierarchical self-assembly are shown on the nanoscale by Groschel *et al.*[71] , who showcased recent advances in the design of multicompartment micelles, MCMs. The surfaces of the different compartments can be functionalised with different 'nanoenvironments' and are typically spherical or capsular in shape. The formation of *targeted* MCMs from block copolymers is hindered by the many possible MCMs that are kinetically accessible. Successful higher-order assembly relies upon the monodispersity of the first stage of assembly. Through careful control of polymer solvation, Groschel *et al.* promote the formation of targetted MCMs which then assemble in later stages into 2D lattices and linear chains.

The design of appropriate building blocks for multistaged assembly of pyrochlore and cubic diamond was approached using landscape engineering by Ma and Ferguson [72]. In this approach, a large number of design parameters for spherical colloidal particles decorated with nanodots are investigated via Langevin dynamics, followed by the generation of free-energy surfaces. Each 'candiate' or combination of nanodot binding strengths and locations is rated by a fitness metric, which is based on the relative stability between the target structure and its nearest competitor. Using an evolutionary algorithm the strongest candiates influenced the next generation of candiates, with multiple generations run to find optimal system parameters. Ma and Ferguson identified parameters for nanodot location and binding strengths that avoid kinetic traps and

favoured targeted crystal formation, but fabrication challenges have so far prevented experimental validation of these results.

While triblock patchy particles with equal-size patches on the poles have received considerable attention in recent years, control over patch sizes in experimental fabrication has opened up the prospects of realising different bonding topology [73]. In a recent experimental study, Chen *et al.* synthesised triblock patchy particles with asymmetrical patch sizes and triggered their staged self-assembly pathways by varying the ionic strength of the medium in a stepwise manner [74]. Such pathways provided a route to higher-order structures, where small clusters formed in the first stage acted as the secondary building blocks for the second stage. While their experimental protocol was selective for the wider patches to interact before the narrower patches came into play, the first stage of assembly led to a distribution cluster sizes, as shown in figure 1.10. The second stage of assembly driven by the interaction between narrower patches then produced a porous network rather than an open lattice.

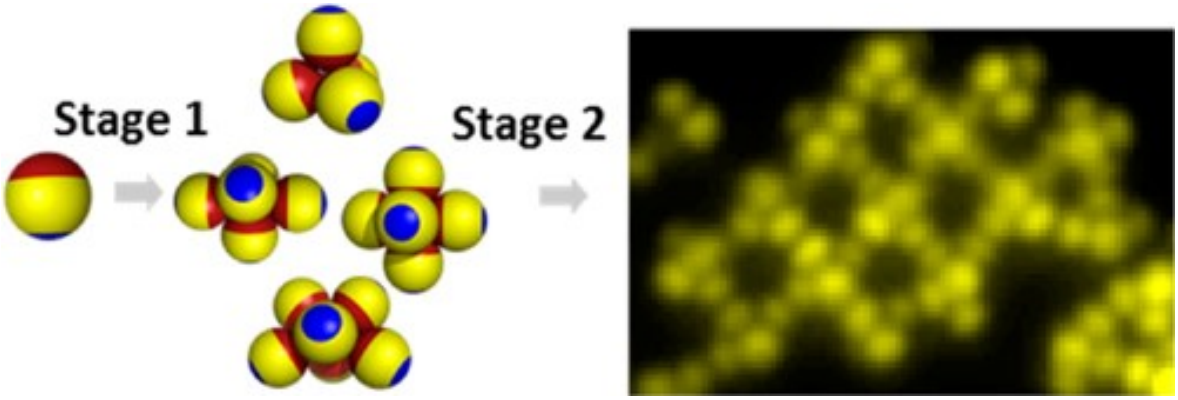

Figure 1.10: Schematics of a two-stage self-assembly route for triblock patchy particles with asymmetrical patch sizes, producing a higher-order network structure via a distribution clusters. Reproduced from Chen *et al.* [74].

An alternative approach to hierarchical self assembly is presented in a computational study by Grunwald *et al.*, who used isotropic colloidal spheres and tuned their

sizes and binding affinities to initially form small clusters of well-defined size and composition with the aid of glue particles [75]. The authors referred to these clusters with an effective patchy interactions as "metaparticles", which then engage in a second stage of assembly, thus yielding a variety of superstructures, including porous crystals. The authors envisaged colloidal nanoparticles coated with DNA to be an experimental realisation of the building blocks they considered with control over binding affinities. It is of interest to note that this computational study treated the metaparticles to be rigid bodies while simulating the second stage of assembly, thus simplifying a multi-scale design problem [75].

In a series of computational studies of finite systems of colloidal magnetic particles with off-centred dipoles, Morphew and Chakrabarti established a set of design rules for encoding hierarchical self-assembly, while addressing the challenges that arise from both thermodynamic and kinetic considerations in the context of such multi-scale design problem [76, 77, 78]. In this series of studies, they demonstrated that colloidal particles with embedded magnetic dipole first self-assembled into trimers, which then went on to form hollow spherical structures. They also demonstrated two-stage self-assembly of tubular structures via square planar subunits [77]. In the context of two-stage self-assembly into thermodynamically favoured hollow spherical structures, they remarkably observed that the structure, which derived the most energetic stability from the first stage of assembly and the least from the second stage of assembly, was most kinetically accessible. The rationale they offered to explain this observation provided the foundation for the hypothesis that a hierarchy of interaction strengths realised with triblock patchy particles could be used to programme hierarchical self-assembly [79]. This hypothesis was validated in a computational study by Chakrabarti and co-workers, demonstrating the hierarchical self-assembly of a colloidal open crys-

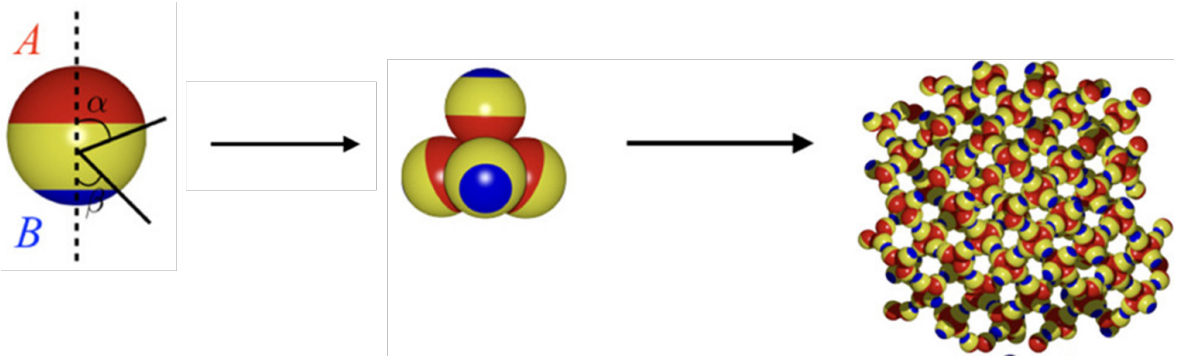

Figure 1.11: Schematic illustration of a hierarchical self-assembly scheme encoded in triblock patchy particles to yield a colloidal open crystal of cubic diamond symmetry via tetrahedral colloidal molecules. Reproduced from Morphew *et al.* [79].

tal with the cubic diamond symmetry from triblock patchy particles via tetrahedral clusters, as shown schematically in figure 1.11. The formation of tetrahedral clusters exclusively during the first stage of assembly was crucial for the success of realising a crystal upon the completion of the second stage.

1.5 Colloidal Self-Assembly: Thermodynamics and Kinetics

Self-assembly of an ordered structure from colloidal particles typically occurs through an interplay between attractive and repulsive interactions. A detailed understanding of colloidal interactions is thus crucial for programming colloidal self-assembly to yield a desired ordered structure. The target structure is required to be both thermodynamically most favoured and kinetically accessible for designer colloidal particles for the success of programmed self-assembly [80]. The free-energy landscape provides a theoretical framework to describe the thermodynamics and kinetics of self-assembly. The potential energy landscape, which is easier to explore, also provides useful information,

especially at low temperatures.

1.5.1 Brownian Dynamics and Colloidal Interactions

If the difference in mass between the solvent and the colloidal particle is small enough that the change of momentum after a collision is non-negligible, 'random' Brownian motion can be observed. Such 'solvent-particle' interactions were first recorded by the botanist Brown in 1828 whilst studying pollen, whose observations were used by Einstein to help develop molecular theory [81, 10]. The equations used to model the movement of Brownian particles are described in the Langevin equation, which extends Newton's equation of motion with contributions from Stokes' law to model friction, along with additional fluctuating forces to model the collisions between the mass and solvent particles. Further discussion around the Langevin equation can be found in chapter 2.

A variety of potentials have been used to describe the large numbers of possible colloidal interactions. These are discussed in detail in chapter 2 but a brief overview is provided here. Charge-stabilised colloidal particles are described by the **DLVO theory** [82, 83]. Here, particles are attracted to one-another by relatively longer-ranged van der Waals interactions, while like-like surface charges provide a relatively shorter-ranged repulsion. The depletion interaction, describing the apparent attraction between uncharged colloidal particles caused by the addition of small depletant particles, is described with the **Asakura–Oosawa** model [84]. Here the available volume accessible to the added depletants is greater when the larger colloidal particles are closer together, as the exclusion zones around the colloids overlap. When discussing interactions between patchy particles, discussed in detail below, a square well potential is often used. The **Kern-Frenkel** potential [85] describes how the relative orienta-

tions of the patches govern the potential energy contributions. Plots of these three potentials, which are discussed in further detail in chapter 2 are shown in figure 1.12.

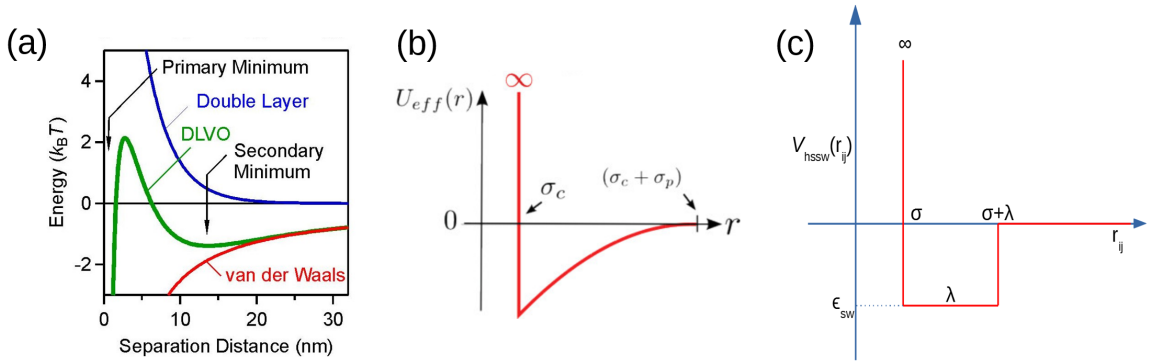

Figure 1.12: Plots showing interaction potentials. (a) the DLVO potential, reproduced from Trefalt and Borkovec [86] CC BY 4.0. (b) The depletion interaction, providing an effective entropic attraction term. Reproduced from Binder *et al* [87]. (c) The Kern-Frenkel [85] potential, providing square-well attraction corresponding to the patches making a 'contact'.

1.5.2 Self-Assembly and the Kinetic Crossover

As discussed by Jack, Hagan and Chandler [88] amongst others [89, 3, 90, 91], successful self-assembly requires cooperative thermodynamics and kinetics. The themodynamic requirement for a system to self-assemble into the ordered structure is that it exists as the lowest free-energy minimum, , while the kinetic requirement highlights the need for the system to reach this minimum in a timescale suitable for the application. As the temperature of the system is lowered, the thermodynamic term drives the system towards adopting the ordered state, but the exploration of different metastable minima will be reduced. Jack *et al.* referred to a "kinetic crossover", taking place across a temperature window beyond which lowering the temperature decreases the successful formation of the target structure. Identifying this region highlights the phase space around which the self-assembly will be most successful.

In order to identify this region, Jack, Hagan and Chandler employed the fluctuation-dissipation theorem, which describes the response to perturbations away from but close to equilibrium in terms of the relaxation of spontaneous fluctuations at equilibrium [92]. How the system responds to these perturbations differs depending on the location of the current state point relative to the kinetic crossover. By calculating the fluctuation-dissipation ratio, Jack *et al.* were able to distinguish between systems above and below the kinetic crossover region in the context of assembly of viral capsids and of crystallisation of sticky disks. Crucially, this analysis in terms of the fluctuation-dissipation theorem can be applied from observations made early in the simulation lifetime, able to provide insight to the chemist as to what area of the phase space will lead to successful self-assembly without running longer simulations. As such, may short simulations can be run to identify effective assembly conditions.

This idea is represented in figure 1.13, reproduced from a later paper Klotsa and Jack [89]. In this paper the group investigated the self-assembly of hard-sphere square-well particles using Monte Carlo, using the fluctuation-dissipation theorem to identify likely candidates of parameter space that would lead to successful crystallisation. This new utilisation provided generality to the application of fluctuation-dissipation theorem to investigating crystallisation phase-space. In a later paper Klotsa and Jack [93] proposed a method to automatically adapt the manipulation of system changes using fluctuation-dissipation theorem as the simulations were run, enabling a feedback loop to identify the most optimal protocol. They found that this approach quickly locates interaction parameters for which assembly is effective.

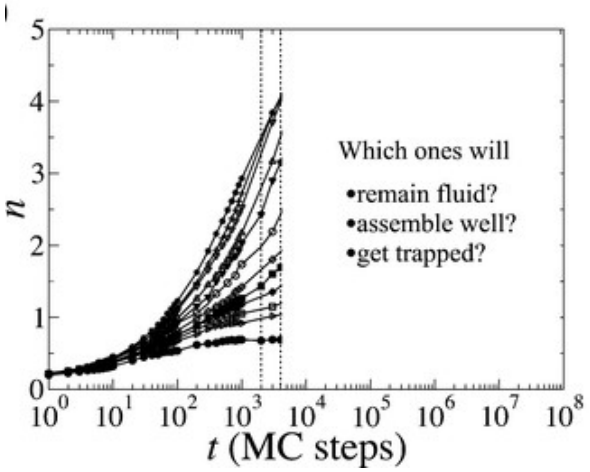

Figure 1.13: A Fluctuation-Dissipation theorem, Klotsa *et al* [89]. Here n is the average number of bonds per particle for simulations of various bond strengths. From information obtained between the vertical dashed lines, the group can identify which simulation states will lead to a fluid, which will assemble successfully and which will become trapped in a dissordered state. Reproduced with permisison.

1.5.3 Energy Landscapes

As alluded to above, understanding the thermodynamics of the system is crucial to correctly identifying the parameter space most likely to lead to the targeted crystalline structure. The potential energy landscapse of a system is defined by a mathematical function that describes its potential energy as a function of its degrees of freedom. Typical points of interest on these energy landscapes are stationary points, where the gradient in multiple directions is zero, as these describe minima and transition states of the system.

Examples of such surfaces are shown in figure 1.14, where the top image shows a potential energy landscape for a proton exchange interaction. In this system, the potential energy is a function of just the two interparticle distances, R_{AB} and R_{BC}. In the bottom figure,a free energy surface is shown where the free energy G of a protein folding reaction is plotted against parameters Q and P. Three routes navigating the

energy surface are shown in yellow (fast folding), red and green (both slower folding), matching experimental observations of different rates of protein folding [95]. We note that in this case, there are multiple possible pathways towards the same folded free-energy minimum. Understanding of the energy landscape in order to predict and explain the alternate reasonable trajectories a system may take is critical for successful design of targeted self-assembly pathways.

Analysis of potential and free energy landscapes is crucial for crystallisation studies [96, 94, 97], where information about equilibrium thermodynamic properties can be extracted and lowest energy pathways between energy minima can be calculated, often displayed through disconnectivity graphs [98, 99]. Multiple methods exist for calculating the free energy landscape, such as umbrella sampling [100, 101] and metadynamics [102], but these are beyond the scope of this thesis. Interested readers are directed towards reference [94] for in-depth disccussion surrounding energy landscapes. The methods used to navigate the potential energy landscape relevant to this thesis are described in section 2.6.

1.5.4 Thermodynamic Integration

For a system with fixed volume, temperature and number of particles (NVT), the Helmholtz free energy is minimised for a system at equillibrium. If we wish to know what the system would look likle at equilibrium, calculating the free energy at various points in the phase diagram will let us describe the system and identify points of interest.

Calculation of free energy is dependent on both the parameters defining the point in phase space and the accessibility of that point from other state points [103]. There are multiple methods available to calculate free energy, such as the Gibbs ensemble

method [104] and Gibbs-Duhem integration [105], but the approach typically used for calculating free energy differences for the generation of phase diagrams is thermodynamic integration. For this method, a similar system of known free energy is used as a reference. The free energy difference between the known system and the system of interest is then calculated along a pathway between the two. This pathway is usually created following Kirkwood's coupling parameter methods. An overview of this method is provided in reference [103], with illustrative applications for colloidal systems provided by Hynnien and Panagiotopoulos in reference [106], where phase diagrams of charged colloids are calculated through thermodynamic integration methods, and Muller and Daoulas [107] who calculate the free energy difference along a reversible path connecting the disordered and the self-assembled ordered state.

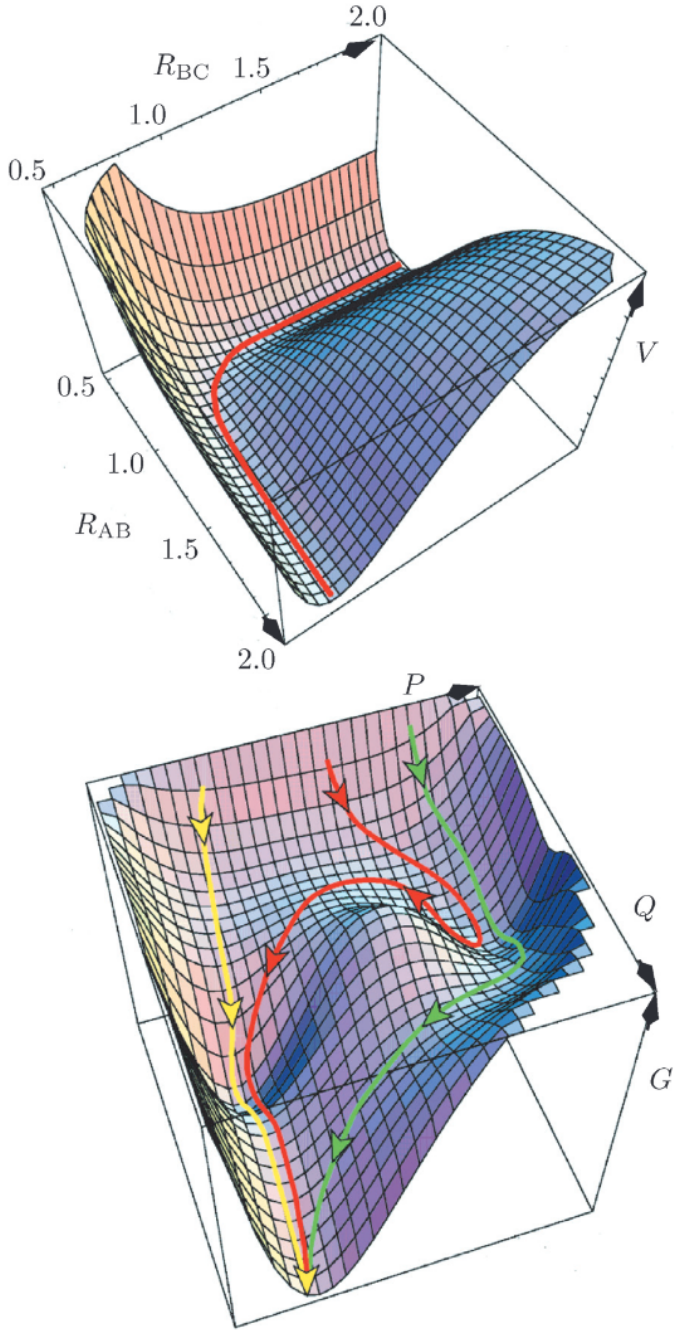

Figure 1.14: Representations of a potential (top) and free energy (bottom) landscape. The top figure shows the potential energy, V, as a function of two order parameters, R_{AB} and R_{BC}. The bottom figure shows multiple possible trajectories for the folding of lysozyme, each exploring different areas of the energy landscape. Reproduced with permisison from Wales [94].

1.5.5 Law of Correspondent States

The law of correspondent states, introduced by van der Waals, is the observation that real gases at corresponding states behave similarly. According to this law, all simple fluids obey the same reduced equation of state if the thermodynamic variables that describe the equation of state is scaled with respect to their values at the critical point.In their 2000 paper, Noro and Frenkel [108] discussed how this law could be adapted to predict the topology of the phase diagram for suspensions of colloidal particles having isotropic interparticle interactions with different ranges of attractions.

Following this work, Foffi and Sciortino generalised the extended law of corresponding states to consider patchy particles interacting via anisotropic potentials close to the liquid-gas critical point.[109]. Whilst the extended law of correspondent states suggested by Noro and Frenkel does not generically hold for non-spherical potentials, Foffi and Sciortino suggested that the application of thermodynamical pertubation theory developed by Wertheim [110] allows for the possible generalisation in the limit of one bond per patch. In this theorem the shape of the patches is not considered and it is assumed that each patch acts as as an independent interacting unit. Foffi and Sciortino considered patchy particles with 3, 4 and 5 patches for a variety of different patch ranges and sizes. Their work showed that the generalised law of corresponding states is obeyed by patchy particles with same number single-bond patches.

1.6 Thesis Outine

In this context, the overall aim of this thesis is to investigate the versatility of the hierarchical self-assembly scheme encoded in triblock patchy particles to realise colloidal open crystals via colloidal molecules. To this end, the objectives are as follows:

1. to explore the formation of distinct colloidal molecules of well-defined size and shape upon the completion of the first stage of self-assembly;

2. to explore routes to a variety of colloidal open crystals, exploiting different valences of the colloidal molecules using the patch width as a control parameter;

3. to investigate whether hierarchical self-assembly pathways can make colloidal open crystals kinetically accessible;

4. to characterise dynamical pathways to colloidal open crystals in detail to glean mechanistic insight especially into polymorph selection.

The thesis is organised as follows: **Chapter 2** provides an overview of the methodology, describing a variety of computational techniques employed to carry out the present body of work. **Chapter 3** explores hierarchical self-assembly of triblock patchy particles via octahedral colloidal molecules and reports the formation of body-centred cubic crystals. **Chapter 4** then explores whether a simple cubic crystal can be self-assembled from these triblock patchy particles via octahedral colloidal molecules. In **Chapter 5**, we devise a bottom-up route to tetrastack crystals via tetrahedral colloidal molecules and rationalise our observation that in this case hierarchical self-assembly pathways promote crystallisation in preference to an amorphous phase. In **Chapter 6**, we present an analysis of the pathways to tetrastack crystals, discussing a competition

between cubic and hexagonal polymorphs. Finally, **Chapter 7** provides a summary of the work presented and a future outlook.

Chapter 2

Methodology

In this chapter we will discuss the underlying models and theory for the simulation of colloidal suspensions. We highlight interaction potentials of interest and discuss the Brownian dynamics, global optimisation and crystal identification techniques used throughout this body of work.

2.1 Particle Stabilisation

In order to form targeted structures such as system-spanning networks and crystals, the colloidal particles must be stabilised against various pathways to phase separation. Processes such as sedimentation and aggregation that drive the system to phase separation are often in direct competition with the pathways to the formation of the targeted network [111] . Irreversible aggregation is typically referred to as coagulation, where the formation of many small aggregates from the dispersed state is permanent. Where the aggregation forces are weaker and can be overcome through mixing or stirring the phase transition is referred to as flocculation [112].

Steric Stabilisation and Gravitational Forces

One technique to stabilise the system is steric stabilisation, involving the chemical bonding of many long-chained groups to the surface of the particle [113]. When the coated particles are far apart, the chains attached have the freedom to rotate into a large number of configurations. If the particles come closer together then the number of accessible states of the chains decreases, lowering the entropy of the system. This provides the system with an entropic driving force to remain apart, without imposing any long-range repulsion. The range of this repulsion is therefore dictated by the lengths of the chains attached to the nanoparticle. An example of the potential energy contributions from steric repulsion of surface polymers is shown in figure 2.1, where the length of the polymer chains, n, can be seen to extend the repulsion, preventing the particles from moving closer together and hence minimising the potential energy gain from the van der Waals attraction present in the system.

As well as attractive and repulsive forces, particles are also subjected to a gravitational force courtesy of Earth's gravitational field. Sedimentation and creaming can occur when the colloidal particles are heavier, or lighter, than the solvent they are suspended in. The sedimentation velocity v_s, the velocity at which a particle will fall or rise if creaming, is given as

$$v_s = \frac{2}{9}\frac{\Delta\rho g a^2}{\eta_0}$$

where $\Delta\rho$ is the difference in density, g is the gravitational constant and η_0 is the solvent viscosity. If $\Delta\rho$ is negative, the particle undergoes creaming, and the magnitude of $\Delta\rho$ dictates the speed of the phase transition. To stabilise the system against sedimentation and creaming, the system must be density matched to the solvent [112, 115].

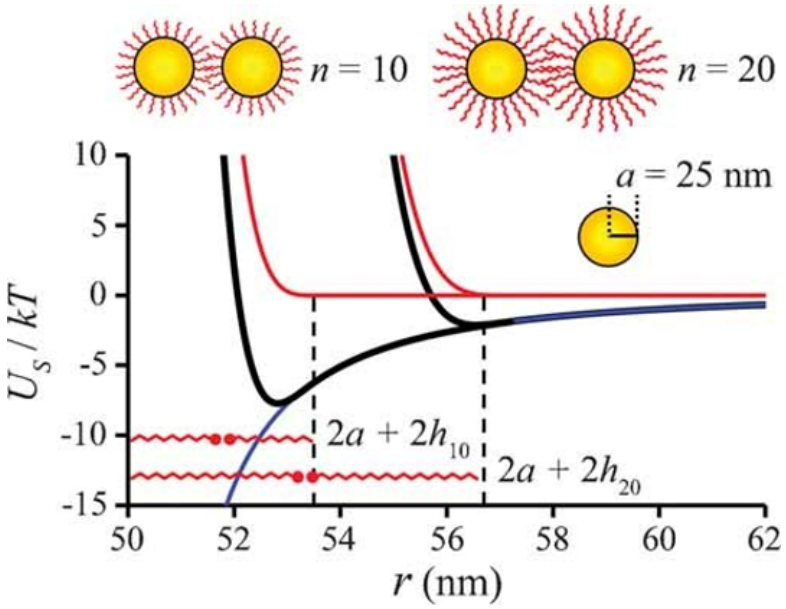

Figure 2.1: Potential energy plot showing steric repulsion (red) and van der Waals attraction (blue), with total interparticle potential in black, for two different monomer lengths (n) in the polymer chains. Reproduced from Bishop [114].

2.2 The DLVO Potential

A complex interplay of attractive and repulsive forces exists for colloidal particles suspended in polar solvents. Colloidal particles exhibit attraction to each other, typically the product of London dispersion forces [116]. As well as this short-range attraction, particles suspended in polar solvents typically acquire a layer of charged ions at their surface. This charge can arise from from dissociation and adsorption of ionisable groups present at the surface-liquid interface [117]. Oppositely charged counterions in the solvent will be attracted to the net charge and form a second layer around the first charged sphere. The formation of this second layer effectively neutralises the long range repulsion, where the range of this repulsion can be influenced by the addition of salt.

The theoretical framework to describe these interactions is known as DLVO the-

ory [82, 83]. This theory presents a description of the interactions between a pair of charged, spherical colloidal particles interacting through the forces described above. The interaction potential is shown below:

$$V(H) = \frac{64\pi a n k_B T \gamma^2}{\kappa^2} \exp\left(-\kappa H\right) - \frac{H_m a}{12H}$$

where H_m is the Hamacker constant, a system dependant constant which scales the interaction strength, a is the radius of the two identical spheres, n is the concentration of electrolyte solution, γ is the particles surface potential, κ is the inverse of the thickness of the double layer and H is the surface-surface distance [118]. The components of this potential are shown in figure 2.2 where the long ranged attraction is shown, along with the shorter ranged repulsion. The height of the maximum and its position can be controlled through manipulating various variables present in the equation, typically by changing n and H_m, and the barrier to coagulation can even be completely removed leading to widescale aggregation of particles [118]. Appropriate care must be taken to choose system parameters to avoid this scenario if control of the aggregation pathways is required.

Whilst the DLVO theory works well for charged particles at long distances, discrepancies were noted at smaller separations [114]. A computationally less expensive alternative to modelling the repulsion in the DLVO potential for colloidal particles which shares the same form is the Yukawa potential:

$$V_{Yukawa}(r_{ij}) = \epsilon_Y \frac{\exp(-\kappa(r_{ij} - a))}{r_{ij}/a}$$

Here, the strength of the repulsion is scaled by ϵ_Y, and the range dictated by κ. The Yukawa potential has been found to show good correlation with experimental colloidal

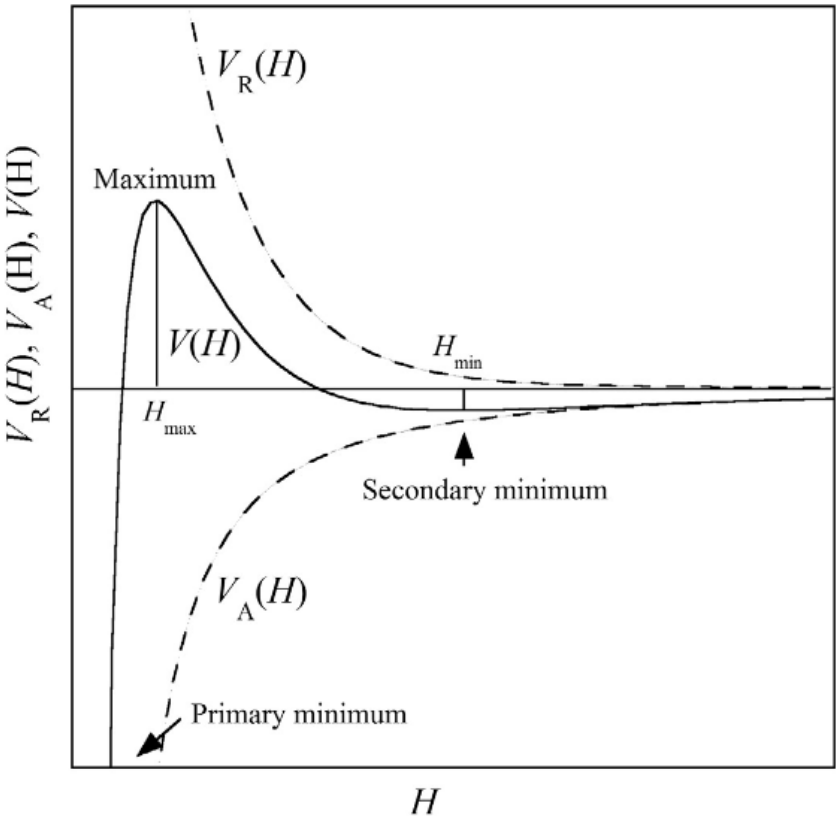

Figure 2.2: Plot of repulsive and attractive components of DLVO potential. Reproduced from Oshima[118].

systems [119].

2.3 Attractive forces

As discussed in the previous chapter, a variety of potentials are frequently used to describe attractions between colloidal particles. In the sections below a mathematical overview is provided of some potential interactions frequently used in this field.

2.3.1 Depletion

An example of such an attractive interaction is the entropically driven depletion interaction. Small, neutral hard-sphered 'depletion agents' with radii R_D are added to the system. The colloidal particles themselves have a radii R_C. $R_D << R_C$. As both the depletion agents and colloidal particles are hard spheres, there will be a volume of space around the larger spheres called an 'exclusion zone' where the depletion agents cannot enter. The volume of such a space is defined by

$$v_{ez} = \frac{4}{3}\pi(R_C + R_D)^3 \tag{2.1}$$

The total volume excluded will be the concentration of colloidal particles multiplied by the equation 2.1, assuming $[D] > [C]$. When two of the larger, colloidal particles come together, their exclusion zones can overlap before the electrostatic or steric repulsion begins to repel the spheres. In such a scenario the total volume excluded to the depletion particles in the system will decrease, increasing the entropy of the system and giving rise to an effective attraction, driving the formation of clustering. This is shown pictorially in figure 2.3. The range of the depletion attraction is the radius of the depletant particles, which are significantly smaller than the colloidal particles.

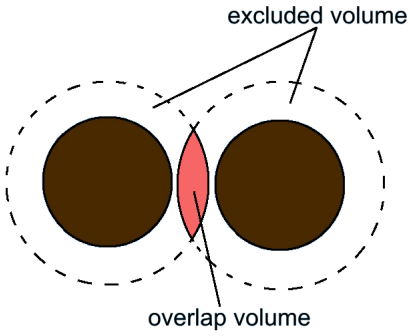

Figure 2.3: Depiction of the excluded volume decreasing when two particles approach one another.

As such, the potential energies of clusters are essentially dictated by the number of contacts each colloidal particle has in the limit of very short range attractions [120].

The combined Asakura-Oosawa potential is as follows:

$$\frac{v(r)}{k_{\mathrm{B}}T} = \begin{cases} -\frac{\pi\sigma_{\mathrm{p}}^3 z_{\mathrm{p}}}{6}\frac{(1+q)^3}{q^3}\left(1 - \frac{3r}{2(1+q)\sigma_{\mathrm{c}}} + \frac{r^3}{2(1+q)^3\sigma_{\mathrm{c}}^3}\right) & \text{for} \quad \sigma < r < \sigma_{\mathrm{c}} + \sigma_{\mathrm{p}} \\ 0 & \text{for} \quad r \geq \sigma_{\mathrm{c}} + \sigma_{\mathrm{p}} \end{cases} \tag{2.2}$$

where $q = \sigma_{\mathrm{p}}/\sigma_{\mathrm{c}}$ is the size ratio and z_{p} is the fugacity of the polymers. The range of the depletion attraction is thus governed by the size of polymers, which is significantly smaller than the colloidal particles. The depletion attraction is therefore relatively short-ranged. The depth of the potential increases linearly with the fugacity, which is related to their chemical potential, and hence depends on the concentration of the polymers.

2.3.2 The Kern-Frenkel Potential

Many of the patchy particle simulation papers discussed in the preceding chapter use the Kern-Frenkel potential to model patch-patch interactions [85]. In this model, at-

tractive patches are present on the surface of spheres interacting via the hard-sphere potential. As such, this potential takes into consideration the particles orientation as well as translation, as only patch-patch interactions are attractive. The potential is shown below:

$$V_{ij}(\boldsymbol{r}_{ij}, \boldsymbol{n}_i, \boldsymbol{n}_j) = V_{hssw}(r_{ij}) \cdot f(\boldsymbol{r}_{ij}, \boldsymbol{n}_i, \boldsymbol{n}_j) \tag{2.3}$$

where V_{hssw} is the square-well potential described by:

$$V_{hssw}(r_{ij}) = \begin{cases} \infty & \text{for} \quad r < \sigma \\ -\epsilon_{sw} & \text{for} \quad \sigma \leq r < \lambda\sigma \\ 0 & \text{for} \quad \lambda\sigma \leq r \end{cases} \tag{2.4}$$

where the range of the attractive well is λ and the depth ϵ_{sw}. The orientational dependence is given by:

$$f(\boldsymbol{r}_{ij}, \boldsymbol{n}_i, \boldsymbol{n}_j) = \begin{cases} 1, \text{ if } \boldsymbol{n}_i \cdot \boldsymbol{r}_{\text{ij}} \geq \cos\theta_0 & \text{and} \quad -\boldsymbol{n}_j \cdot \boldsymbol{r}_{\text{ij}} \geq \cos\theta_0 \\ 0, & \text{otherwise} \end{cases} \tag{2.5}$$

where $\boldsymbol{n}_i$ is defined by the spherical angles $w_i = (\theta_i, \varphi_i)$ in an arbitrarily oriented coordinate frame and describes the orientation of the centre of the patch, $\boldsymbol{r}_{\text{ij}}$ is the interparticle angle under the same coordinate system and θ_0 is the size of the patch. From this potential, we can see that any overlap between hard spheres would cause an infinite repulsion, while only correct patch-patch orientation would allow the attractive aspect of the square-well potential to come into force. A figure showing the Kern-Frenkel potential is shown in the previous chapter, figure 1.12 (c).

2.3.3 Anisotropic Triblock Patchy Particles

The designer triblock patchy colloidal particles we use as our elementary building blocks for hierarchical self-assembly are spherical in shape with two circular patches A and B at opposite poles, modelled as rigid bodies. The patches A and B can differ in terms of their surface coverage, characterised by the angles α and β respectively which define their half-patch widths.

The patches A and B can both interact with themselves and one another. Here, ϵ_{AB} is the depth of the potential due to the patch A - patch B interaction when the two patches face each other. The effective potential for a pair of patchy particles V_{ij} is given by

$$V_{ij}(\boldsymbol{r}_{ij}, \boldsymbol{\Omega}_i, \boldsymbol{\Omega}_j) = V_{\mathrm{Y}}(r_{ij}) + \sum_{p \in i} \sum_{p' \in j} V_{pp'}(\boldsymbol{r}_{ij}, \boldsymbol{\Omega}_i, \boldsymbol{\Omega}_j) w_{pp'}(r_{ij}) \tag{2.6}$$

where $\boldsymbol{r}_{ij} = \boldsymbol{r}_j - \boldsymbol{r}_i$ is the separation vector between triblock patchy particles i and j, $\boldsymbol{r}_i$ is the position vector for the geometric center of the patchy particle i and r_{ij} the magnitude of the vector $\boldsymbol{r}_{ij}$. $\boldsymbol{\Omega}_i$ and $\boldsymbol{\Omega}_j$ describe the orientations of particles i and j, respectively. The isotropic component U_{Y} is the repulsive Yukawa potential

$$V_{\mathrm{Y}}(r_{ij}) = \epsilon_{\mathrm{Y}} \frac{\exp[-\kappa(r_{ij} - \sigma)]}{r_{ij}/\sigma}, \tag{2.7}$$

where κ is the inverse Debye screening length and ϵ_{Y} is the Yukawa contact potential.

The angular dependence of the patch-patch interaction is described by $V_{pp'}$:

$$V_{pp'}\left(\mathbf{r}_{ij}, \mathbf{\Omega}_i, \mathbf{\Omega}_j\right) = \epsilon_{pp'} \frac{1}{4} \left[1 + \Phi\left(\mathbf{r}_{ij}, \mathbf{\Omega}_i, \mathbf{p}_i\right)\right] \left[1 + \Phi\left(\mathbf{r}_{ji}, \mathbf{\Omega}_j, \mathbf{p}_j\right)\right], \tag{2.8}$$

$$\Phi\left(\mathbf{r}_{ij}, \mathbf{\Omega}_i, \mathbf{p}_i\right) = \begin{cases} -1, & \cos\theta_{ijp_i} < \cos\delta, \\ -\cos\left(\dfrac{\pi\left[\cos\theta_{ijp_i} - \cos\delta\right]}{1 - \cos\delta}\right), & \cos\theta_{ijp_i} \geq \cos\delta. \end{cases} \tag{2.9}$$

Here $\mathbf{p}_i$ is a normalised vector from the centre of the spherical particle i in the direction of the centre of patch p on it and thus depends on $\mathbf{\Omega}_i$; $\cos\theta_{ijp_i}$ is the scalar product of the vectors $\hat{\mathbf{r}}_{ij}$ and $\mathbf{p}_i$. Here, $\delta = \alpha, \beta$ and hence the parameter $\cos\delta$ controls the width of a patch.

The distance dependence of the patch-patch interaction is governed by the function $w_{pp'}$:

$$w_{pp'}\left(r_{ij}\right) = \begin{cases} -1, & \text{if } \left(r_{ij} - \lambda\right) < 0, \\ -\frac{1}{2}\left[1 + \cos\left(\pi\left(r_{ij} - \lambda\right)s\right)\right], & \text{if } 0 \leq \left(r_{ij} - \lambda\right) \leq s^{-1}, \\ 0, & \text{if } \left(r_{ij} - \lambda\right) > s^{-1}, \end{cases} \tag{2.10}$$

where λ is the largest separation at which the patch p - patch p' attraction is at its strongest and the parameter s controls the range over which this attraction vanishes. In the present study, λ was set to 1.01σ. We used reduced units: the length in the units of σ, the energy in the units of ϵ_{Y}, the temperature in the units of $\epsilon_{\mathrm{Y}}/k_{\mathrm{B}}$, with the Boltzmann constant k_{B} taken to be equal to one. The parameter σ provides an estimate for the size of the charge-stabilised patchy particles in the absence of a hard core. We show how the potential varies for particles with different range parameters, s, and patch strengths, ϵ, in figure 2.4.

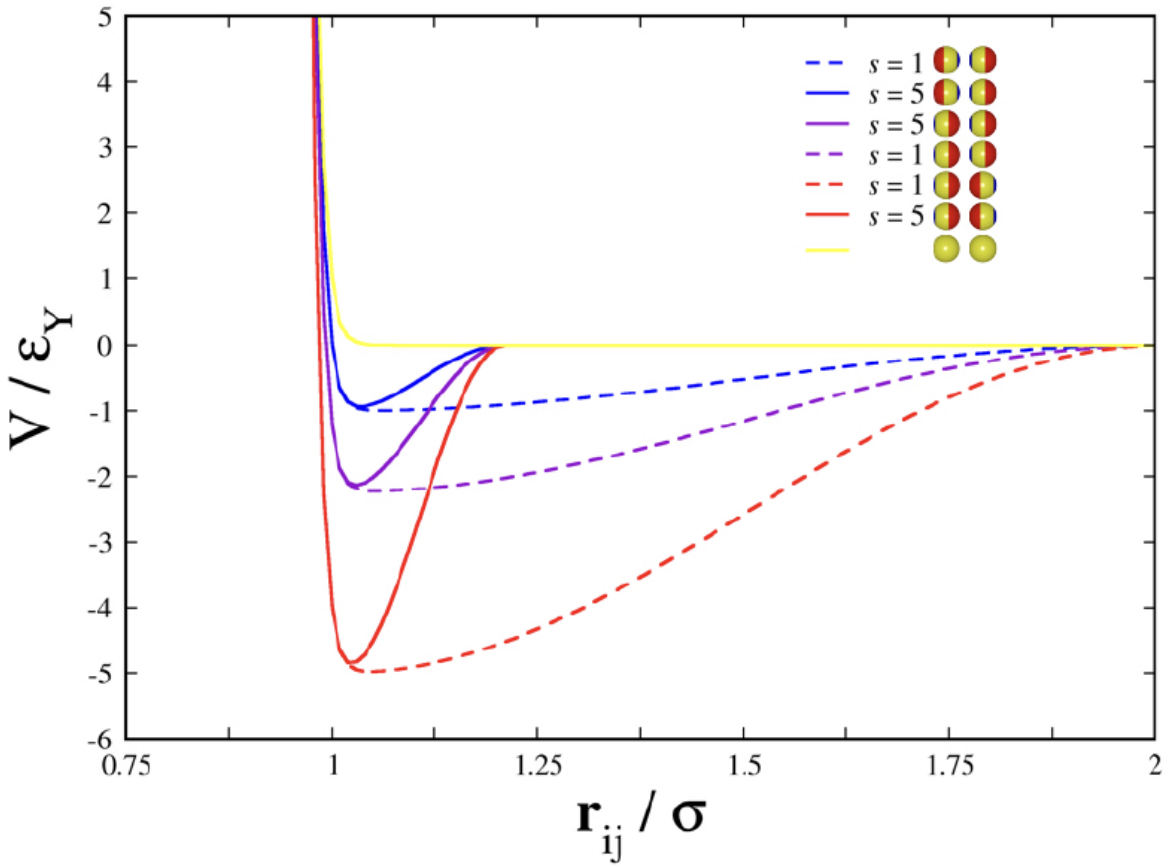

Figure 2.4: The effective pair potential for the patchy particles under consideration as a function of separation for three different orientations - strong-strong, strong-weak and weak-weak. The following parameters are kept constant: $\epsilon_{AA} = 5$, $\epsilon_{BB} = 1$, $\alpha = 80^o$, $\beta = 40^o$, $\kappa = 100$. The isotropic component, given by the Yukawa potential V_Y, is shown separately in yellow.

2.4 Orientation

As we have seen, when handling particles with patches and other forms of anisotropy we must keep track of the particles rotation. We use a rigid-body description for our colloidal particles, where operations on our particles typically include a translational and rotational step. Manipulation of the translational components of a simulated colloidal particle is straightforward by tracking the centres of mass of particles with Cartesian coordinates. Depending on the nature of anisotropy, multiple methods of handling the rotational components present themselves. An in-depth discussion around the correct handling of orientations is discussed by Chakrabarti and Wales, but briefly below we discuss rotation matrices and angle axis [121]. A rotation of a rigid body can be described by a single three dimensional vector, $\boldsymbol{p}$, of which the direction indicates an axis to rotate about, and the magnitude indicates the angle by which to rotate: $\boldsymbol{p} = [p_1, p_2, p_3] = \theta\hat{\boldsymbol{p}}$, where $\hat{\boldsymbol{p}}$ is the unit vector. This compact form is simple to understand but in order to increase the efficiency of the optimisation for calculating the derivatives with respect to rotation, we transform this into a rotation matrix $\mathbf{R}$. A rotation matrix is an orthonormal 3 by 3 matrix comprised of 3 perpendicular vectors. To perform a rotational operation we multiply the orientational vector $\boldsymbol{v}$ by $\mathbf{R}$ to obtain $\boldsymbol{v}'$.

$$\mathbf{R} = \begin{bmatrix} u_x & v_x & w_x \\ u_y & v_y & w_y \\ u_z & v_z & w_z \end{bmatrix}$$

To calculate the rotation matrix from the angle axis from an angle axis vector $\boldsymbol{p}$ we can use Rodrigues' rotation formula:

$$\mathbf{R} = \mathbf{I} + (1 - \cos\theta)\tilde{\boldsymbol{p}}\tilde{\boldsymbol{p}} + \sin\theta\tilde{\boldsymbol{p}}$$

where $\mathbf{I}$ is the identity matrix and $\tilde{\boldsymbol{p}}$ is the skew-symmetric matrix:

$$\tilde{\boldsymbol{p}} = \frac{1}{\theta}\begin{pmatrix} 0 & -p_3 & p_2 \\ p_3 & 0 & -p_1 \\ -p_2 & p_1 & 0 \end{pmatrix}$$

2.5 Particle Movement and Equations of State

When simulating particles undergoing Brownian motion some level of coarse-graining can be undertaken, without which the simulation time needed for the evolution of the system would be restrictive [122]. The appropriate level of coarse-graining will differ depending on the properties the scientist wishes to observe. We are primarily interested in the dynamics of the larger colloidal particles; the evolution and structural properties of the solvent, which are many orders of magnitude smaller than the colloids, are typically not tracked [123]. Instead, the force of the constant stochastic collisions of the solvents with the larger particles is described in the Langevin equation, 2.11, as $\boldsymbol{\xi}_i$. The Langevin equations for translation and rotation, shown in equations 2.11 and 2.12 respectively are used to describe Brownian motion. In these equations, the superscript tr signifies translational components, while rt denotes rotational.

$$m_i \frac{d\boldsymbol{v}_i}{dt} = -\zeta^{tr}\boldsymbol{v}_i + \boldsymbol{F}_i(t) + \boldsymbol{\xi}_i^{tr}(t) \tag{2.11}$$

$$I_i \frac{d\boldsymbol{w}_i}{dt} = -\zeta^{rt}\boldsymbol{w}_i + \boldsymbol{T}_i(t) + \boldsymbol{\xi}_i^{rt}(t) \tag{2.12}$$

Here, m is the mass of the colloid, $\boldsymbol{v}$ and $\boldsymbol{w}$ are the translational and orientational velocity at time t respectively, ζ^{tr} and ζ^{rt} are the translational and rotational coefficients of friction respectively, $\boldsymbol{F}_i(t)$ and $\boldsymbol{T}_i(t)$ the force and torque applied to particle i,

and $\boldsymbol{\xi}_i(t)$ is the contribution of the solvent particles random collisions to the translation and rotation of the larger colloidal particle and I is the moment of inertia. The friction terms, ζ, are related to the diffusion coefficients through the Einstein equations:

$$D = \frac{k_B T}{\zeta} \tag{2.13}$$

, where k_B and T are the Boltzmann constant and temperature respectively.

The force and torque terms are described below in equations 2.14 and 2.15, and are dictated by the derivative of the potential used. Another level of coarse-graining is used here through the use of pair potentials, where we neglect N-body interactions where $N > 2$. This common coarse-graining technique provides considerable speedup and the contribution from $N > 2$-body interactions is factored in the effective pair potential [122].

$$\boldsymbol{F}_i = -\boldsymbol{\nabla}_{\boldsymbol{r}_i} \sum_{j \neq i} V_{ij}(\boldsymbol{r}_{ij}, \boldsymbol{e}_i, \boldsymbol{e}_j) \tag{2.14}$$

$$\boldsymbol{T}_i = -\boldsymbol{e}_i \times \boldsymbol{\nabla}_{\boldsymbol{e}_i} \sum_{j \neq i} V_{ij}(\boldsymbol{r}_{ij}, \boldsymbol{e}_i, \boldsymbol{e}_j) \tag{2.15}$$

where V_{ij} is the interaction potential while $\boldsymbol{e}_i$ and $\boldsymbol{e}_j$ describe the orientations of the particles, where applicable.

The Brownian dynamics method does not use the inertia of the colloidal particles, as the forces from the viscous solvent are assumed to damp the momentum of the larger colloidal particles. This framework is referred to as 'overdamped'. The movement of the particles can therefore be evolved using the following equation in the overdamped

limit, neglecting hydrodynamic effects:

$$\boldsymbol{x}(t+\Delta t) = \boldsymbol{x}(t) + \left(-\frac{D_0^{tr}}{k_B T} \nabla (V(\boldsymbol{x})) + \boldsymbol{\xi}_{tr} \right) \Delta t \tag{2.16}$$

where $\boldsymbol{x}$ is the particle position, D_0^{tr} = translational diffusion coefficient at infinite dilution, $\nabla(V(\boldsymbol{x}))$ is the force on the particle, and $\boldsymbol{\xi}_{tr}$ is the random translational force. The red terms are due to particle-particle interactions while the blue terms are from interactions with the solvent particles.

The orientation of the particles is propagated using:

$$\boldsymbol{e}_i(t+\Delta t) = \boldsymbol{e}_i(t) + \frac{D_0^{rt}}{K_B T} \Delta t \boldsymbol{T}_i(t) \times \boldsymbol{e}_i(t) + (\boldsymbol{\xi}_{rt}) \times \boldsymbol{e}_i(t) \tag{2.17}$$

Here D_0^{rt} and $\boldsymbol{\xi}_{rt}$ are the rotational diffusion coefficient and random rotational force respectively. The diffusion constants at infinite dilution are given by Stokes law for translational and rotational diffusion respectively:

$$D_0^{tr} = \frac{k_B T}{3\pi\eta\sigma}$$

$$D_0^{rt} = \frac{k_B T}{\pi\eta\sigma^3}$$

where η is the viscosity coefficient of the solvent, and σ the colloidal particle diameter.

The random displacement terms above describe the influence of the frequent collisions of the smaller particles, causing the larger colloids to rotate and translate. This random force is undirected as the assumption of the model is that there is no order to which the solvents collide with the larger particle. This force is also described as 'memoryless' in that only the current state of the system is relevant to calculate the following step [124]. We generate these displacements from a Gaussian distribution

with means and covariances detailed below:

$$\langle \xi^{tr} \rangle = 0, \quad \langle \xi^{rt} \rangle = 0$$

$$\langle \xi_i^{tr} \cdot \xi_j^{tr} \rangle = 2\Delta t D_0^{tr} \delta_{ij}, \quad \langle \xi_i^{rt} \cdot \xi_j^{rt} \rangle = 2\Delta t D_0^{rt} \delta_{ij}$$

We use a soft matter program called `PASSION`, software developed in-house to calculate our Brownian dynamics trajectories [125].

2.6 Global Optimisation

As well as investigating the Brownian dynamics of colloidal systems, in this thesis we explore the potential energy surface to identify global minima. Here, the potential energy surface refers to a multidimensional surface that describes how the potential energy varies as variables such as the particle positions and orientations are manipulated. As an example, for a system of two isotropic particles in one dimension, interacting purely through a distance-based potential such as Lennard-Jones, the only variable that will change the potential energy of these particles will be the distance between them. As such, the system can be described with a one dimensional potential energy.

An example representation of a potential energy surface is shown in figure 2.5, where we have labelled points of interest. Here, $\boldsymbol{x}$ is a vector that contains all the coordinates of the system, and $V(\boldsymbol{x})$ is our potential energy function. Points at which the change in potential energy is 0 with respect to our variable $\boldsymbol{x}$, $\nabla V(\boldsymbol{x}) = 0$, are called stationary points. These stationary points are of significance as the force of the system, F, is equal to $-\nabla V(\boldsymbol{x})$, and so parameter space with $\nabla V(\boldsymbol{x}) = 0$ corresponds to systems where the force acting on the system is also 0, suggesting these structures are in mechanical *equilibrium*.

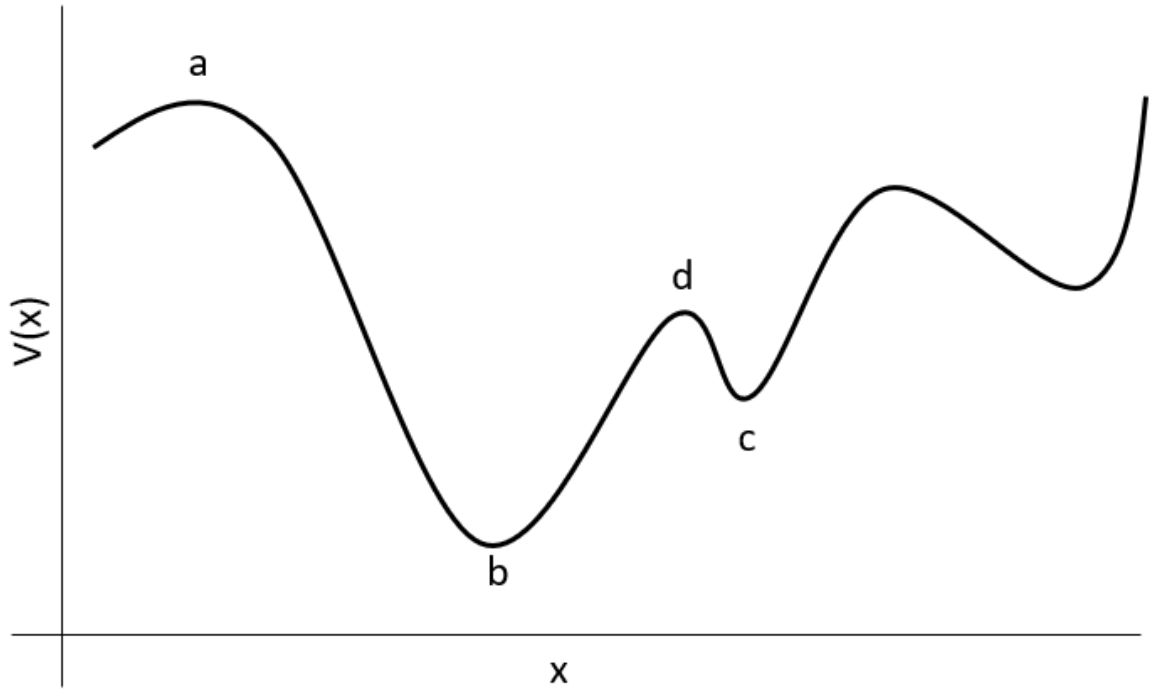

Figure 2.5: An example potential energy surface, with labelled stationary points (a, d) and minima (b,c).

These stationary points, labelled a-d in figure 2.5, can be differentiated by calculating the second derivative with respect to $\boldsymbol{x}$, at which point minima will be identified with only positive second derivatives (b,c) and maxima, or saddle points, can be classified with a negative second derivative (a,d). If we again discuss the relationship between force and potential energy, these minima on the potential energy are regions of parameter space that when small displacements are applied, the system will attempt to 'correct' itself or minimise back into the state from before. These systems can be described as mechanically *stable*.

Typically the second derivative is referred to as the Hessian matrix, shown in equation 2.18.

$$H_{ij}(\boldsymbol{x}) = \frac{\partial^2 V(x)}{\partial x_i \partial x_j} \tag{2.18}$$

Stationary points where all second derivatives are positive are minima, which is mathematically equivalent to a Hessian matrix with no negative eigenvalues. Other stationary points are referred to as n-th order saddle points, where n is the number of negative Hessian eigenvalues, or negative second derivatives.

Now that we are able to describe a position on the potential energy surface, we describe a method called 'basin hopping' to locate the potential energy minima. This method performs a hypersurface deformation, where each point $\boldsymbol{x}$ on the potential energy surface V is mapped to the nearest local minimum. We then use a Monte Carlo-like 'walk' to transition between these regions of the reduced surface. This deformation is shown in figure 2.6. This transition process is described below:

1. Perturb the system

2. Local minimisation

3. Accept or reject perturbed configuration

The perturbation involves translational and rotational displacements, the initial size of which is an input parameter for the algorithm. In step 2 we use the limited-memory Broyden-Fletcher-Goldfarb-Shanno (L-BFGS) minimiser to reach local minima, a quasi-Newton method for which interested readers are directed towards reference [126]. This provides us with two energies - the initial, V_a, and post-minimisation, V_b. If the post-minimisation energy is lower than the initial, $V_b < V_a$, the move is accepted and subsequent proposed moves are made from this new configuration. However, if the energy is greater we use the Metropolis criterion where the 'upwards' step in energy is accepted if $\xi < \exp[\Delta V/(k_B T)]$, where ξ is a uniformly distributed random number between 0 and 1. Here, T is a fictitious temperature which the user defines to adjust the probability of accepting these 'unfavourable' steps, in order to increase the area of

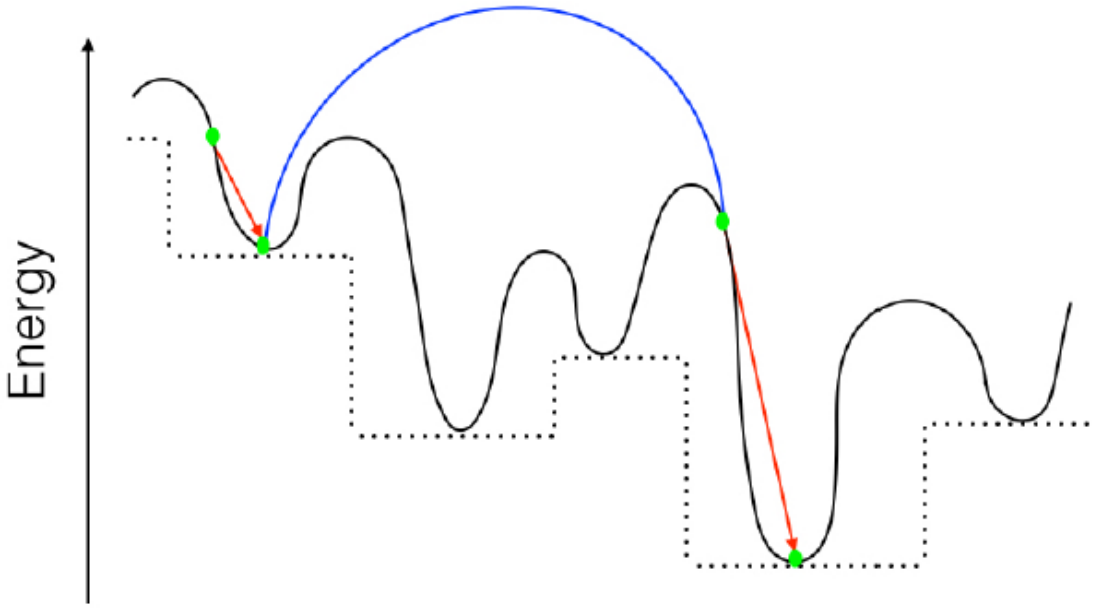

Figure 2.6: A representation of the hypersurface deformation to permit basin-hopping (dashed line), local minimisation (red) and perturbation steps (blue) along the potential energy surface (black). Reproduced from Morphew [127].

the potential energy landscape explored. This cycle constitutes a single 'step' in the program. We typically begin the simulation with a random distribution of particles.

2.7 Simulation Improvements

In order to increase the number of particles in each simulation that we investigated, throughout the degree various improvements to the `PASSION` simulation framework were implemented. Increasing the number of particles in each simulation allows us to probe the effect of the simulation size on the trajectories followed, and investigate multiple crystallisation events in the same system.

In order to reduce the CPU time needed to run the simulations, we must reduce the number of expensive mathematical operations undertaken. In all simulations we use

a radial cutoff for the pairwise particle potential energy calculations. The square root function is typically one of the slowest arithmetic operations and so when calculating inter-particle distances via $\boldsymbol{r_{ij}} \bullet \boldsymbol{r_{ij}} = ||r_{ij}||^2$, we compare the squared value with the squared value of the radial cutoff, R_C [122]. This cutoff is set where the potential energy contribution at that distance is negligible and no greater than that of the numerical precision of the computer variable it is stored in, in the order of 10^{-10}. Using this cutoff reduces the number of potential energy calculations drastically for the short-ranged potentials used in this thesis. However, there are additional steps that can be taken to improve the speed of the simulation without impacting on the numerical stability of the system.

2.7.1 Verlet Neighbour List

Using a neighbour list we can reduce the number of particle-particle distances that are calculated. As well as the interaction 'shell' defined by using a distance cutoff, we introduce a second shell of a greater distance R_N. Particles in this wider shell do not currently interact with the chosen particle. As the system evolves the particles move around, with the maximum displacement of *any* particle since the construction of the neighbour list , $|\mathbf{R_{max}}|$, tracked. Particles that are in the wider shell can move close enough to contribute to the potential energy, and those within the initial cutoff can migrate out, but crucially when $|\mathbf{R_{max}}| \geq R_N - R_C$ the neighbour list is recalculated. This means that no particle can move from outside the neighbour shell to inside the cutoff without triggering a regeneration of the neighbour list where it will be included. A schematic showing the neighbour list calculations is shown in figure 2.7a.

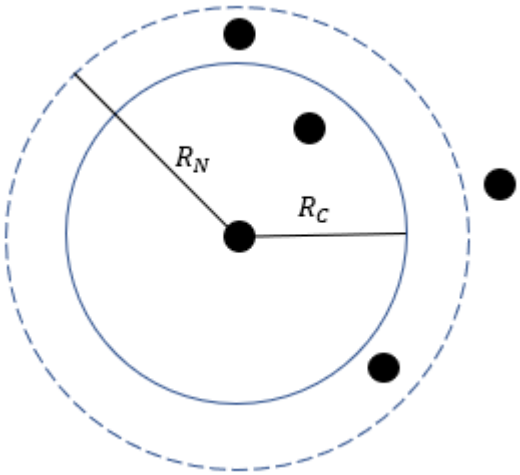

[b]

(a) Neighbour list

[b]

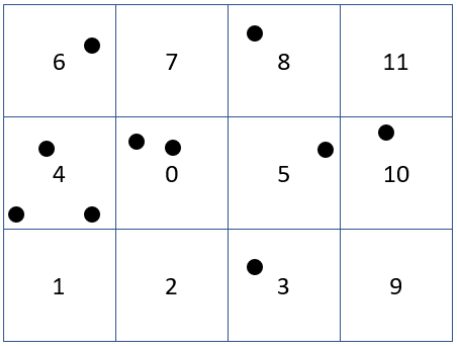

(b) Cell list

Figure 2.7: a) Schematic showing the neighbour list for a single particle. b) 2D schematic showing various environments for a cell list implementation.

2.7.2 Cell List

An alternative to neighbour list is the cell list, where the simulation space is partitioned into equally sized cells. These cells, which in our system are cubic but are not required to be so, have dimensions $c_a = c_b = c_c \geq R_C$. A particle in cell 0 in figure 2.7b will only interact with the cells directly neighbouring it, cells 1-8. The figure is shown in 2D for clarity. When calculating potential energy we can therefore be sure that only particles inside the current cell and those of its neighbours will contribute, as all other cells are too far away.

2.7.3 OpenMP

As discussed above, continued development in computer hardware has rapidly extended the computational power available to the theorist. The significant investment by institutions into massive multi-core supercomputers has lead to the development of parallel

programming libraries better able to utilise this power. Two such libraries, OpenMP and OpenMPI, were used to extend `PASSION` from a single process executable to one which can be run over 100s of CPUs across various nodes in a supercomputing facility. OpenMP boasts an ease of implementation where serial code can be wrapped with *directives*. These directives are commented code around loops that the compiler interprets and automatically generates the required parallel code. In this way the programmer can simply add or remove a compiler flag to swap from serial to parallel executable creation.

In both OpenMP and OpenMPI the same terminology is used for distributing workloads. We used the master-worker approach, where the 'master' thread will spawn 'slave' or 'worker' threads that perform operations in parallel and return a variable, or list of variables, to the master to be consolidated with the other worker's results. When transitioning from a single- to multi-process program the developer must consider the implications of memory management and randomness. For shared memory approaches, such as OpenMP, the developer has control through the use of *attributes* such as *shared* and *private* to enforce correct memory usage. Private variables are stored in separate memory locations for each thread and so will not suffer from race conditions, where multiple threads are trying to access or update the same memory at once and the order they complete would impact the end result. However, the creation and destruction of private variables within the worker threads does create overhead, a slowdown or setup cost, when initialising. Shared memory, by contrast, is accessible to each worker thread at the same memory location. As this memory is already allocated the overhead is significantly cheaper, but as mentioned care must be taken when updating this variable inside the parallel regions. The programmer may use directives such as *atomic* to force only a single thread at a time to operate a section of code, or

flush to update all threads to the shared memory value.

An example usecase for our Brownian dynamics code for private and shared memory is the potential energy calculation step. Here, the chosen particle identifiers, i and j can be private, as each thread will be operating on different pairs and so will need a different value for i and j. However the arrays of particle positions and orientations can be passed as shared variables, as they will not be updated and are the same for each thread. This reduces the overhead of creating the threads and reduces the memory footprint, as only one copy of the positions and orientations is allocated for the program. At the end of the calculation, the potential energy and other variables will be passed back to the master thread.

2.7.4 OpenMPI

While initial speed up was observed after implementing neighbour list with OpenMP, in order to maximise the number of particles that we can simulate in a realistic timeframe we developed an MPI compatible version of `PASSION` with cell list. Compared to the shared memory approach OpenMP, MPI is a distributed memory framework where each thread manages their own storage of data. Similar master-worker methodology can be used here, where the master thread will broadcast the input variables for the task that the worker nodes need to operate with, and will then wait for their responses. As all memory is managed by the threads, the worker nodes can be distributed to different hardware, overcoming the limitation of OpenMP of operating on a single computer. The downside to this approach is the introduction of overhead for broadcasting and receiving data, and that the changes to the codebase for implementing OpenMPI are much more significant than for OpenMP.

2.7.5 Visualisation Suite

Alongside the expansion of the computational framework and analysis programs, a visualisation program, UniVis [128], was developed in order to provide high detail, accurate representations of our system post-simulation. Previous methods to produce high-quality representations of the simulation snapshots used PovRay, a raytracing program [129]. Whilst this method produced publication-grade images, the time taken to render each image, around 10 minutes for large systems, did not provide real-time feedback. UniVis uses the raw positions and orientation files, custom 3D meshes and is easily extendable through C# scripting in the Unity3D framework.

2.8 Simulation Protocols

The details of the simulation performed in each system are detailed below, in table 2.1. Global Optimisation calculations were performed on desktop workstations with i7-6700 CPU @ 3.40GHz processors. For the Brownian Dynamics simulations we used BlueBEAR, the University of Birmingham's HPC facility, and Athena/HPCM+, a Tier 2 computing facility. Information on this BlueBEAR can be found here. The simulations were performed on Intel Broadwell servers, using 7 of the 20 available cores for `MPI PASSION`. More information on the BlueBEAR configuration can be found here. Athena/HPCM+ provides Intel Xeon E5-2680v4 at 2.40 GHz servers with 128 GB of memory. Simulations were run using 7 cores for `MPI PASSION`. The time units used are in reduced units, $t = \frac{\sigma^2}{D_0^t}$, where σ is the diameter of the particle and D_0^t is the translational diffusion coefficient at infinite dilution. The systems were equilibrated at $T^* = 1$ from an initial face-centered lattice and well-separated configurations were chosen as starting points for independent cooling runs. Volume fraction, ϕ, is calculated

from the volume of the spheres, assuming a hard sphere, over the total volume of the system, using the standard equation $\phi = \frac{\pi}{6}\frac{N}{V}$.

For SC and BCC we use the following system parameters: $\epsilon_{AA} = 5, \epsilon_{BB} = 1, \alpha = 85^o, \beta = 40^o, S = 1, \kappa = 100$ following their definition in section 2.3.3. For tetrastack we used the following: $\epsilon_{AA} = 5, \epsilon_{BB} = 1, \alpha = 80^o, \beta = 40^o, S = 5, \kappa = 100$.

2.9 Analysis of crystal structures

Alongside traditional methods for identifying long-range order, such as analysis in terms of radial distribution functions and structure factors, various methods have been developed to 'fingerprint' crystal structures. One such method is through the calculation of the Steinhardt order parameters, q_l [130]. These order parameters are widely used in literature for the analysis of crystal structures, and have become the standard method of identification [131, 132, 133, 134]. Often referred to in literature also as bond order parameters (BOPs), bond-orientational order parameters (BOOs), the Steinhardt order parameters describe the local environment of a chosen particle, providing quantitative measures. These values for particles in a known perfect crystal are typically documented for comparison. In practice, distributions of q_l values sampled at thermal equilibrium are compared with the corresponding reference distributions [135].

In this approach, the neighbours of a particle i are identified to be all particle j located within a separation r_c, and there exists a bond between particles i and j, whose orientation is defined by $\hat{\boldsymbol{r}}_{ij}$, the unit vector of the separation vector $\boldsymbol{r}_{ij}$. If $N_b(i)$ is the number of neighbours of particle i, then its local environment is characterised by

$$q_l(i) = \sqrt{\frac{4\pi}{2l+1}\sum_{m=-l}^{l}|q_{lm}|^2} \tag{2.19}$$

$N = 864$ BCC	T^*	1	0.8	0.5	0.4	0.2	0.16	0.15	
	t	100	200	100	100	100	200	200	
$N = 864$ BCC 'Instant Quench'	T^*	1	0.2						
	t	100	200						
$N = 864$ SC	T^*	1	0.8	0.6	0.5	0.4	0.3	0.28	0.26	0.24
	t	100	100	100	100	100	200	200	200	200
	T^*	0.22	0.2	0.18	0.16	0.15	0.14			
	t	200	200	200	600	200	200			
$N = 864$ SC 'Instant Quench'	T^*	1	0.2	0.15						
	t	t	800	1400						
$N = 8788$ SC	T^*	1	0.8	0.6	0.5	0.4	0.3	0.28	0.26	0.24
	t	t	100	100	100	100	200	200	200	200
		0.22	0.2	0.18	0.16					
		200	200	200	550					
$N = 864$ TD	T^*	1	0.8	0.6	0.5	0.4	0.3	0.2	0.19	0.18
	t	40	40	40	40	80	80	80	80	80
	T^*	0.17	0.16	0.1575	0.155	0.1525	0.15	0.14		
	t	80	80	80	80	80	1920	80		
$N = 4000$ TD	T^*	1	0.8	0.6	0.5	0.4	0.3	0.2	0.19	0.18
	t	40	40	40	40	80	80	80	80	80
	T^*	0.17	0.16	0.1575	0.155	0.1525	0.15	(0.145)		
	t	80	80	80	80	80	860	460		

Table 2.1: Table documenting the simulation protocols followed for Brownian Dynamics calculations. For BCC, the simulations were performed on BlueBEAR. For Simple Cubic (SC), the simulations were performed on Athena/HPCM+. For Tetrastack (TD), the simulations were performed on Athena/HPCM+. T^* is the reduced temperature and t is the reduced time unit. The final step in the $N = 4000$ at 0.145 T^* was ran in parallel to the simulation at 0.15 T^*, branching off after 460 t. This is explained in detail in chapter 6.

	BCC $Im\bar{3}m$		FCC $Fm\bar{3}m$	HCP $P6_3/mmc$	Simple Cubic $Pm\bar{3}m$
	$n = 8$	$n = 14$	$n = 12$	$n = 12$	$n = 6$
q_2	0	0	0	0	0
q_3	0	0	0	0.076	0
q_4	0.509	0.036	0.19	0.097	0.764
q_5	0	0	0	0.252	0
q_6	0.629	0.511	0.575	0.484	0.354
q_7	0	0	0	0.311	0
q_8	0.213	0.429	0.404	0.317	0.718
q_9	0	0	0	0.138	0
q_{10}	0.65	0.195	0.013	0.01	0.411
q_{11}	0	0	0	0.123	0
q_{12}	0.415	0.405	0.6	0.565	0.696

Table 2.2: Table of q_l values from perfect crystals: BCC, FCC, HCP and Simple Cubic. n is the number of neighbours considered for each value calculated. For BCC crystal, the set of second nearest neighbours can be excluded from consideration or included ($n = 8$ and 14, respectively). Table adapted from Mickel *et al.* [134].

where

$$q_{lm}(i) = \frac{1}{N_b(i)} \sum_{j=1}^{N_b(i)} Y_{lm}(\hat{\boldsymbol{r}}_{ij}), \tag{2.20}$$

Here, $Y_{lm}(\hat{\boldsymbol{r}}_{ij}) \equiv Y_{lm}(\theta_{ij}, \phi_{ij})$ are the spherical harmonics corresponding to the polar and azimuthal angles, θ_{ij} and ϕ_{ij}, respectively, of the bond $\boldsymbol{r}_{ij}$ between particle i and its neighbour j.

These q_l values depend on the angle between the points of interest, which for our system are the neighbouring particles within bonding distance, and are independent of a reference frame [135]. Typically, q_4 and q_6 are used as they can distinguish for hexagonal and cubic structures, though values from $l = 2 \rightarrow 12$ are used in literature [134]. Ideal q_l values are shown in table 2.2.

Bond order parameters are used to qualify a particle as 'solid' by comparing its local environment with that of its neighbours. If a particle is in the same environment as a set

fraction of its neighbours, typically 2/3, then the particle can be considered solid-like. When following the nucleation and growth of Lennard-Jones crystals through molecular dynamics, ten Wolde *et al.* used the scalar product S to quantify the similarity of a particle's q values to those of their neighbours [132]:

A normalised $2l+1$-dimensional complex vector $\mathbf{q}_i$ is assigned to every particle i with components

$$\tilde{q}_{lm}(i) = \frac{q_{lm}(i)}{\left[\sum_{m=-l}^{l} |q_{lm}(i)|^2\right]^{1/2}} \tag{2.21}$$

such that

$$\tilde{\mathbf{q}}_i \cdot \tilde{\mathbf{q}}_i = \sum_{m=-l}^{l} \tilde{q}_{lm}(i)\tilde{q}_{lm}(i)^\star = 1 \tag{2.22}$$

For two particles i and j, the real part of the scalar product $\tilde{\mathbf{q}}_i \cdot \tilde{\mathbf{q}}_j$, S_{ij}, thus provides a measure of how similar their local environments are. ten Wolde *et al* used a threashold value of $S_{ij} > 0.5$ to established a "connection" between particle i and its neighbour j, with particles with over 7 connections being deemed as 'solid-like' [132].

As well as obtaining a measure of the local environment of individual particles, a global bond order parameter Q_l can be used to describe the entire system [132]:

$$Q_l(i) = \sqrt{\frac{4\pi}{2l+1} \sum_{m=-l}^{l} |Q_{lm}|^2} \tag{2.23}$$

where

$$Q_{lm}(i) = \frac{\sum_{i=1}^{N} N_b(i) q_{lm}(i)}{\sum_{i=1}^{N} N_b(i)} \tag{2.24}$$

While the Steinhardt order parameters in their original form are still extensively used in literature, Lechner and Dellago put forward a modification to consider average

local bond order parameters in the following form [135]:

$$\bar{q}_l(i) = \sqrt{\frac{4\pi}{2l+1} \sum_{m=-l}^{l} |\bar{q}_{lm}|^2} \tag{2.25}$$

where

$$\bar{q}_{lm}(i) = \frac{1}{\tilde{N}_b(i)} \sum_{k=0}^{\tilde{N}_b(i)} q_{lm}(k). \tag{2.26}$$

Here the sum $\sum_{k=0}^{\tilde{N}_b(i)}$ loops over all neighbours of particle i as well the particle itself. In this approach, one thus takes into consideration the second shell of neighbours in the calculation of the average local bond-order parameters. In the original paper that introduced the modification and throughout this thesis, these averaged local bond order parameters are denoted with an overbar, as shown in equations 2.26 and 2.25 [135]. The extension of the calculation to include the second shell of neighbours allows for more information about the local environment of the particle to be accounted for, leading to often a more effective distinction between different crystal structures as evident in figure 2.8.

Whilst these bond order calculations provide excellent insight into the makeup of the system, their calculation is much more intense than the more simple methods discussed at the start of this section. For quick insight into the state of the system, we generate radial distribution functions and follow the energy of the system to look for discontinuities. We use the orientational order parameter, defined in equation 2.27, to identify octahedral and tetrahedral clusters formed by the triblock patchy particles, thus enabling us to count the number of octahedra and tetrahedra present in the system. For a single particle, we identify the 5 (or 3 for tetrahedra) nearest neighbours, using the minimum image convention. We calculate the geometric centres for these 6 (or 4)

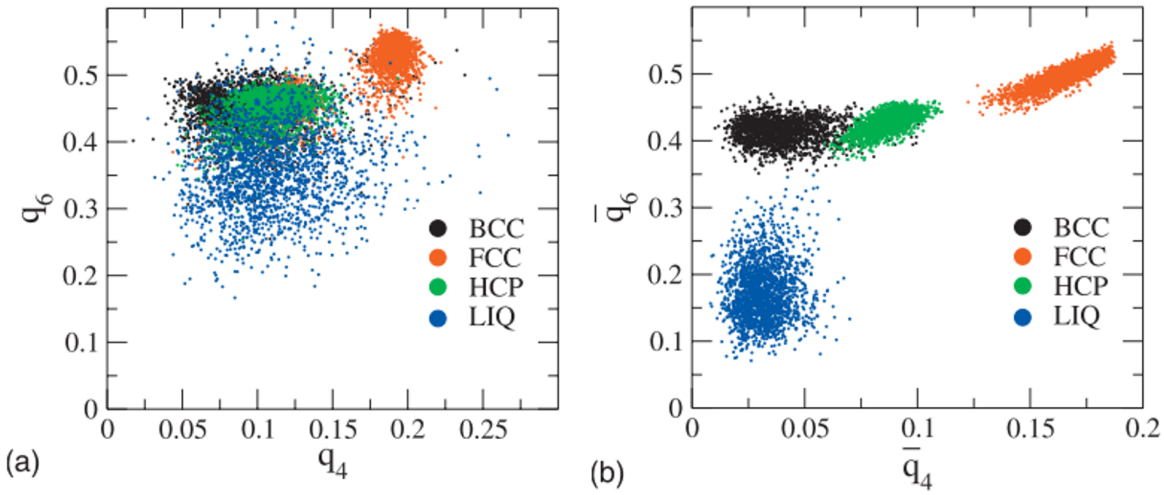

Figure 2.8: Local environments of particles in three crystal structures and the liquid phase for the Lennard-Jones system, using the traditional Steinhardt order parameter (a) and averaged local bond order parameters, as introduced by Lechner and Dellago [135]. Image reproduced from Lechner *et al.* [135].

particles and then calculate the value for q_{ord} using equation 2.27.

$$q_{ord} = 1 - \frac{3}{8} \sum_{j=1}^{N_b-1} \sum_{k=j+1}^{N_b} (\cos \psi_{jk} + \frac{1}{3})^2 \tag{2.27}$$

The values for q_{ord} can range from 1 to -3, with a value for q_{ord} for 6 particles on the vertices of a perfect octahedron at 0 or a value of 1 for 4 particles on the vertices of a tetrahedron [136]. We use a cutoff of $q_{\text{ord}} = 0 \pm 0.02$ to identify our octahedra and $q_{\text{ord}} = 1 \pm 0.01$ for tetrahedra.

Chapter 3

Hierarchical Self-Assembly of Triblock Patchy Particles via Octahedral Colloidal Molecules

3.1 Introduction

Colloidal molecules are capable of offering highly directional interactions and are thus promising building blocks for realising colloidal open crystals via self-assembly - the tunability of these interactions offers a vast parameter space to explore in the hunt for self-assembly pathways [137]. Hierarchical self-assembly pathways via colloidal molecules are appealing from the perspective of their processability; the feasibility of triblock patchy particles forming colloidal molecules with tetrahedral and octahedral symmetry following a staged assembly route is well-established [74]. However, the assembly at the first stage produced a distribution of cluster sizes, which severely reduced the likelihood of realising colloidal crystals in the next stage [74]. Building

on the success of programming two-stage self-assembly of a colloidal crystal from the triblock patchy particles via self-limiting tetrahedral clusters *in silico*, here we investigate the generality of the design principles [79]. In particular, we explore hierarchical self-assembly pathways via octahedral colloidal molecules.

3.2 Method

3.2.1 Global optimisation for a finite system

We began our approach by identifying an optimal set of potential parameters that support distinct octahedral subunits. To this end, we predicted the global minima on the potential surfaces for a finite system of $N = 48$ triblock patchy particles for different sets of parameters, using basin-hopping global optimisation runs. Figure 3.1 shows the global minimum on the potential energy surface corresponding to the following set of parameters: $\epsilon_{\mathrm{AA}} = 5\epsilon_{\mathrm{Y}}$, $\epsilon_{\mathrm{BB}} = 1\epsilon_{\mathrm{Y}}$, $\alpha = 85°$, $\beta = 40°$, $s = 1$ and $\kappa = 100$ where, as defined in section 2.3.3, ϵ_{AA} and ϵ_{BB} are the strengths of the A and B patches respectively, α and β are the patch angles, s relates to the range of the interaction, κ is the inverse Debye screening length and ϵ_{Y} is the Yukawa contact potential. It is apparent that the structure consists of distinct octahedral subunits. Note that the set of parameters, $\epsilon_{\mathrm{AA}} = 5$, $\epsilon_{\mathrm{BB}} = 1$, $\alpha = 80°$, $\beta = 40°$, $s = 5$ and $\kappa = 100$, is known to support distinct tetrahedral subunits [79]. In the present case, a larger width ($85° > 80°$) for the patches forming stronger bonds and a longer range for the patch-patch interactions (a smaller value of s) favour larger coordination for the subunits. The formation of these subunits involves the stronger interactions between the patches. The weaker patches offer valences to these subunits, i.e. octahedral colloidal molecules. Here the weaker patches are narrow enough to allow for only two weaker patches to

optimally interact, forming a single "bond" or contact, thus bringing together two octahedral subunits.

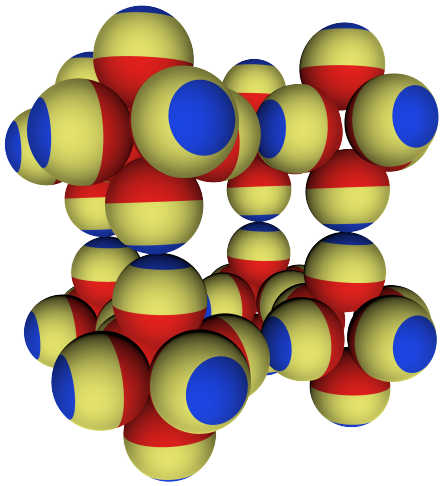

Figure 3.1: A representation of the global minimum for $N = 48$ elementary particles, which form 8 6-membered octahedra through their strong patches and sit on a cubic lattice through their weaker patches.

We next used Brownian dynamics simulations to investigate a system of $N = 864$ triblock patchy particles under periodic boundary conditions. The system, when following the gradual cooling protocol described in table 2.1 in chapter 2, is expected to undergo staged self-assembly, encoded by the use of a hierarchy of strengths for the patch-patch interactions. A question of interest is whether the first-stage of self-assembly occurs in a self-limited way, giving rise to a fluid of monodisperse octahedral clusters exclusively. In both pathways the system begins from a high temperature ($T^* = 1$) melt of a particles on an FCC lattice. For the slower annealing protocol, the temperature is gradually lowered, where each temperature was run for at least 2×10^7 steps with a timestep of 5×10^{-6} yielding a minimum time of 100 τ. The temperatures chosen were to allow the gradual formation of octahedra while the weaker patch is unable to form bonds of significant lifetime. The temperature profile followed was 1.0,

0.8, 0.5, 0.4, 0.2, 0.16, 0.15 T^*, with simulation times listed in table 2.1. We performed eight independent runs. The simulation was performed at a volume fraction of $\phi = 0.3$. In the rapid quenching simulations we simulate four independent runs. We begin from the same equilibrated melt but drop down to $T^* = 0.2$, the temperature at which the weaker patch begins to form bonds of strength strong enough to withstand the thermal displacements.

3.3 Annealing

Figure 3.2 plots the average potential energy per particle against the temperature as we cool the system. The figure also shows the number of octahedral clusters found in the system versus the temperature. This number is averaged over the last 100 'snapshots' dumped along the dynamical trajectory at each temperature, where two successive snapshots are separated by 1000 simulation steps. The method to calculate the number of octahedra present is discussed below.

We use the orientational order parameter, defined in the method chapter and again below in equation 3.1, to identify octahedral clusters formed by the triblock patchy particles, thus enabling us to count the number of octahedra present in the system. For a single particle, we identify the 5 nearest neighbours, using the minimum image convention. We calculate the geometric centres for these 6 particles and then calculate the value for q_{oct} using equation 3.1.

$$q_{oct} = 1 - \frac{3}{8} \sum_{j=1}^{N_b-1} \sum_{k=j+1}^{N_b} (\cos \psi_{jk} + \frac{1}{3})^2 \tag{3.1}$$

The values for q_{oct} can range from 1 to -3, with a value for q_{oct} for 6 particles on the

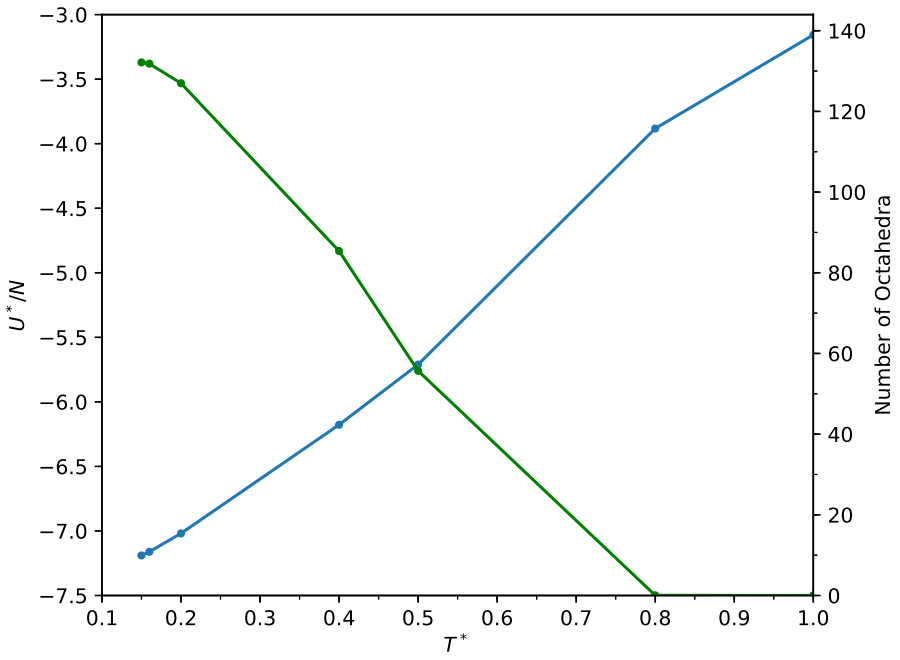

Figure 3.2: Average energy per particle (blue) and number of octahedra (green) throughout the annealing protocol for one configuration, from a single trajectory (shown in blue in figure 3.3).

vertices of a perfect octahedron at 0.[136] We use a cutoff of $q_{\text{oct}} = 0 \pm 0.02$ to identify our octahedra. This cutoff is rationalised from observations reported in chapter 4.

It is evident in figure 3.2 that as the temperature is gradually reduced, the average potential energy per particle falls with a concomitant growth in the number of octahedral clusters. These octahedral clusters are presumably formed via the interaction between wider and stronger patches. It is confirmed by visual inspection of typical configurations. At low temperatures, the number of octahedral clusters rises to a level of saturation around 130, close to the maximum possible value of $N/6 = 144$. However, the average energy per particle continues to fall as the bonds become stronger and the bond lifetime becomes longer. There appears no obvious signature for a second stage of assembly from this plot.

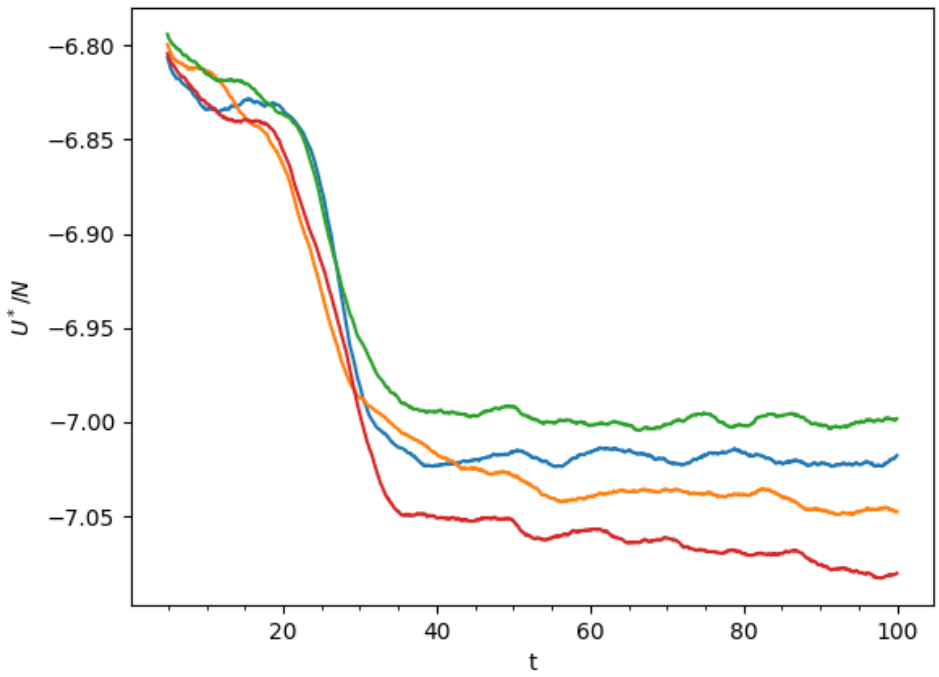

Figure 3.3: Potential energy at $T^* = 0.2$ for four configurations.

Figure 3.3 shows the time evolution of the running average of the potential energy per particle along four independent dynamical trajectories at temperature, $T^\star = 0.2$. The running average of the potential energy per particle at any instant of the time is calculated by taking the average over its last 100 values dumped. A rapid drop in this running average is evident for each of the trajectories over a short time window around $t = 20$, indicating the possibility of a structural transition. We probe this likely structural transition in detail later.

The time evolution of the running average of the potential energy per particle along four additional independent dynamical trajectories at $T^\star = 0.2$ after following the same annealing protocol was also followed, and was largely similar. A snapshot of a typical configuration of the system obtained at this temperature after equilibration is shown in figure 3.4.

We note that from the previous figure 3.2 the number of octahedra at the start

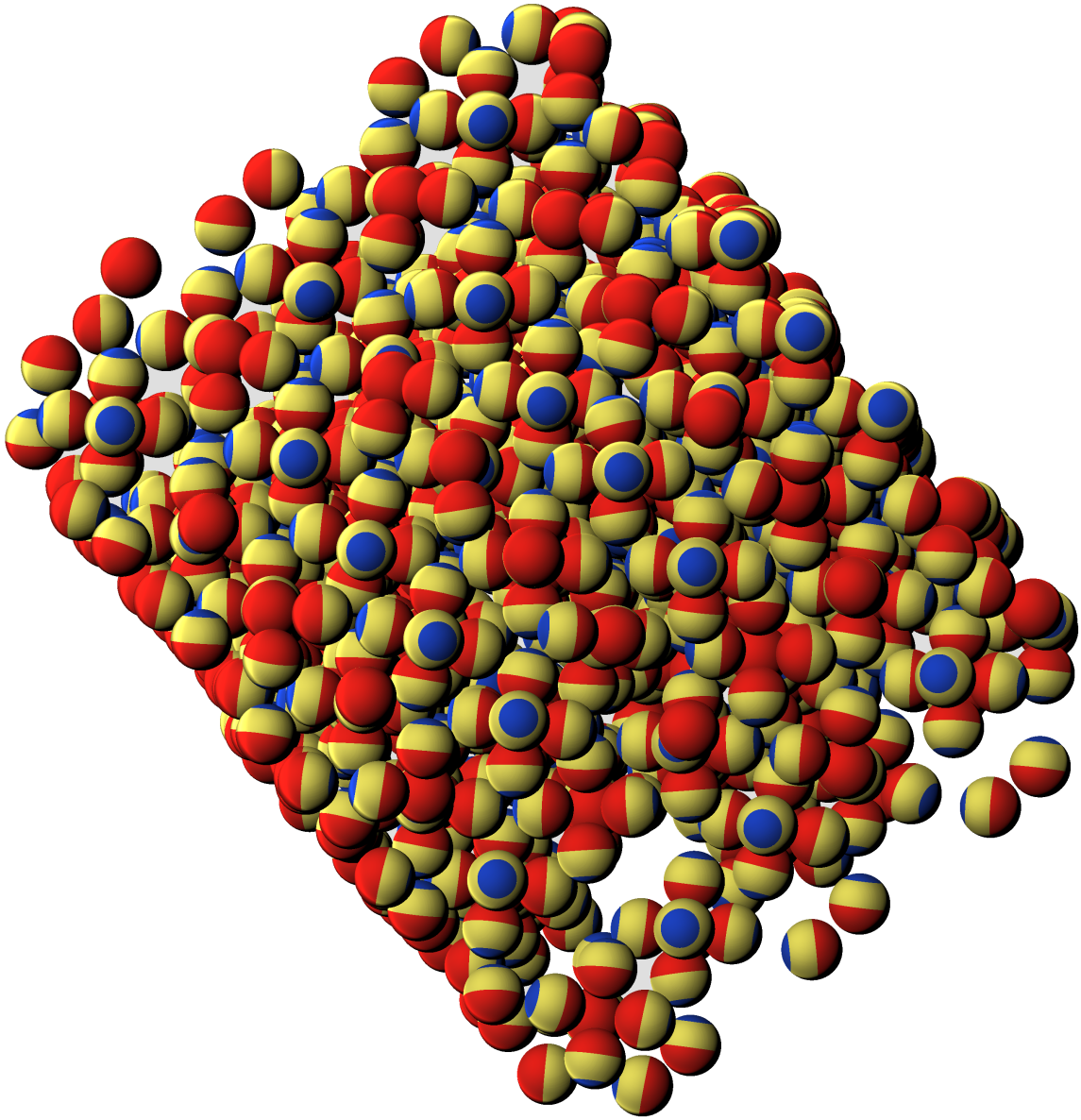

Figure 3.4: A visualisation of the A-B 85-40 system after annealing protocol, showing the crystalline BCC. The cubic simulation box has been rotated to show crystallinity. The yellow band indicates the Yukawa repulsion, with the stronger, wider patches shown in red, and the weaker smaller patches shown in blue.

of this temperature drop is around 90, or $\frac{5}{8}$ of saturation, and does not need a fully saturated system of octahedra to begin the second stage of assembly. We probe this hypothesis further in section 3.4.

Figure 3.5 shows the radial distribution functions for the centres of the octahedral clusters identified to be present in the system at two temperatures studied across $T^\star = 0.2$. The radial distribution function at $T^\star = 0.4$, shown in blue, shows the presence of a short-range order typical of a liquid in the fluid of predominantly of octahedral clusters. At $T^\star = 0.15$, shown in orange, the radial distribution function shows more structured feature, with more pronounced and persistent peaks, indicating the emergence of long-range order. The drop to lower intensities between peaks suggests that the octahedra are sitting at preferred separations akin to solid-like environments.

The peak positions for an ideal crystal can be worked out analytically from the lattice points and compared to those observed in order to help characterise the system. In table 3.1, we compare the values observed to those in the perfect crystal. We see a good match, indicating two-stage self-assembly into a body-centred crystal from the triblock patchy particles via colloidal octahedral molecules.

Ideal	Observed
2.33	2.33
2.70	2.60
3.81	3.85
4.47	4.53

Table 3.1: A comparison between the ideal spacing between lattice points for a BCC crystal, shown in the left column, against the approximate peak positions for our BCC crystal in the RDF shown in figure 3.5. The distances shown for the ideal BCC lattice points have been scaled so that the first distance matches that of the first peak.

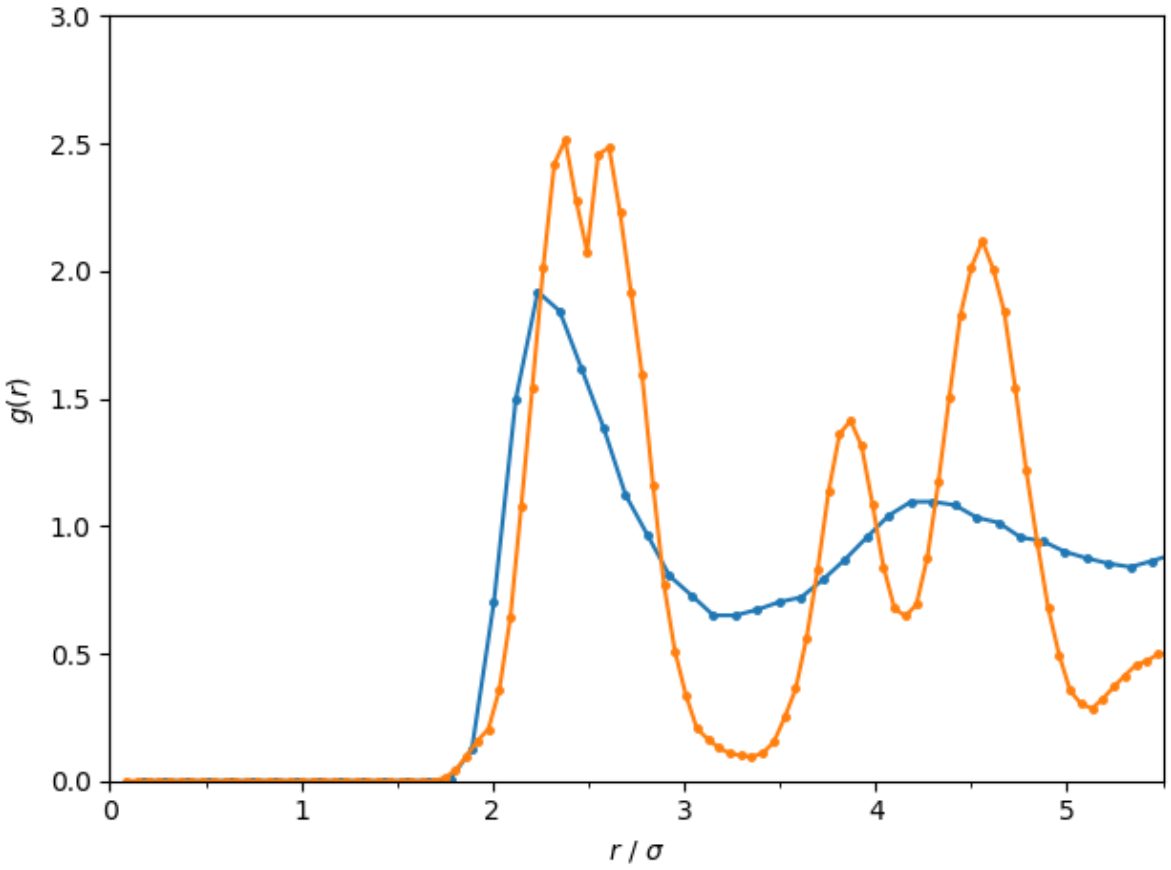

Figure 3.5: Radial distribution function for the centres of octahedra at $T^* = 0.15$ (orange) and $T^* = 0.4$ (blue).

3.3.1 Bond Order Parameters

We confirm our crystal identity by using bond order parameters. These order parameters, used throughout this thesis, let us fingerprint our system by carefully choosing input parameters to compare the local environment to literature values. These order parameters are used widely in literature to classify and quantify colloidal crystallisation [130, 132, 138]. We note that the input parameters to these calculations, such as the use of either a fixed distance cutoff or number of neighbours and use of first or second shell neighbours (q or $\bar{q}$) can make a significant difference to the values obtained and should be justified in full to avoid confusion. This is discussed in detail by Mickel *et*

al [134].

The equations used to calculate the bond order parameter for BCC identification is shown below:

$$q_{lm}(i) = \frac{1}{N_b(i)} \sum_{j=1}^{N_b(i)} Y_{lm}(\hat{\boldsymbol{r}}_{ij}), \tag{3.2}$$

where $N_b(i)$ is the number of neighbours of particle i located within a distance r_{tc} corresponding to the location of the first peak of the radial distribution function, and $Y_{lm}(\hat{\boldsymbol{r}}_{ij}) \equiv Y_{lm}(\theta_{ij}, \phi_{ij})$ are the spherical harmonics corresponding to the polar and azimuthal angles, θ_{ij} and ϕ_{ij}, respectively, of the bond $\boldsymbol{r}_{ij}$ between octahedra i and its neighbour j.

$$\bar{q}_{lm}(i) = \frac{1}{\tilde{N}_b(i)} \sum_{k=0}^{\tilde{N}_b(i)} q_{lm}(k) \tag{3.3}$$

where $\sum_{k=0}^{\tilde{N}_b(i)}$ loops over all neighbours of k + particle i itself.

$$\bar{q}_l(i) = \sqrt{\frac{4\pi}{2l+1} \sum_{m=-l}^{l} |\bar{q}_{lm}|^2} \tag{3.4}$$

Here we use a fixed radial cutoff distance to count the number of neighbours for an octahedral cluster to assign its local environment. This cutoff distance is set at 3.2σ. This value is chosen based on the radial distribution function observed at $T^\star = 0.15$, as seen in figure 3.5. Such a cutoff distance allows for contributions from the 14 nearest neighbours when the particles are sitting on the lattice points. The results of this analysis are shown in figure 3.6 for configurations at $T^\star = 0.4$ and $T^\star = 0.15$. We can compare these results to those in the literature to identify the crystal structure self-assembled in this case to be BCC: $\bar{q}_4$ and $\bar{q}_6$ of 0.05 and 0.425 were observed respectively for an undercooled Lennard-Jones BCC crystal which match well with our low-temperature results shown in green and red, respectively. The distributions at the

higher temperature, shown in blue and orange, are not characteristic of any crystalline structure.

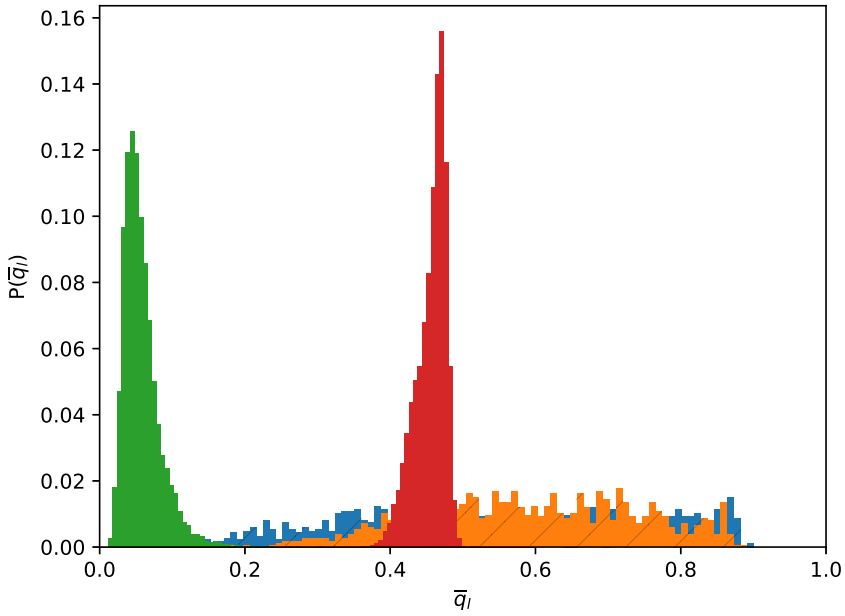

Figure 3.6: Probability distribution for $\bar{q}_l$ bond order parameters for our crystalline system at low temperature ($T^* = 0.15$, $l = 4$ and 6 green and red bars respectively) and liquid at higher temperature ($T^* = 0.4$, $l = 4$ and 6 blue and orange bars respectively).

3.4 Rapid quenching

As well as subjecting the system to gradual annealing protocol, we performed four Brownian dynamics simulations following rapid quenching to lower the temperature of the system down to $T^\star = 0.2$ from $T^\star = 1$. We chose this temperature as we observed crystallisation to occur at $T^\star = 0.2$ upon relatively slow annealing, allowing for octahedral clusters to gradually form and then nucleate into a crystal. At this temperature, the narrower patches that form weaker bonds are able to form bonds with a much greater lifetime. We investigated the possibility that the A-B bonds could

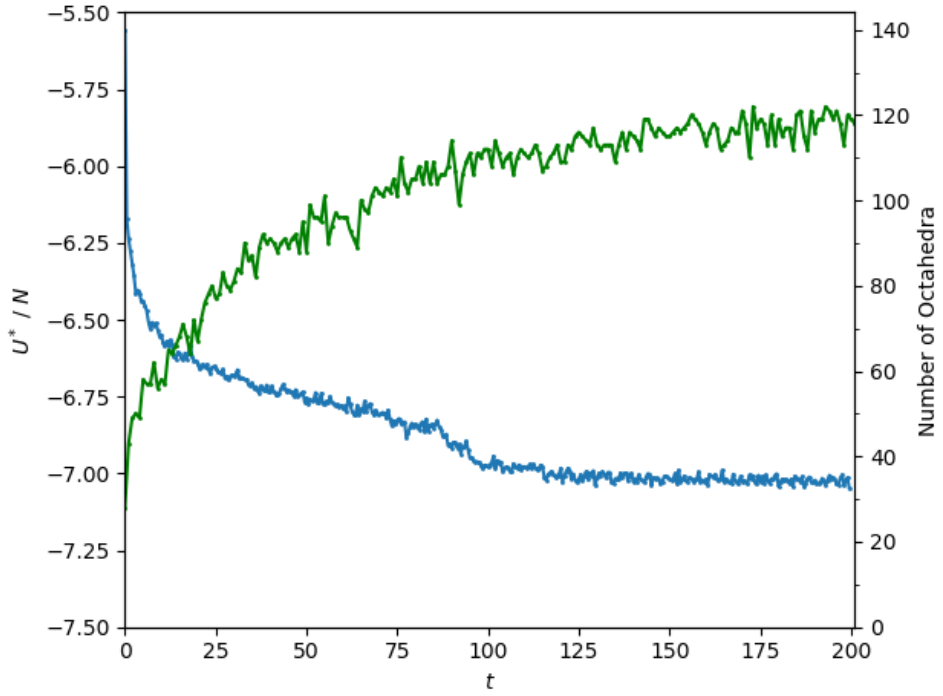

Figure 3.7: Potential energy and number of octahedra at $T^* = 0.2$ from instant quench runs. The small energy discontinuity around $t = 80$ suggests a phase change.

disrupt the formation of octahedral clusters. The likelihood of forming A-B bonds is higher in these rapid quench runs, as in the gradual annealing protocol results in the saturation of the wider patches forming stronger bonds, leaving fewer of them to interact with the narrower patches.

In figure 3.7, we show the average potential energy per particle and the number of octahedral clusters formed along such a dynamical trajectory at $T^\star = 0.2$ upon rapid quenching, beginning at the point at which the temperature was first dropped to $T^\star = 0.2$. Here we can see that immediately after the temperature drop, octahedral clusters begin to form, and the potential energy drops as well. After a rapid drop in U/N, it continues to fall steadily as the number of octahedral clusters rises before showing another drop over a short time window to practically reach a plateu.

It is at this point that the crystallisation occurs. This is confirmed by the analysis

of the bond order parameter presented in figure 3.8. The positions of the peaks after the structural transition confirm that a BCC crystal was formed.

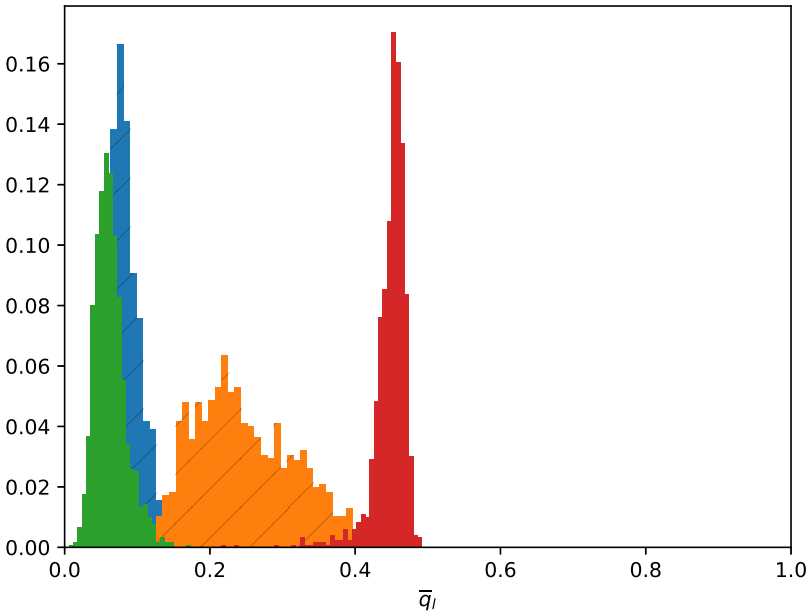

Figure 3.8: BCC bond order parameter for instant quench runs at $T^* = 0.2$. Blue and orange are $\bar{q}_4$ and $\bar{q}_6$ respectively at 75 t, while green and red are $\bar{q}_4$ and $\bar{q}_6$ respectively at 125 t.

3.5 Conclusion

In this study, we identify a set of parameters that facilitates the selective growth of octahedral clusters from triblock patchy particles. This is achieved in the first stage of self-assembly via the interactions between the wider patches, $\alpha = 85^o$, which bind strongly. These octahedra form with very high yield compared to competiting polyhdra due to the selection of appropriate bond angles and strengths, parameters gleaned from global optimisation simulations. Subsequent to the growth of these octahedral colloidal molecules, the weaker patches come into play at lower temperatures to bind the octahedra together, where the geometry of the octahedral clusters dictates the centres of these octahedra sit on a BCC lattice. The narrow patches limit the bonds formed in the second stage of assembly to involve the interactions between only two such patches.

The success of this two-stage self-assembly scheme encoded in triblock patchy particles to yield a crystal via octahedral colloidal molecules further validates the generality of our design principles. Through this design we exploit a hierarchy of interaction strengths to program two-stage self-assembly pathways and the interplay between patch sizes and the range of interactions between patches to make the growth of colloidal molecules self-limiting in the first stage.

The two-stage self-assembly pathways programmed with a hierarchy of strengths for interactions between patches is generally envisaged to be triggered by gradual cooling, to allow for annealing of defects. It is remarkable that in this case even a rapid quenching yields a BCC crystal from triblock patchy particles through hierarchical self-assembly pathways via octahedral colloidal molecules. The presence of long-range patch-patch interactions presumably facilitates the navigation through metastable structures. It should be noted that these longer range attractions between

the designer triblock patchy particles make them realisable in the nanoscale, rather than microscale.

Chapter 4

Crystallisation from Octahedral Colloidal Molecules into an Open Crystal

4.1 Introduction

The simple cubic (SC) crystal, with a packing fraction, ϕ, of 0.52 corresponding to touching spheres along the edges of the cube, is significantly less dense than FCC and HCP crystals, where $\phi = 0.74$. The mean coordination number drops from 12 at close packing to 6 for a simple cubic lattice. Figure 4.1 shows the three Bravais lattices that have a cubic symmetry. Maxwell's mechanical stability criterion, where particles connected with central force bonds in a periodic lattice must have a mean coordination number that equals or exceeds $2d$, d being the dimensionality of the lattice, explains the challenges that realisation of open lattices face from the perspective of thermodynamics [52].

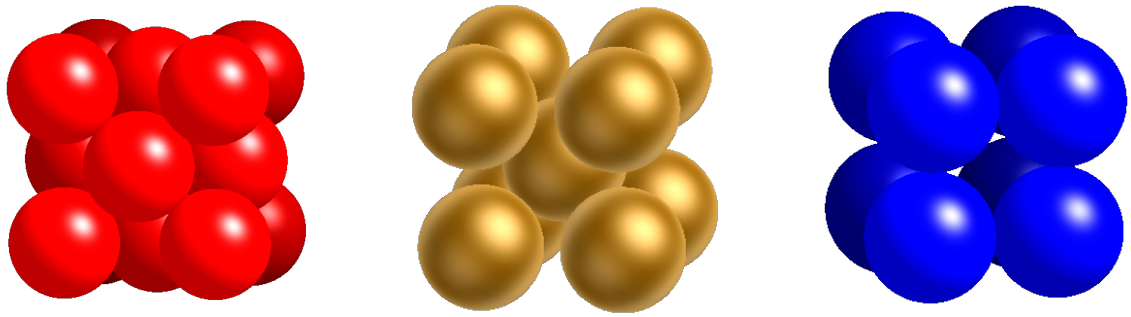

(a) (b) (c)

Figure 4.1: Conventional unit cells of three Bravais lattices of cubic symmetry: (a) face-centred cubic (a), body-centred cubic and (c) simple cubic.

Previous investigations have shown the simple cubic crystal to possess a small photonic band gap of around 5% [139]. However, realisation of the structure on the colloidal scale experimentally has proved to be challenging as with hard-spheres colloids the system collapses into FCC and HCP crystals. Experimental techniques such as photoelectrochemical etching of macroporous silicon to create spherical voids at simple cubic lattice points are able to produce inverse simple cubic structures with band gaps [140]. This route, however, involves expensive and time-consuming fabrication protocol. Moreover, the sensitivity of the photonic properties to small imperfections could result in complete closing of the photonic band gap. Another route to open crystals involves self-assembly pathways in a binary system to overcome the risk of collapsing to close-packed structures. One such attempt used a binary system of oppositely charged colloidal hard spheres to form a caesium chloride structure [30]. This structure is formed of two interpenetrating simple cubic structures of opposite charge, with particles lying on a body-centred cubic lattice. It was suggested that removal of one type of charged particles, an experimentally feasible option, would leave a simple cubic crystal behind [141].

In order to drive the formation of simple cubic crystals we must therefore provide

further motivation for particles to sit on a simple cubic lattice, or dissuade particles from forming BCC. Zanjani *et al.* increase the cost of particles in the central BCC lattice point relative to the simple cubic positions by using colloidal clusters formed of colloids of different particle sizes, along with 'glue' particles [68]. Rossi *et al.* use superspheres, cubes with rounded edges, to provide an entropic penalty to forming BCC over simple cubic [56].

Self-assembly of colloidal particles offers an enticing bottom-up route to colloidal open crystals. In the previous chapter, we have demonstrated that a relatively open colloidal crystal, where octahedral clusters sit on body-centred cubic lattice points, can be self-assembled from designer triblock patchy particles following two-stage assembly pathways. Since a BCC lattice can be envisaged as two interpenetrating simple cubic lattices, a pertinent question is whether hierarchical self-assembly of these triblock patchy particles into a simple cubic crystal structure can be achieved at lower volume fractions and if so whether the self-assembly pathways involve the formation of a BCC crystal as a precursor. These questions are addressed in this chapter.

4.2 Results

We chose to investigate the same designer triblock patchy particles that we studied in the previous chapter. These triblock patchy particles are designed to form octahedral clusters bound by stronger patches. For the same set of parameters, that is $\epsilon_{\mathrm{AA}} = 5$, $\epsilon_{\mathrm{BB}} = 1$, $\alpha = 85°$, $\beta = 40°$, $s = 1$ and $\kappa = 100$, crystal structure prediction by `GlOSP` confirms that a simple cubic crystal structure formed by octahedral clusters is indeed a local minimum on the crystal energy landscape. As defined in section 2.3.3, ϵ_{AA} and ϵ_{BB} are the strengths of the A and B patches respectively, α and β are the patch angles, s relates to the range of the interaction, κ is the inverse Debye screening length and

ϵ_Y is the Yukawa contact potential. Note that here a relatively large patch width for the stronger patch, defined by $\alpha = 85°$ and a longer range for the interaction between patches promote larger coordination, thereby facilitating the formation of octahedral clusters over tetrahedral clusters. Figure 4.2 shows the simple cubic crystal structure that we found.

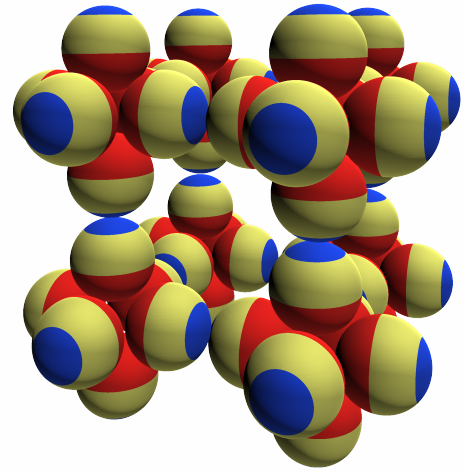

Figure 4.2: Octahedral simple cubic crystal structure formed by designer triblock patchy particles. Here each octahedral cluster formed by the triblock patchy particles sit on simple cubic lattice points.

4.2.1 Simulation Protocols

We next investigate, using Brownian Dynamics simulations, whether a simple cubic crystal can indeed be self-assembled following two-stage assembly pathways and if so our objective is to investigate such pathways in detail to glean mechanistic understanding. To this end, we studied two system sizes, one containing $N = 864$ designer particles and the other with $N = 8788$, at a range of volume fractions within a cubic box under periodic conditions.

We follow a similar annealing protocol to Morphew *et al* where we gradually reduce the temperature of the system once it has equilibrated, where equilibration is

characterised by the potential energy of the system reaching a point where it remains unchanged as the system is evolved over time [79]. We investigated volume fractions, ϕ, of 0.16 - 0.19 in steps of 0.01 for $N = 864$ & 8788 elementary particles. At each volume fraction at least 3 independent runs were started from an equilibrated FCC melt at $T^* = 1.0$. We calculated the number of octahedra and average energy per particle at each temperature step. The temperature protocol followed and timescales are shown in table 2.1.

4.2.2 N = 864

The results for $\phi = 0.17, N = 864$ are shown in figures 4.3 and 4.4. The presence of the octahedra is determined by calculating the order parameter q [142, 136]:

$$q = 1 - \frac{3}{8} \sum_{j=1}^{N_b-1} \sum_{k=j+1}^{N_b} \left(\cos \psi_{jk} + \frac{1}{3} \right)^2 , \tag{4.1}$$

where $N_b = 6$ is the number of particles in the cluster under consideration and ψ_{jk} is the angle subtended at the centre of the cluster by the two vectors joining the centre to particles j and k. In the case of a perfect octahedron, $q = 0$ [136]. In the present study, a range of values 0 ± 0.02 was used, thus allowing for thermal fluctuations, for a cluster of six particles deemed to have formed an octahedron.

Figure 4.3 shows how the average energy per particle evolves as the temperature is gradually reduced. There occurs first a gradual drop in the average energy per particle over a broad temperature range due to the formation of octahedral clusters via the interaction between stronger patches. The concurrent growth in the number of octahedra present in the system approaching the maximum possible value of $N/6$ is also apparent in figure 4.3. As noted previously, the formation of octahedral clusters

in preference to tetahedral clusters is favoured by wider patch width and longer range for the patch-patch interactions, both of which facilitate larger coordination.

Around $T^\star = 0.16$, there appears a weak discontinuity in the average energy per particles, signalling another structural transition. The radial distribution functions, shown in figure 4.4, were calculated across this temperature to investigate this transition. The growth of additional peaks at the lower temperature suggests that crystallisation occurs – a long-range order that was not present at $T^\star = 0.18$ develops in the system at $T^\star = 0.16$.

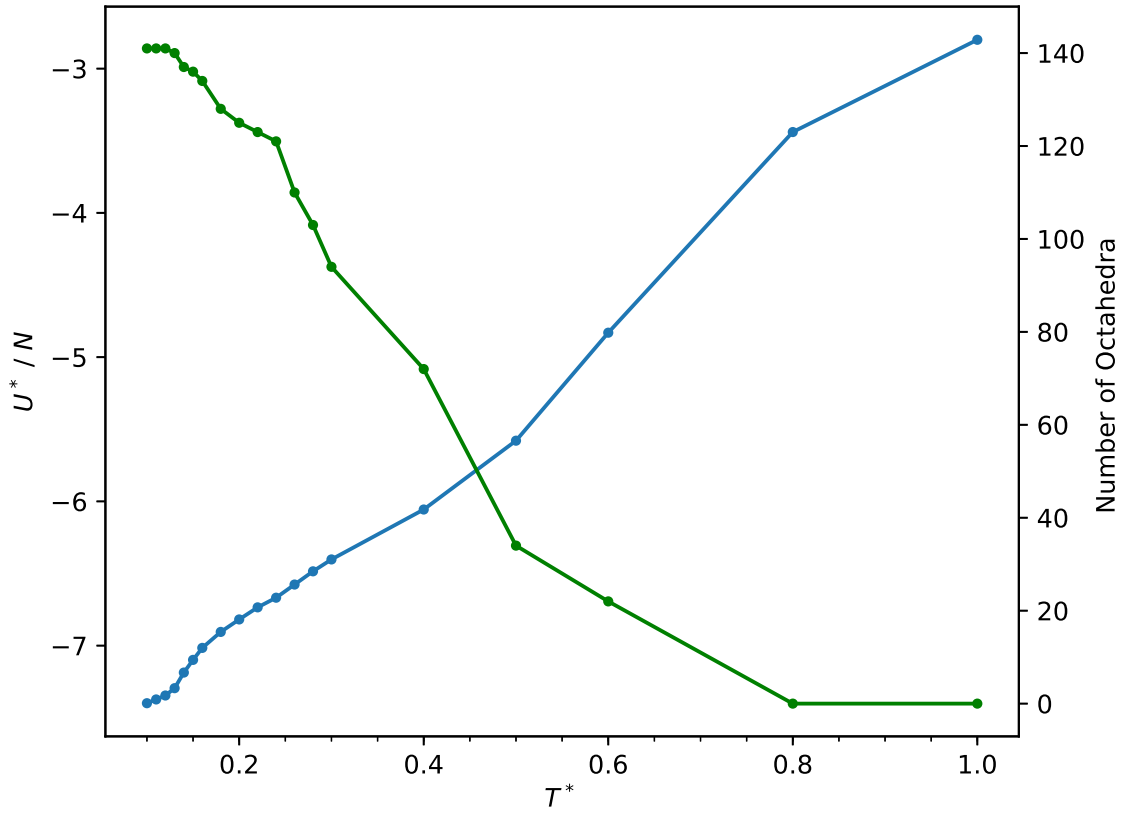

Figure 4.3: Average energy per particle and number of octahedra formed in a system of $N = 864$ triblock patchy particles as a function of temperature.

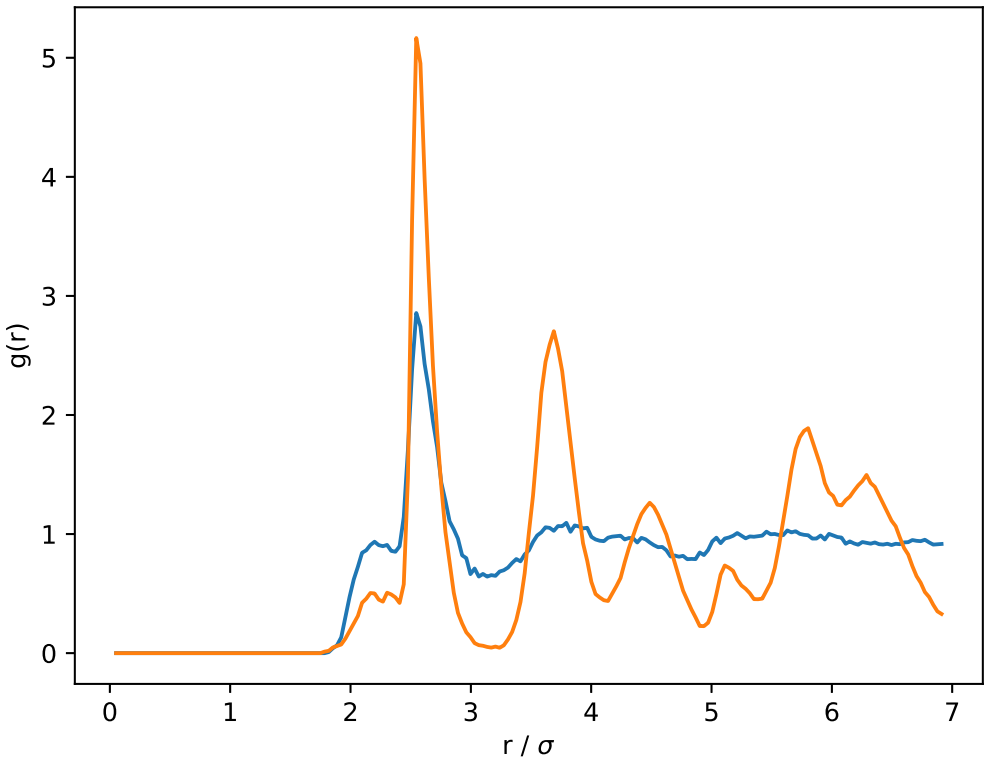

Figure 4.4: Radial distribution functions for the centres of octahedral clusters at two temperatures: $T^\star = 0.18$ (blue) and $T^\star = 0.16$ (orange) for $N = 864$.

4.2.3 $N = 8788$

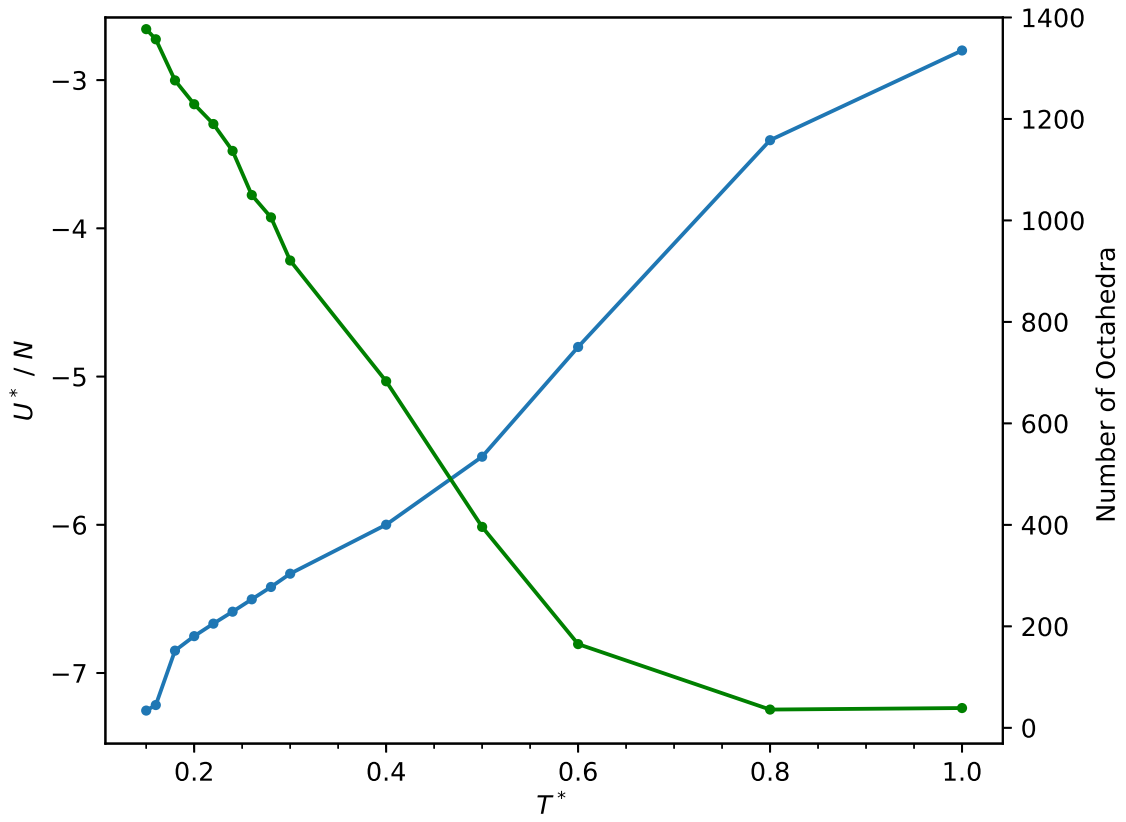

Figure 4.5: Average energy per particle and number of octahedra formed after equilibration along the annealing protocol for $N = 8788$.

We also carried out Brownian dynamics simulations with a system of $N = 8788$ triblock patchy particles at four different volume fractions in order to investigate pathways for crystallisation in detail. The data corresponding to the volume fraction of $\phi = 0.17$ are presented here as in the case for $N = 864$ for comparison. We use the same threshold value for identifying the formation of an octahedral cluster. The average energy per particle and the number of octahedral clusters present in the system are shown in figure 4.5, revealing mostly similar features as observed in 4.3. Note that the low-temperature transition becomes sharper as expected for the bigger system size,

confirming the first-order nature of the phase transition.

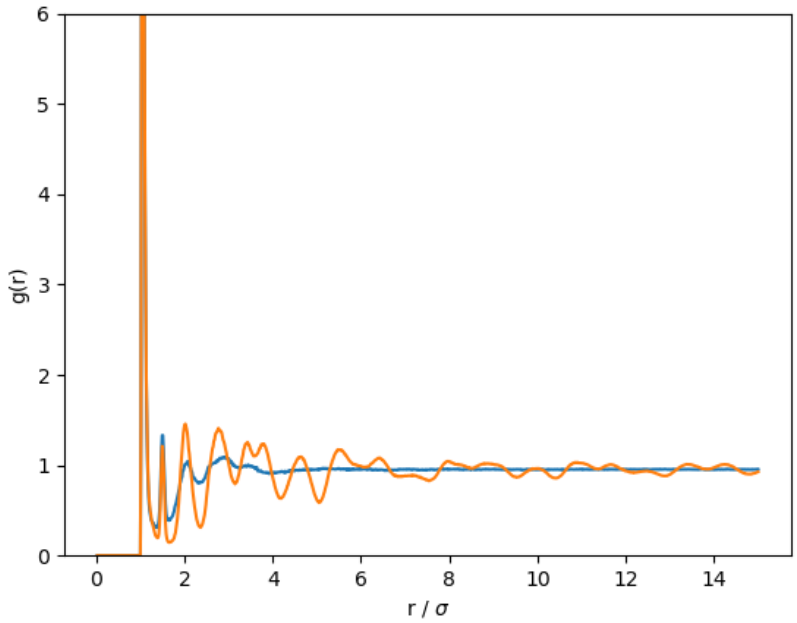

Figure 4.6: Radial distribution functions of elementary particles for $N = 8788$ particles, showing the system before (blue) and after (orange) network formation.

We first use the radial distribution function of the centres of the octahedral clusters, as shown in figure 4.7, to confirm that indeed a simple cubic crystal is self-assembled here. The values for the inter-particle distances for particles on a perfect simple cubic lattice were calculated and scaled based on the distance between two octahedra in the simple cubic crystal structure predicted by `GlOSP` for our designer triblock patchy particles. These are shown as dashed guide lines in figure 4.7. The correspondence between the peaks in the radial distribution function and the dashed lines showing the ideal separations in a perfect crystal provides convincing evidence that the centres of the octahedral clusters formed by the triblock patchy particles in the first stage of assembly sit on a simple cubic lattice in this case. A snapshot of the system at a temperature below the first-order transition is shown in figure 4.8, clearly revealing

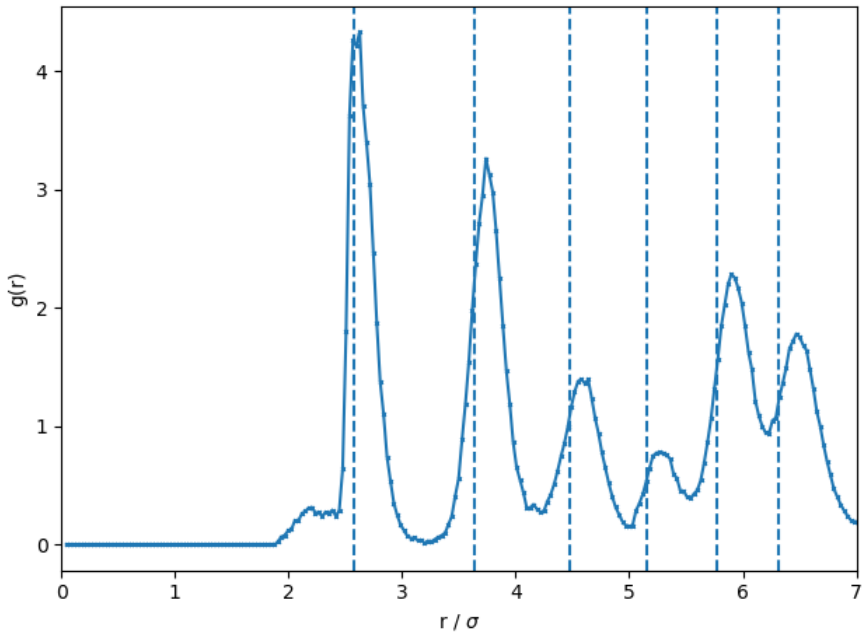

Figure 4.7: Radial distribution function for the centres of octahedra for $N = 8788$. Guidelines for a zero-temperature simple cubic crystal are shown, with the peak positions multiplied by the position of the first peak

the formation of a simple cubic crystal by the designer triblock patchy particles via octahedral clusters.

Using the above criteria we can make the following assignments, shown in table 4.2. This data suggests volume fractions of 0.17 and 0.18 are effective at producing simple cubic crystals, with over 60% of the crystalline octahedra being identified as simple cubic. There is also a clear correlation between average energy and number of simple cubic octahedra, where simulations where the energy is less than -7.10 all have significant crystalline growth. Table 4.2 also highlights the growth of defects at higher packing fractions. At the highest density investigated with 8788 particles, $\phi = 0.19$, we observe a small but not-insignificant growth of BCC crystalline clusters. These clusters are spread throughout the simple cubic crystal but are typically less than 5% of octahedra formed are in such environments. The largest clusters observed in this

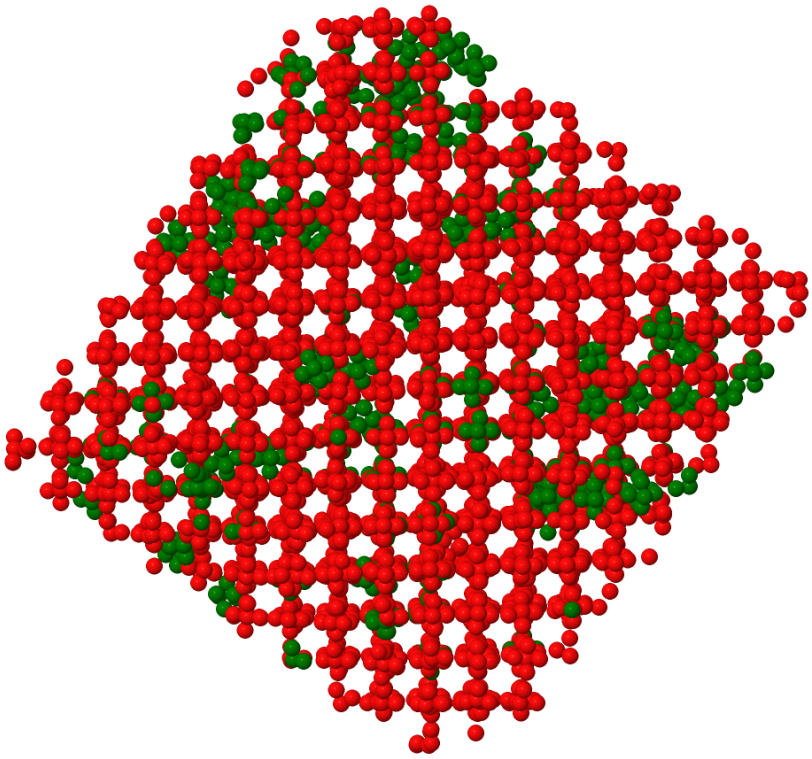

Figure 4.8: A snapshot of a typical configuration obtained for a system of $N = 8788$ designer triblock patchy particles at $\phi = 0.17$ and $T^{\star} = 0.16$. Here, the triblock patchy particles are shown without patches as red spheres if they belong to the largest crystalline cluster, and green spheres if they do not. The method to identify crystalline clusters is detailed in section 4.3.

volume fraction in a BCC environment are in the order of 10s of particles.

4.3 Classification of network

In order to identify the crystal structures self-assembled, we use the Steinhardt bond order parameters [130]. Our protocol for assigning the crystallinity of octahedra is defined as follows:

1. Identify the number of octahedral clusters present in the system

2. Count the number of solid-like octahedra using equation 4.2

3. Calculate the largest cluster of solid-like octahedra

4. Assign the solid-like octahedra in the largest cluster to a crystalline environment using q_l values as detailed in table 4.1

Here we use the complex conjugate of bond orders approach to defining a particle as solid-like. The *coherence* of a particle's local bond-order parameter value to that of its neighbours indicates a solid-like particle [132, 143, 144, 67, 79]. A solid-like particle can then be assigned a crystalline environment *via* traditional q_l approaches. A particle is only considered solid-like if it has $N_{\mathrm{SB}} \geq C_{\mathrm{SB}}$ where N_{SB} is the number of neighbours that meet the similarity condition, and we set C_{SB} to 4. Our protocol follows prescription in line with previous studies investigating pathways to FCC and HCP crystals, setting C_{SB} to $\frac{2}{3}N_{\mathrm{CB}}$, where N_{CB} is the number of bonds a particle has in the perfect crystal [143, 132]. The equation to calculate the components of $\tilde{q}_l(i)$, used for the similarity calculation, is shown below:

$$\tilde{q}_{lm}(i) = \frac{q_{lm}(i)}{\left[\sum_{m=-l}^{l} |q_{lm}(i)|^2\right]^{1/2}} \tag{4.2}$$

The equation to calculate the similarity between two particle's environments is $\tilde{q}_l(i) \cdot \tilde{q}_l^*(j) > 0.7$. The value of 0.7 is slightly higher than what was used in previous studies investigating pathways to FCC and HCP crystals (0.5 and 0.65, respectively) due to the fewer number of bonds present in SC [132, 144]. These works used $l = 6$ for the similarity calculation, but we find that for simple cubic $l = 4$ provides better distinction between liquid- and solid-like environments. Particles that satisfy this criterion and $N_{\mathrm{SB}} > C_{\mathrm{SB}}$, are considered solid-like and their identity is assigned *via* q_l. The values for q_l used for the purpose of assignments are shown in table 4.1. These values are based

on ideal values, calculated by Mickel *et al.* , allowing for deviations due to thermal fluctuations [134].

Crystal (Number of Bonds)	l	q_{lower}	q_{higher}	q_{crystal}
FCC/HCP/Icosahedra (12)	6	0.4	0.7	0.575/0.484/0.663
SC (6)	6	0.6	0.8	0.764

Table 4.1: q_l assignments for solid-like octahedra. q_{crystal} values from [134].

We use an alternative prescription for the assignment of a BCC environment where we utilise $\bar{q}_l$ values. This follows the previous methodology introduced by Lechner *et al* to utilise the second neighbour shell [135]. It has been shown by Morphew *et al* to offer clear assignments for BCC formed from self-assembled octahedra [79]. We use the bounds of $0 < \bar{q}_4 < 0.1$ and $0.4 < \bar{q}_6 < 0.5$ to characterise our octahedra to be in the BCC environment.

ID	N_{O}	N_{SO}	NC_{SO}	N_{SC}	N_{X}	N_{SC}/NC_{SO}	U/N
				$\phi = 0.16$			
1	1339	316	149	45	0	-	-7.05
2	1352	1114	1098	609	0	55.5%	-7.21
3	1339	1133	1128	717	0	63.6%	-7.21
				$\phi = 0.17$			
1	1331	299	292	128	1	43.8%	-7.06
2	1349	125	72	18	0	-	-7.05
3	1357	1190	1183	729	0	61%	-7.22
				$\phi = 0.18$			
1	1367	1043	1037	658	0	63.5%	-7.21
2	1358	1015	938	612	1	65.2%	-7.20
3	1376	1038	1029	644	0	62.6%	-7.19
				$\phi = 0.19$			
1	1373	1112	1110	794	13	71.5%	-7.22
2	1372	960	928	573	1	61.2%	-7.20
3	1368	842	836	512	12	62.3%	-7.19

Table 4.2: Assignments for N = 8788 particles for $\phi = 0.16$ to 0.19 from top to bottom. N_{O} is number of octahedra in system, N_{SO} is number of solid-like octahedra, NC_{SO} largest cluster of solid-like octahedra identified, N_{SC} is number of simple cubic octahedra identified in the largest cluster of solid-like octahedra, N_{X} is the total number of octahedra identified in any FCC, HCP or BCC environments, and U/N is average energy per particle. $N_{\mathrm{SC}}/NC_{\mathrm{SO}}$ percentages only calculated where $N_{\mathrm{SC}} > 100$. Simulation state after 110 million simulation steps at $T^* = 0.16$.

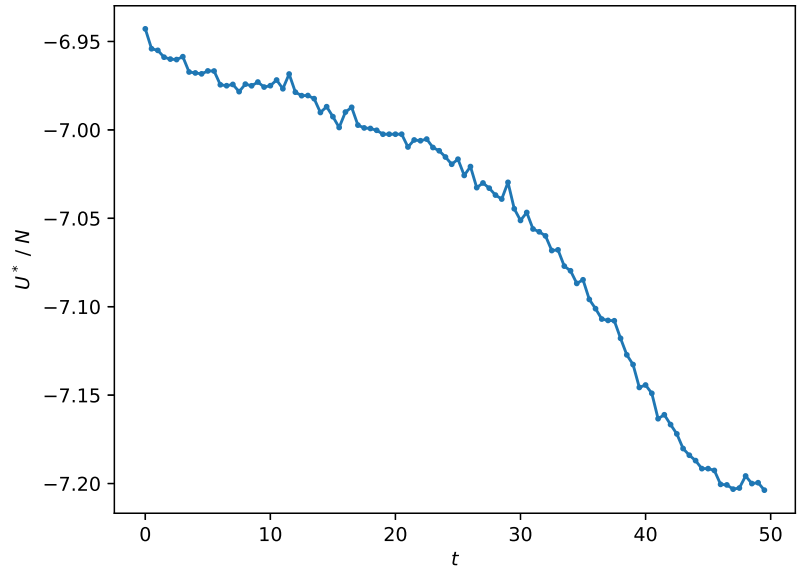

Figure 4.9: Energy per particle over 50 t, $T^* = 0.16$, $\phi = 0.17$ for $N = 8788$.

4.4 Crystallisation pathways

Whilst it is informative to look at the assignment of the crystal structure once the system is equilibrated following crystallisation, we must investigate the state of the system as it evolves over time in order to investigate how crystallisation occurs. We identified a time window of interest at $T^\star = 0.16$ by monitoring the running average of the potential energy per particle along the dynamical trajectory (data not shown). We probe the system over this time window of duration about 50 t, by dividing it into shorter time intervals, each of length 0.5 t. Figure 4.9 shows how the energy per particle, averaged over the shorter time intervals, evolves through this time window.

4.4.1 $N = 8788$

We probe the evolution of the largest crystalline cluster formed by the octahedral colloidal molecules along trajectory 3 through this time window of interest and assign the local environments of the colloidal molecules in these clusters, as summarised in figure 4.10. We observe that the number of octahedral colloidal molecules remains fairly constant, reinforcing the fact that the stronger bonds formed by the wider patches during the first stage of assembly are long-lived and persistent over the timescale of observation. The size of the largest cluster of solid-like octahedra, NC_{SO}, grows almost in unison with the number of solid-like octahedra, N_{SO}, identified in the system, suggesting that nucleation in this case involves the growth of a single nucleus. We also note that the number of octahedral molecules detected in FCC, HCP and BCC environments within the largest crystalline cluster remains low throughout this time window, suggesting that the crystal growth does not proceed through a precursor having any of those morphologies. This contrasts with the current understanding of the formation of an FCC crystal from colloidal isotropic spherical particles, which are said to grow from BCC critical nuclei following Ostwold's step rule [132, 145].

4.4.2 $N = 864$

We also probed in detail how crystallisation occurs in a system of $N = 864$ triblock patchy particles at a higher volume fraction of $\phi = 0.21$. In this case, we also observe a noticable growth in N_{X} due to octahedral molecules being also present in the BCC environment. The trajectory analysis is shown in figure 4.11, where we observe the numbers of octahedral molecules in BCC and simple cubic environments to grow in parallel. Although the growth of BCC environments appears to occur prior to that of simple cubic environment, the signature is not unambiguous; the latter subsequently

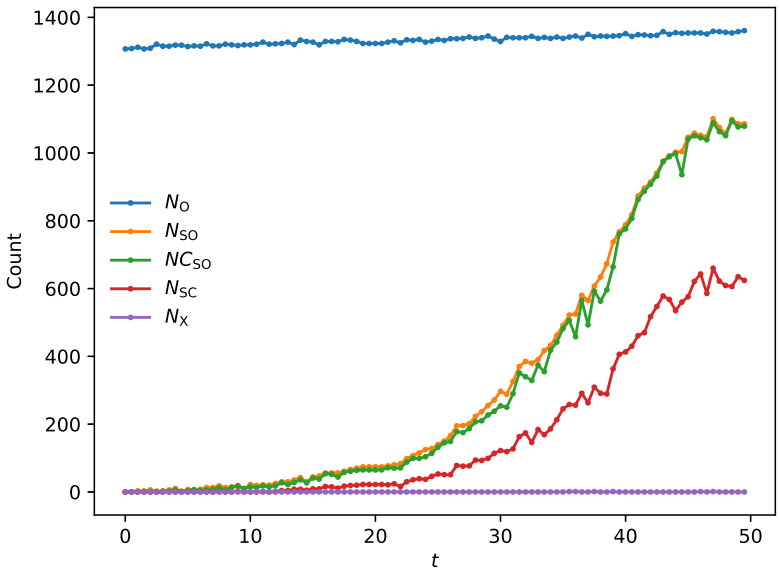

Figure 4.10: Time evolution of the structural composition of the largest cluster formed by the octahedral colloidal molecules along a section of a dynamical trajectory over which crystallisation occurs. Here trajectory 3 corresponding to $\phi = 0.17$ is probed at $T^\star = 0.16$. The labels are the same as in table 4.2.

becomes dominant.

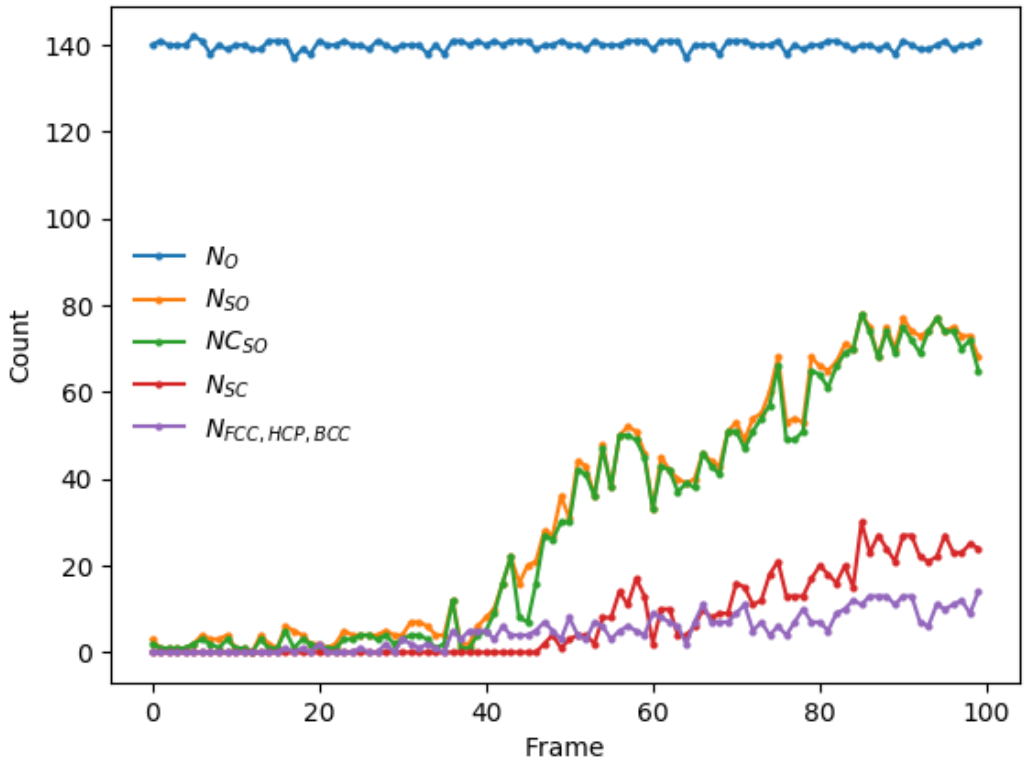

Figure 4.11: Time evolution of the structural composition of the largest cluster formed by the octahedral colloidal molecules along a section of a dynamical trajectory over which crystallisation occurs. Here a trajectory for a system of $N = 864$ triblock patchy particles at $\phi = 0.21$ is probed. The labels are the same as in table 4.2.

4.5 Conclusion

In this chapter, we demonstrate a novel bottom-up route to a simple cubic crystal through hierarchical self-assembly of triblock patchy particles via octahedral clusters. We employ a hierarchy of patch-patch interaction strengths to induce two-stage self-assembly pathways upon cooling. The width of the patches making stronger bonds and the range of interactions over which these patches interact are tuned to ensure the formation of self-limiting octahedral clusters in the first stage of assembly. The weaker patch is chosen to be narrow enough to form only one bond. For such a set of parameters, we show that simple cubic crystals can be exclusively self-assembled over a range of volume fractions in preference to body-centred cubic crystals, which are realised at higher volume fractions. The selective growth of an open crystal over a competing close-packed system provides inspiration for the hunt for self-assembly pathways towards other open crystals, as discussed in the following chapters.

We also investigate the crystallisation pathways along dynamical trajectories obtained from a number of independent simulation runs at different volume fractions. We find that the formation of simple cubic crystals proceeds directly from the fluid phase of octahedral clusters, without the formation of any different crystal structure as a precursor. This crystallisation pathway is in contrast to simulation work by ten Wolde and Frenkel towards the formation of FCC, which is shown to nucleate *via* BCC critical nuclei [131]. We note that in each of the cases presented for $N = 8788$ and $N = 864$, the size of the largest cluster follows closely the number of solid-like octahedra identified in the system, suggesting the presence of a single nucleation site rather than multiple sites.

Chapter 5

Formation of Tetrastack Crystal via Tetrahedral Colloidal Molecules

5.1 Introduction

Photonic crystals have long served as attractive targets for programmed self-assembly of colloidal particles [146, 147, 148]. These crystals are periodically structured optical media generally with a photonic band gap, corresponding to a range of frequencies for photons prohibited to propagate through these media [45]. Colloidal particles are particularly appealing building blocks for bottom-up routes to photonic crystals as their size is comparable to the wavelength of visible light, providing access to photonic band gaps (PGB) in this region. Of the limited number of three-dimensional (3D) crystals known to have a complete photonic band gap, cubic diamond and cubic tetrastack are especially sought-after as they require a relatively low refractive index contrast for the band gap to emerge [49, 50, 148]. These 3D crystals have rather open structures, making them elusive for being realised through bottom-up routes [58, 59, 60]. One of the challenges arises from the task of making these low-coordinated crystals mechanically

stable for designer colloidal building blocks. In particular, the tetrastack lattice with a mean coordination of 6 is on the verge of mechanical instability as per Maxwell's argument [64, 52].

For a bottom-up route to be a viable means of fabrication of a desired colloidal open crystal, the target structure is required to be not only thermodynamically favoured for the building blocks of choice, but also kinetically accessible via self-assembly pathways in preference to metastable structures [80, 149, 78]. In the context of self-assembly of tetrahedral patchy particles into a diamond crystal, kinetic traps are known to arise from the competition from an amorphous phase with random tetrahedral network structures [150]. The presence of competing cubic and hexagonal polymorphs yet again increases the challenge of forming these colloidal crystals via self-assembly pathways for photonic applications [67, 151, 152]. This issue of polymorph selection in the case of tetrastack lattices will be investigated in detail in the next chapter.

Here we devise a new bottom-up route to tetrastack lattices, relying upon hierarchical self-assembly pathways for designer triblock patchy particles and explore whether such pathways promote crystallization. A tetrastack lattice is comprised of vertex-shared tetrahedra [50, 147] and can thus be conceived to be realized by a two-stage self-assembly of triblock patchy particles via tetrahedral clusters. The key to the success of such a staged assembly scheme is the self-limiting formation of tetrahedral clusters in the first stage.

5.2 Results

5.2.1 Crystal structure prediction

We initially employed the basin-hopping algorithm for global optimisation on crystal energy landscapes to predict the crystal structures for the triblock patchy particles considered here in search of the parameter space that could possibly support tetrastack crystals. In the present study, we restrict ourselves to the triblock patchy particles that have two equal-size patches on the poles. The size of the patches is chosen to ensure that each patch can make contacts with three other patches in order to form a tetrahedron, as shown in Figure 5.1a. We consider such triblock patchy particles of two types: one type has two identical A patches, interacting with a strength $\varepsilon_{\mathrm{AA}} = 1$ so that the triblock patchy particles retain the head-tail symmetry in addition to the cylindrical symmetry. The second type involves two different patches, A and B, having different strengths for the interactions between patches such that $\varepsilon_{\mathrm{BB}} = 0.2\varepsilon_{\mathrm{AA}} = 1$. For simplicity we fix $\varepsilon_{\mathrm{AB}} = \sqrt{\varepsilon_{\mathrm{AA}}\varepsilon_{\mathrm{BB}}}$. We call the former AA-triblock patchy particles and the latter AB-triblock patchy particles, the latter lacking the head-tail symmetry despite having the patches of the same size. [1]

Figure 5.1b shows characteristic 16-particle motifs of the two polymorphs that we identify as the global minima on the crystal energy landscape for our designer AB-triblock patchy particles for a range of parameters. These polymorphs have identical lattice energies. The global minima of the AA-triblock patchy particles are near-identical to those found for the AB ones, with only subtle differences to bond lengths. It is noteworthy that the lattices formed by the AB-triblock patchy particles have two distinct sets of tetrahedra, one strongly bound and the other relatively weakly

[1] Thanks to Abhishek Rao and Andreas Neophytou for crystal structure prediction input and discussion.

bound, of slightly different volumes. The two polymorphs, both comprised of vertex-shared tetrahedra, differ in the relative arrangements of the tetrahedra as apparent in Figure 5.1b. In the cubic polymorph, all four strongly bound tetrahedra are staggered relative to the weakly bound tetrahedron formed by the interactions between B patches. In contrast only three of the four strongly bound tetrahedra are staggered relative to the weakly bound tetrahedron in the hexagonal polymorph, the fourth one being in an eclipsed arrangement.

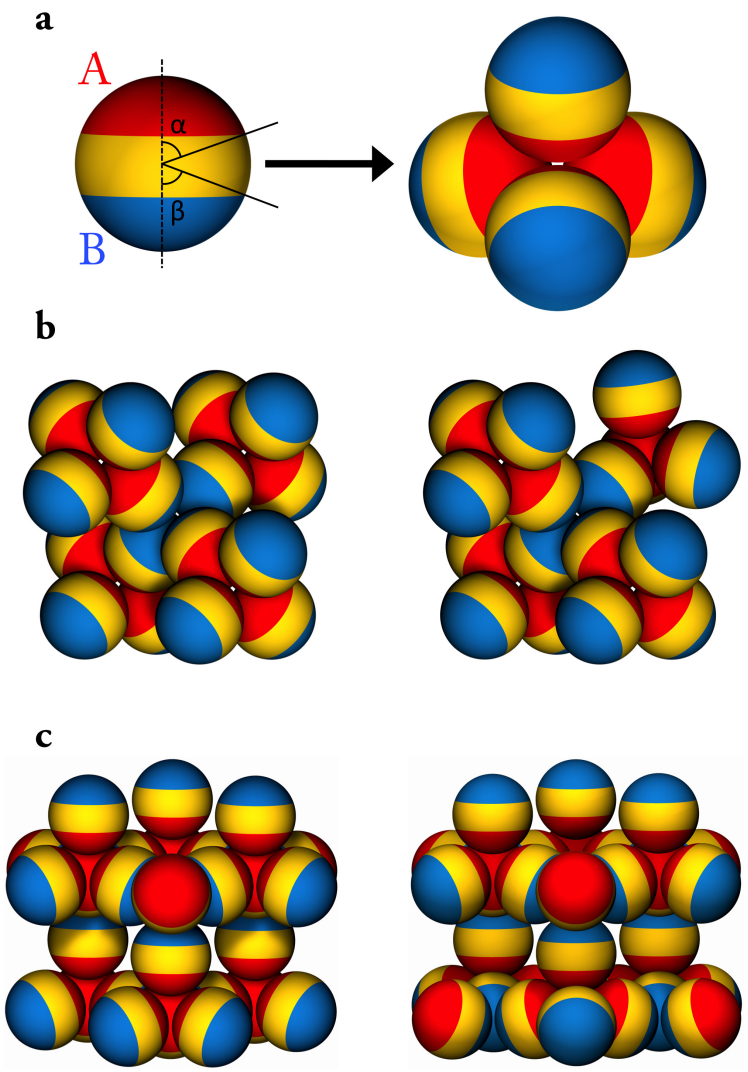

Figure 5.1: Tetrastack crystal structures formed by triblock patchy particles via tetrahedra in the presence of a hierarchy of interactions. (a) Designer triblock patchy particles with equal-size patches on the poles. Patch A, colored red, formed stronger contacts relative to those formed by patch B, colored blue. (b) Characteristic 16-particle motifs of the cubic (left) and hexagonal (right) tetrastack structures. In the cubic tetrastack structure, each of the four strongly bound tetrahedra formed by A patches are staggered relative to the weakly bound tetrahedron formed by B patches. In the hexagonal polymorph, one of the four strongly bound tetrahedra is in an eclipsed arrangement relative to the weakly bound tetrahedron, while the remaining three are staggered. (c) Portrayal of the the cubic and hexagonal tetrastack structures formed by the triblock patchy particles under consideration, highlighting that both of these polymorphs consist of alternating layers of two-dimensional kagome and triangular planes.

5.2.2 Brownian dynamics Simulations

For these two systems, AA and AB, which only differ in the presence of patch strength hierarchy, we carried out Brownian Dynamics simulations to investigate whether two-stage self-assembly pathways can yield the tetrastack crystal structures that we identified to be stable on the crystal energy landscapes. To this end, we considered a system of $N = 864$ triblock patchy particles in a cubic box at a volume fraction of $\phi = 0.3$ under periodic boundary conditions, implementing the minimum image convention. The system was initially melted at temperature $T^\star = 1$ from an FCC lattice at the chosen volume fraction and equilibrated. Four configurations well separated along the dynamical trajectory were then subjected to gradual cooling, allowing the system to equilibrate at each step. The timescales and temperature protocols followed are shown in table 2.1. Additional simulations for a larger system size of $N = 4000$ are discussed in the following chapter.

5.2.3 Following Crystallisation

To investigate the initial stage of the simulation we count the number of tetrahedra identified in the system. We use the same equation for identifying tetrahedra as we used for counting octahedra, shown in 5.1. To count tetrahedra only three neighbours are used, using a value of $q_{\text{tet}} > 0.99$ as our threshold [136].

$$q_{\text{tet}} = 1 - \frac{3}{8} \sum_{j=1}^{N_b-1} \sum_{k=j+1}^{N_b} (\cos \psi_{jk} + \frac{1}{3})^2 \tag{5.1}$$

At a temperature at which a patch-patch bond becomes thermodynamically stable we observe a rise in the number of tetrahedra, indicating a phase transition. Figure 5.2 shows the number of tetrahedra and potential energy per particle against temperature

for a single trajectory. Here we can clearly see the correlation between the number of tetrahedra and potential energy of the system, with the almost symmetrical figure showing that the stability shown from the potential energy drop is caused by tetrahedra formation. We observe the multiple stages of the simulation signalled by drops in energy, with the first occurring between T^* =0.6 and 0.2 where the strong tetrahedra are formed. The second stage is a significantly larger drop between $T^* = 0.16$ and 0.14, where the weaker patches are activated and a percolating network is formed between tetrahedra. We show the potential energy against time for three trajectories in figure 5.3, showing that multiple independent trajectories follow this two-stage pathway to a percolating structure.

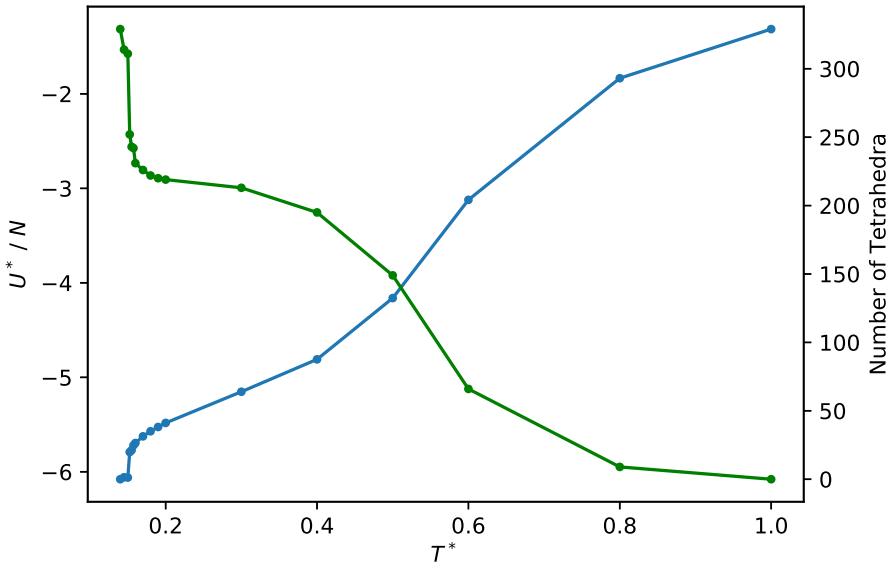

Figure 5.2: Plot showing the number of tetrahedra and potential energy of the system per particle, for one trajectory against temperature. Blue shows the average energy per particle and green shows the percentage of tetrahedra formed. This system utilises the hierarchy of interaction strengths to achieve staged self-assembly.

Shown in figure 5.4 is the number of tetrahedra and average energy of the system for the non-hierarchy run, where $\epsilon_A = \epsilon_B = 1\epsilon_Y$. Here we can see that in contrast to figure

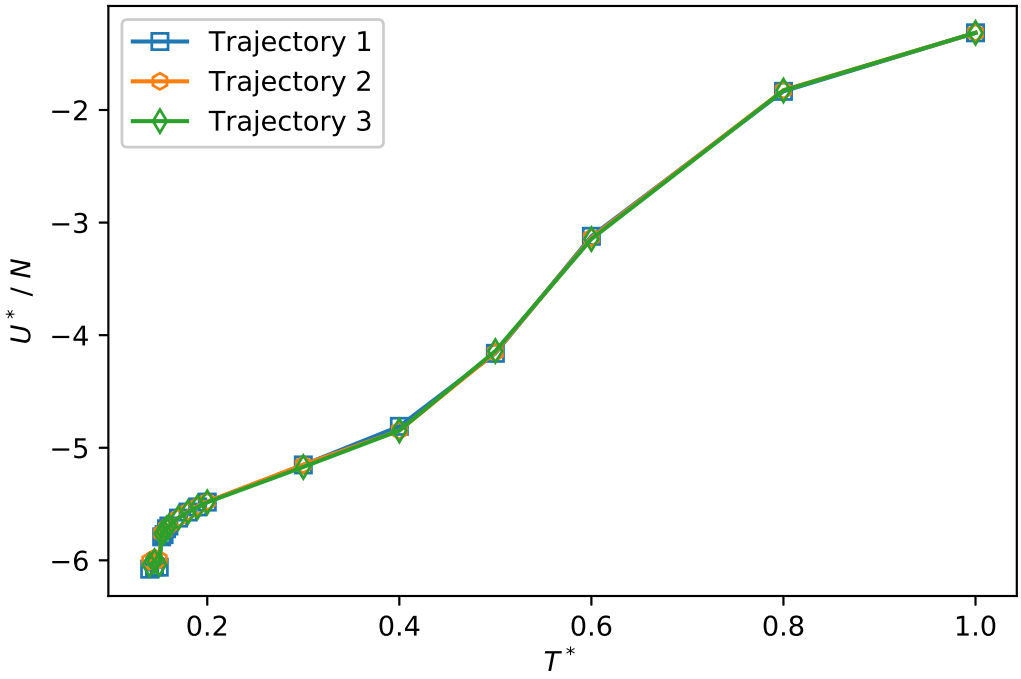

Figure 5.3: Average potential energy per particle against temperature for 3 trajectories for $N = 864$ AB particles. All three trajectories exhibit multistage assembly.

5.2 there is only a single phase transition, beginning around $T^* = 0.16$ and continuing to $T^* = 0.1$. We observe the number of tetrahedra increase rapidly, but rather than reaching a plateau of around 210 tetrahedra, the system continues to develop more tetrahedra, beginning to tail off around 300. This is in contrast to that observed in the AB hierarchy pathway, where only three of the 6 bonds per triblock particle are satisfied and each particle is an element in a *single* tetrahedra. From visual inspection we can see that the system has not formed a crystal and the tetrahedra remain in a dissordered state.

To further probe the state of the networked system we analyse the radial distribution plots. Sharp peaks which extend the length of the simulation box would indicate a repeating structure, while broad peaks suggest inhomogeneity. We show the radial

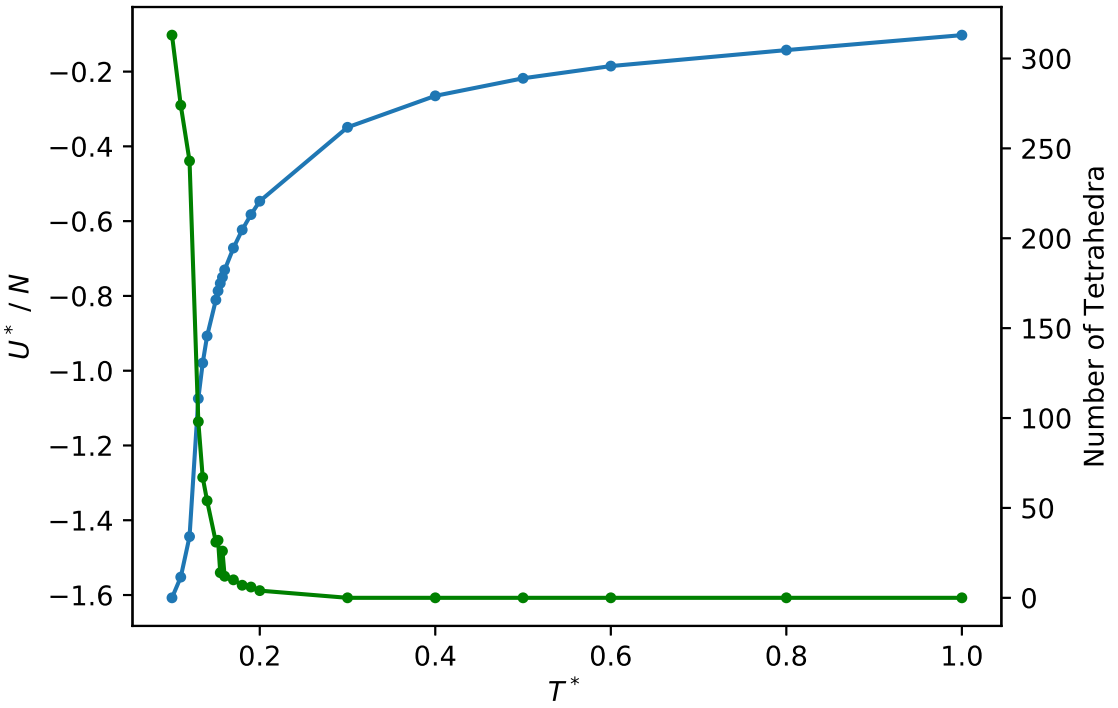

Figure 5.4: Plot showing the number of tetrahedra and potential energy of the system per particle, for one trajectory against temperature. Blue shows the average energy per particle and green shows the percentage of tetrahedra formed. This system does not use the hierarchy of interaction strengths and follows a different pathway to a percolating, non-crystalline structure.

distribution function for the two configurations used in the cycle analysis in figure 5.5, where we can see that the AA system has short-range but not long-range order. We contrast this with the AB plot, shown in blue, which exhibits pronounced peaks that extend to the end of the simulation box. To investigate the differences between the two networked states, we perform graph analysis to investigate cycle counts.

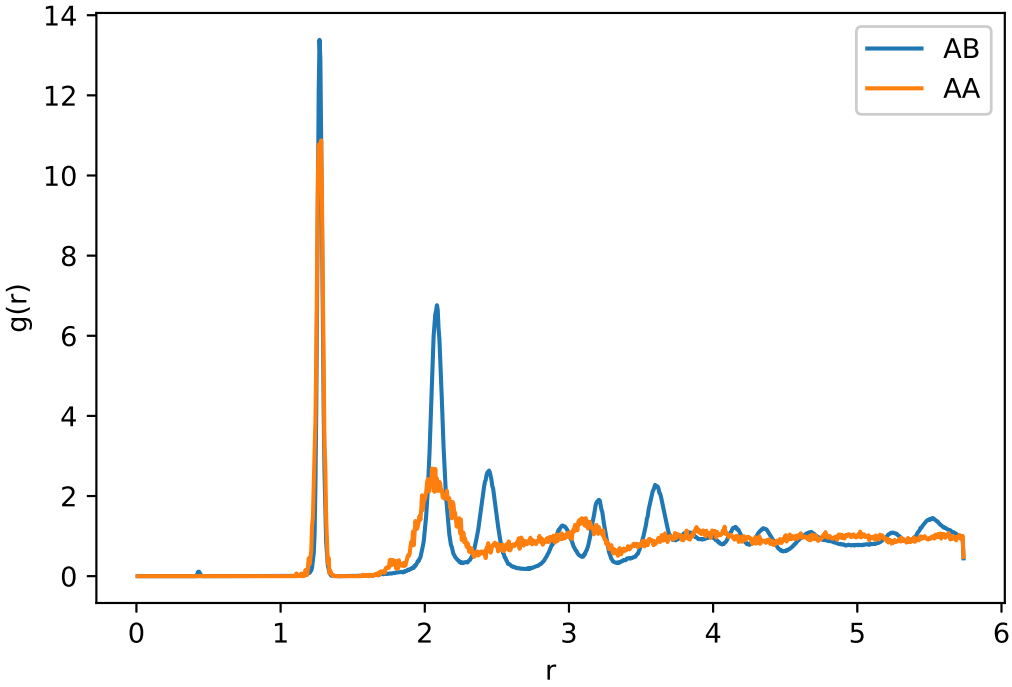

Figure 5.5: Radial distribution plot for AA and AB triblock patchy particle systems at at $T^* = 0.14$ and $T^* = 0.1$ for AB and AA systems respectively. We observe the long range order for the hierarchy system, but not for the alternative except for the formation of tetrahedra, present in both systems as dictated by the patch sizes.

5.2.4 Cycle analysis

The formation of cycles is crucial in the pathway to crystallisation. We use patch hierarchy to control the sizes of cycles formed, which influences the accessibility of competing polymorphs. To test this hypothesis we use graph analysis to follow the number of cycles formed, and their properties, throughout the simulation.

Method

We calculate the distribution of rings, with lengths $R_l \in [4-8]$, in a system of N particles using a graph-theoretical approach [153]. We describe our patchy particle system as a periodic undirected graph, where each vertex represents a particle center and the edges represent a bond between two particles. To calculate the number of cycles, we import our crystal as a graph, defining particles as nodes and drawing edges between particles if they meet a cutoff distance, which we set to σ 1.4. For each particle, we create a subgraph by performing a depth-first-search of fixed depth $\Delta = 4$, importing edges between nodes in this subgraph. The depth of 4 allows us to probe cycles with lengths up to 9 ($\Delta \times 2 + 1$). For each node in the subgraph we calculate all 'simple' paths between nodes, where a simple path is a path with no repeated nodes. When there is more than one simple path between nodes i and j we say that a cycle is formed between them. Once we have looped over all particles and have a list of all cycles identified in the network, we loop through every cycle to remove cycles that contain other cycles. This is the same definition of a cycle as a closed path in this graph (i.e., a path whose first and final vertex are the same). We then define a ring as a cycle that forms part of the minimum cycle basis in our periodic graph. For each vertex in the graph we calculate all distinct paths with R_l edges using a depth-first search traversal, up to the chosen maximum R_l, making sure to prune paths with edges

between non-adjacent vertices and those whose first and last vertex are not the same. This provides us with a count of rings with lengths R_l, each vertex is a part of. [2]

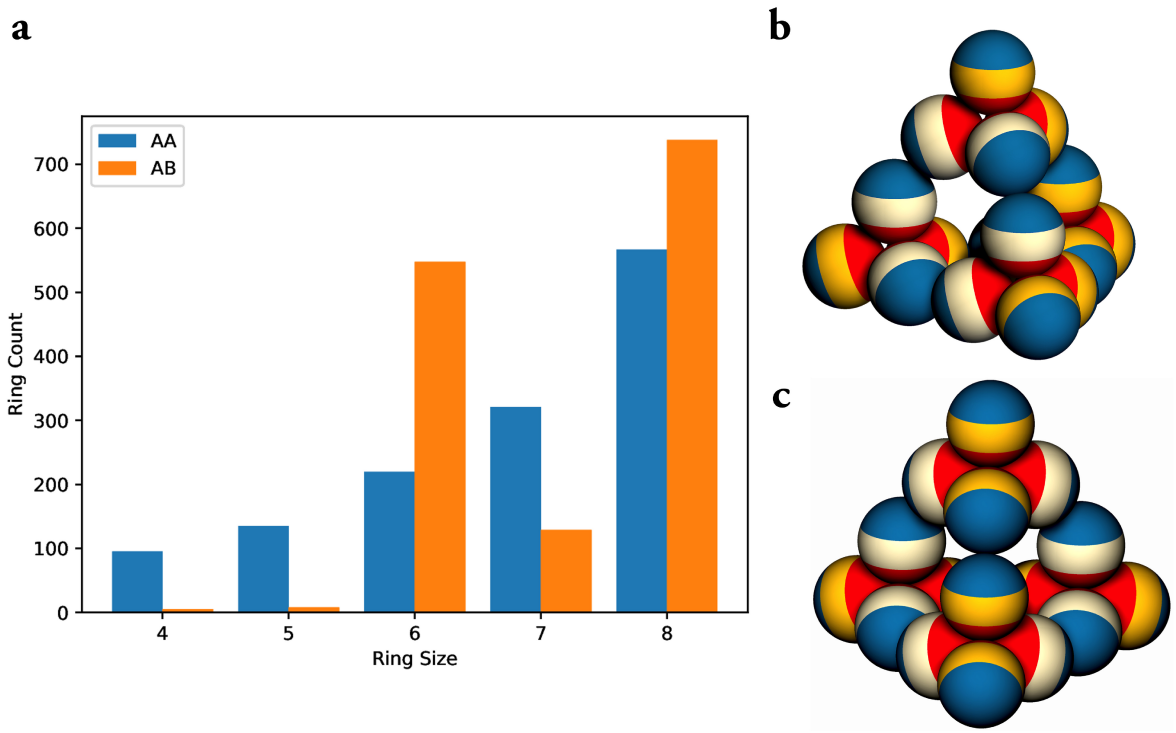

Figure 5.6: Results of cycle calculation following the growth of rings of set sizes. a) A comparison between the number of rings and their sizes for AA- and AB-triblock systems. The AA system is at $T^* = 0.1$, while the AB system is at $T^* = 0.15$ for $N = 864$. b,c) A visual representation of the 6- and 8-membered rings present in the tetrastack crystal, with highlighted middle bands in a lighter shade for particles that form the 6 (b) and 8 (c) rings.

Results

Shown in 5.6 b and c are representations of the 6 and 8 membered rings that are found in the tetrastack crystal. The formation of 6 membered cycles is critical to the growth of the crystal, as any 5 or 7 membered cycles would introduce defects that would distort the crystal. Crucially, this figure shows that in the system without hierarchy, despite

[2]Thanks to Francesco Sciortino and Andreas Neophytou for providing the cycle identification code.

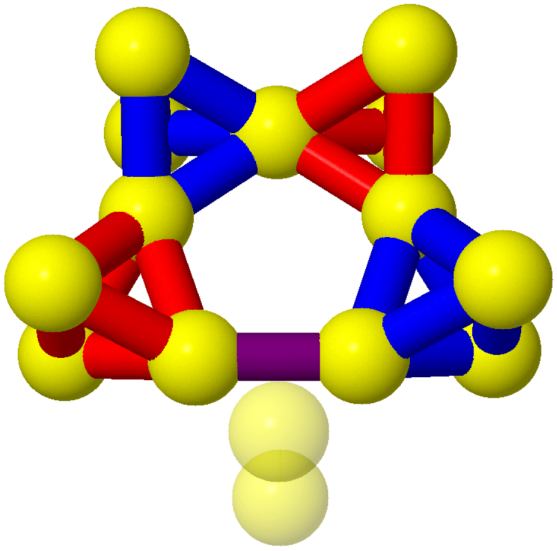

Figure 5.7: A 5 membered cycle of tetrahedra. Strong bonds are drawn as red lines between particle centres, with weak bonds drawn in blue. A hierarchy of patch strengths requires an AB bond (shown in purple) for a 5 membered cycle, which is energetically disfavoured as the system is held at a high temperature to saturate the AA patch interactions first. The particles shown as translucent would be part of this strong-weak tetrahedra hybrid, and their bonds are not shown for clarity.

the relatively similar number of tetrahedra that are forming as shown in figure 5.4, these tetrahedra are not sitting on the tetrastack lattice. We observe that the hierarchy of patch strengths prevents the growth of these disfavoured cycles. In the hierarchical assembly, the formation of rings will only begin once the second stage is triggered by transitioning to a lower temperature, at which point the system is comprised entirely of tetrahedra. As these tetrahedra interact with one another to form cycles, the cycle size is restricted to even-numbered cycles, as an odd-numbered cycle length would require a free particle to bridge a strong-weak interaction. This is shown in figure 5.7, where the purple bond would be a hybrid of strong and weak patches interacting. Such a bond is weaker than a strong-strong bond and by saturating all the strong bonds in the first stage of assembly we prohibit this bond from forming.

In figure 5.8, we show how the number of rings evolves as the trajectories are

equilibrated at $T^* = 0.15$, the transition temperature. The growth of the 6- and 8-membered rings for trajectory 1 appears to come at the cost of 4- and 5-membered rings, where the period of rapid growth for the former occurs at a similar time to the decline of the latter. This is also the case for trajectory 3, which also sees a decrease of aproximately 33% of the 7-membered rings. We note that for clarity cycles of 3-membered rings are not shown. Trajectory 2 shows a much more gradual increase in 6- and 8-membered rings. We investigate the differences between these two trajectories in the following chapter.

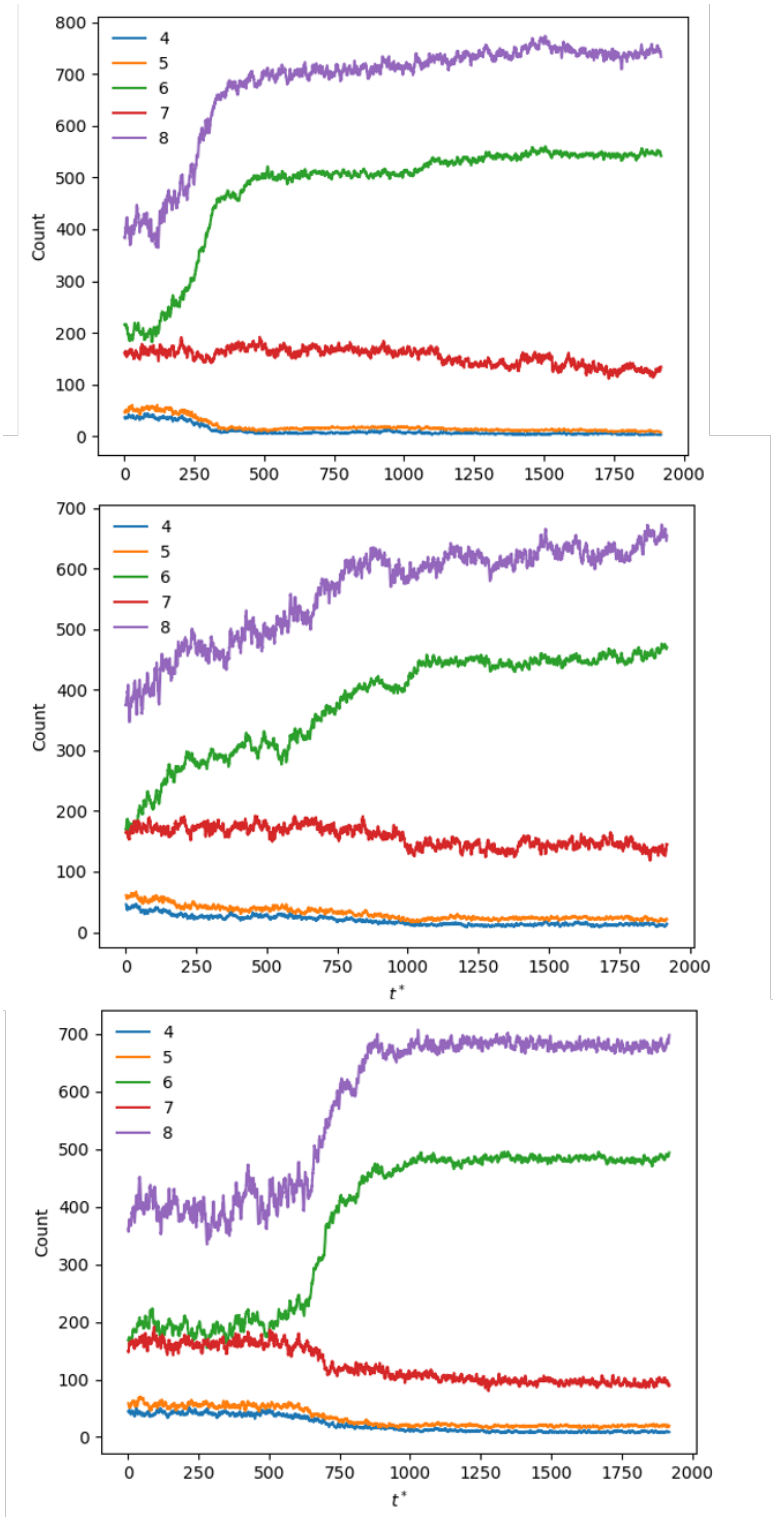

Figure 5.8: Evolution of ring statistics for three trajectories at N = 864, $\phi = 0.3$. In all cases the number of 6- and 8-membered rings increase with time at the expense of rings of other sizes, but the rate of growth in trajectory 2 shows a much slower growth.

5.3 Conclusion

We here employ a hierarchical self-assembly scheme encoded in triblock patchy particles to establish a novel bottom-up route to tetrastack crystals, which are comprised of vertex-shared tetrahedra. The hierarchical self-assembly pathways proceed in two stages, forming self-limiting tetrahedra upon completion of the first stage *en route* to tetrastack crystals. In this assembly scheme, we exploit a hierarchy of patch-patch interactions to induce the staged assembly upon cooling, while the formation of self-limiting clusters in the first stage is achieved by the choice of patch size and the range of patch-patch interactions.

Critically, in comparison to previous chapters, the two patch angles are identical as $\alpha = \beta$ so that the elementary particles have appropriate symmetry for the target tetrastack crystal. We investigate the importance of patch strength hierarchy and find it to be critical, despite crystal structure predictions indicating that on the potential energy landscape there is minimal difference.

In the context of the self-assembly of triblock patchy particles with a large patch size considered here, we find that the tetrastack crystal structures are in competition with disordered network structures. Our results demonstrate that the hierarchical self-assembly pathways followed by our designer triblock patchy particles promote the formation of six- and eight-member rings present in the perfect crystal structures as opposed to five- and seven-member rings, and thus help negotiate the kinetic traps to yield the target crystals. Without the patch strength hierarchy these five- and seven-member rings form, leading to dissordered network competition and preventing long-range crystallisation.

Chapter 6

Crystallisation Pathways and Polymorphism in Tetrastack

6.1 Introduction

Polymorph selection is of much importance for many practical applications, from pharmaceutical products to photonics [154, 67]. Many active ingredients of pharmaceutical products have multiple polymorphs with differing bioavailability, influencing the effectiveness of the drug [154]. Even water, consisting of only two elements, can crystallise into a considerable number of ice polymorphs depending on the conditions [155].

The applications of colloidal open crystals realisable via self-assembly pathways are often impaired by the fact that the free energy differences between the target crystal structure with exciting physical and optical properties and polymorphs that lack these properties, are very small [60, 66]. For example, the difference in free energy between the cubic and hexagonal polymorphs for the diamond crystal is reported to be as small as $0.02 k_{\mathrm{B}} T$ by Romano *et al.* [60] when investigating the crystallization of tetrahedral patchy particles, meaning that without introducing some sort of additional driving

force, either through the addition of glue particles [68], or adapting the anisotropy of the interactions, making a polymorph selectively grow in a system is challenging.

In particular, the selective self-assembly of cubic tetrastack crystal is believed to be of immense importance for photonic applications, as only the cubic polymorph has so far been known to host a complete photonic band gap [67, 151]. As noted in the introductory chapter, the patterning symmetry concept prescribed the use of staggered triangular patches rather than the conventional circular patches on the poles of triblock patchy particles to exclusively yield the cubic tetrastack [67]. A hexagonal tetrastack structure was instead selectively self-assembled in a more recent computational study by introducing large star polymers, commensurate with the void symmetry [151]. The star polymers in this case acted as structure-directing agents to promote an entropic bias towards the formation of the hexagonal tetrastack lattice, where octahedral and tetrahedral voids have different arrangements as compared to the cubic polymorph. However, these design principles have proved difficult to put in practice because of the synthetic challenges involved, where the use of a structure-directing agent, if not optimal, could destabilise the open crystals relative to their closed-packed counterparts.

Crystallisation pathways are known to impact polymorph selection [156]. Understanding crystallisation pathways in detail helps us control nucleation and growth of a crystal and at times can offer a route to polymorph selection. In this chapter, we investigate whether the two-stage self-assembly pathways that we have devised in the previous chapter to yield the tetrastack crystal leads to the selection of the cubic or hexagonal polymorph or promotes any bias towards one of these polymorphs.

6.2 Cubic and Hexagonal Tetrastack

Two polymorphs of the tetrastack crystal can be formed through the self-assembly protocol provided in chapter 5 - cubic and hexagonal. By considering the tetrastack structure as a layering of kagome and triangular planes, we can distinguish the polymorphs as shown in figure 6.1a, where in cubic tetrastack, the kagome layers pack in an alternating ABCABC fashion and in the hexagonal structure pack with ABAB order.

Alternatively, we can distinguish the polymorphs by considering the orientation of bonds between strong and weak tetrahedron. Each elementary particle in the tetrastack crystal will form six bonds - three strong-strong (red-red) and three weak-weak (blue-blue). For the hierarchy of bond strengths approach shown in chapter 5, the strong patches will form first, followed by the weaker patches, forming two parallel planes of elementary particles around the central triblock colloid. This structure of 7 particles can be compared to the molecular structure of ethane, where our particles sit in between every bond. When considering these 7 particles we can describe the system as eclipsed or staggered with respect to the dihedral angle between two particles in the different planes and the centres of tetrahedra. Should the system be eclipsed, these dihedral angles will be 0°, 120° and 240°, and in a staggered environment 60°, 180° and 300°. In organic chemistry this is typically visualised through Newman projections or Ramachandran plots.

For a tetrahedra formed from weak-weak interactions this central tetrahedra will be interacting with four other tetrahedra, where the number of tetrahedra in staggered and eclipsed conformations can differentiate cubic and hexagonal tetrastack. In cubic tetrastack, every tetrahedra is staggered with respect to the central weak tetrahedra, while in hexagonal one of the four tetrahedra is in an eclipsed conformation.This is shown in the top half of figure 6.1a. In 6.1b we show the relationship between the

polymorphs of tetrastack, diamond and close-packed crystals. Here we can see how the centres of tetrahedra lie on cubic diamond lattice points, and that if we consider only the strong tetrahedral centres, those formed from strong-strong patch interactions, that these centres lie on FCC and HCP lattice points for cubic and hexagonal tetrastack respectively. As the crystalisation pathways for these close packed systems has been well studied, an interesting line of enquiry is along the influence of these colloidal tetrahedral molecules on the pathways taken.

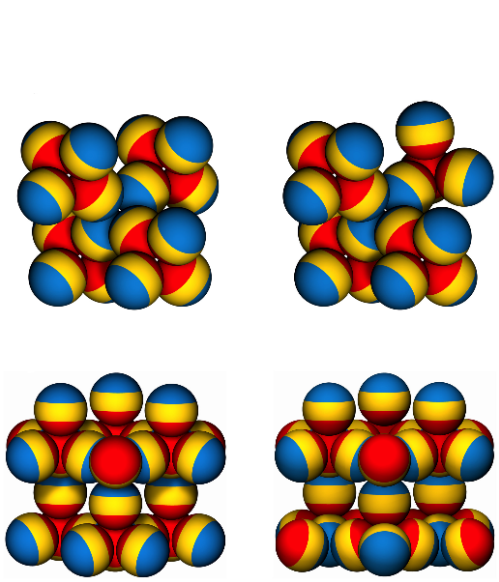

(a)

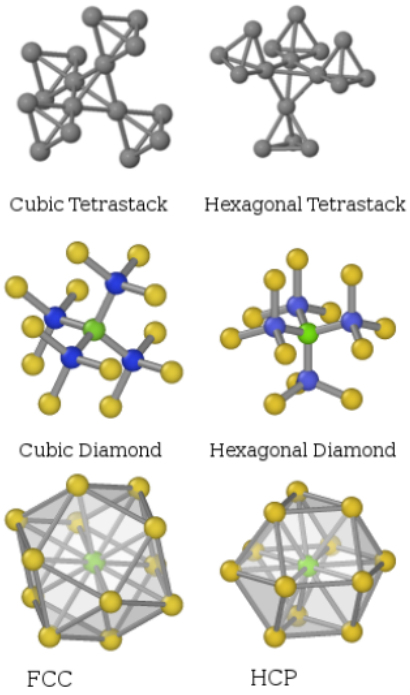

(b)

Figure 6.1: Polymorphs of tetrastack: a) left column, cubic, right column, hexagonal. The top row shows the staggered and eclipsed elementary particles with their patches shown, with the top-right tetrahedra different between the two. The bottom row shows the layering of triagonal and kagome lattices. b) The relationships between tetrastack, diamond and close-packed crystals. In the top row the centres of mass of the elementary particles are shown for tetrastack, with lines drawn to show 'bonds'. In the middle row the centres of the tetrahedra are shown, as they lay on a cubic diamond lattice. In the bottom row we show how the centres of tetrahedra formed through strong-strong (AA) bonds sit on close-packed lattices. Subfigure b adapted from Ovito manual [157].

6.3 Following Nucleation and Growth

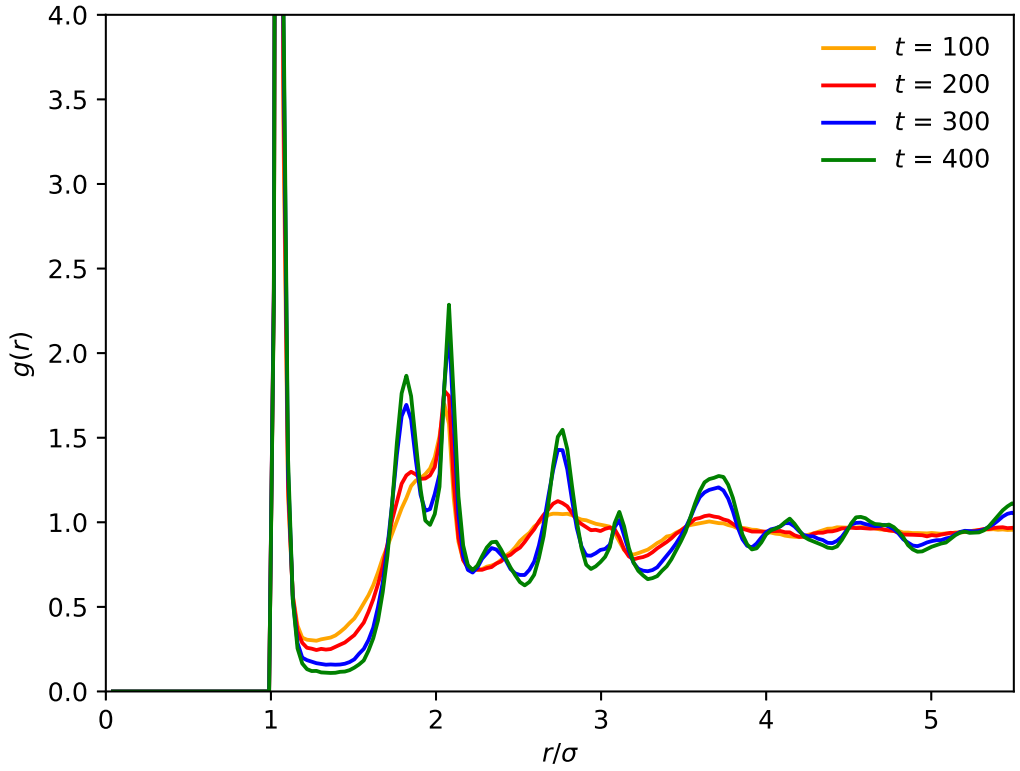

Figure 6.2: Radial distribution functions for triblock patchy particles along trajectory 1 as time evolves. From $t = 200$ we see a development of long range order.

We first identify the sections of the trajectories of interest by probing the radial distribution functions and potential energy throughout the transition temperature, $T^* = 0.15$. In figure 6.2, we show how the radial distribution function evolves along the trajectory, showing the development of long range order between $t = 200$ and 300. We can confirm the transition occurs through this time period by consulting the potential energy plot over time, as shown in the blue plot in figure 6.3, showing a clear transition in the first 500 t.

Also shown in figure 6.3 are two other configurations run at the same system con-

figuration. The blue and green plots, trajectories 1 and 3 respectively, follow a similar path with a sharp decrease in potential energy, while the orange plot begins with a steep decent and then follows a much gentler gradient towards the lower potential energy. These different profiles suggest alternative pathways are being followed. We also note that the rate of the potential energy drop is significantly slower for this crystal formation than in the simple cubic and body-centered cubic pathways discussed in chapters 4 and 3, where the nucleation for a similar number of particles completed in roughly 100 t.

6.4 Assigning Tetrastack Polymorphs

We devised an assignment scheme based on the local environments of the particles in the structure self-assembled from our designer triblock patchy particles. The scheme first identifies whether a particle is in a crystalline environment based on its number of neighbours and then assigns each crystalline particle to be staggered or eclipsed using the calculated values of the Steinhardt bond-orientational parameters q_4 and q_6. If the calculated values do not satisfy certain conditions appropriate for a particle to be labelled as staggered (Condition I: $0.32 < q_4 < 0.43$ and $0.65 < q_6 < 0.83$) or eclipsed (Condition II: $0.13 < q_4 < 0.23$ and $0.35 < q_6 < 0.47$), the particle is left unlabelled. The eclipsed particles are assigned to be in hexagonal environment, while the staggered particles are further classified into cubic, hexagonal or interfacial environment based on its number of eclipsed neighbors. The scheme is presented in detail with the help of a decision tree shown in Figure 6.4.

The range of values we used for the bond-orientational order parameters, q_4 and q_6, to label the particles as being in a staggered or eclipsed environment are effectively centered on the corresponding values in the perfect crystal structures. In the perfect

cubic tetrastack crystal, we identified all the staggered particles to have the following bond-orientational order parameter values: $q_4 = 0.375$ and $q_6 = 0.741$.

However, only three quarters of the particles in a perfect hexagonal tetrastack crystal are in a staggered environment (with the same set of values for q_4 and q_6), the remaining being in an eclipsed environment. For these eclipsed particles forming the triangular layers along the [001] axis, the bond-orientational order parameter values were found to be $q_4 = 0.181$ and $q_6 = 0.411$.

6.4.1 Bond Order Assignments

We investigate the difference between these two separate pathways by looking at the growth of hexagonal, cubic and interfacial elementary particles. This analysis is presented in figure 6.5, where we observe a clear connection with the timeline of growth of crystalline elemental particles and the potential energy shown in figure 6.3.

For all three trajectories at $t = 0$ the system begins with a greater number of particles at the interface between cubic and hexagonal than either polymorph. For trajectories 1 and 3 we observe the sharp increase in number of interfacial and cubic particles over a period of 250 t, with a much more reserved growth for the hexagonal environment. However, for trajectory 2 there is no large increase in a similar timeframe, with the growth between 600 - 1000 t the largest region of increased crystallinity. We note that for trajectory 1, post 1000 t we see the drop in cubic environment and growth of interfacial and hexagonal identifications. These changes in local environment suggest the potential for for conversion between the two polymorphs post-nucleation. As we shall see in the next subsection, these conversions take place without the size of the network increasing, suggesting that these environment changes are not due to the addition of surface particles joining the crystal with that environment. We see

a similar, but much more subtle, effect in trajectory 3, where post nucleation the number of hexagonal is slowly rising while cubic is declining. In all three trajectories, the cubic polymorph is the first crystal to grow to a cluster of significant size. This idea of conversion between crystalline environments could be seen as a manifestation of Ostwald's step rule, where the system does not nucleate to the bulk crystalline state but through steps in structures with small free energy differences [25]. We emphasise that this hypothesis remains to be tested through rigorous free energy calculations.

6.4.2 Largest Cluster

In figure 6.6 we show the size of the three largest clusters of elementary particles identified in any crystalline (cubic, hexagonal or interfacial) environment for each trajectory. These clusters are generated through a depth first search network analysis, where the particles are nodes in the graph and links exist between nodes if the elementary particles are less than 1.2 σ apart. This range is justified for the drop in intensity after the first peak in the radial distribution functions shown in figure 6.2.

For trajectory 1 we see the rapid growth of the largest cluster (blue), which eclipses in size the second (orange) and third (green) largest clusters over $t = 100$ and dominates the rest of the system, with the crystal growing from this initial nucleation point. We note that the system appears to go though a period of arrest between 500 - 900 t, identified through the size of the largest cluster remaining fairly constant and the lack of change of crystalline environments shown in figure 6.5.

For trajectory 2 we observe a remarkably different plot. From $t = 750$ we observe the rapid growth of a cluster as shown by the increase in largest cluster to contain approximately 15% of all elementary particles. However, instead of following the same pathway as the first trajectory, this largest cluster shrinks in size and decays to a

cluster size of 5%. This pattern repeats itself twice more for this trajectory, where rather than growing to a system-spanning network, the cluster instead rises and then decays in size centered around $t = 1200$ and 1700. At the end of the simulation, the largest cluster only contains 20% of all elementary particles, significantly less than the other two trajectories.

Trajectory 3 falls somewhere between these two extremes, where after the rapid increase in size to contain 30% of elementary particles at 850 t, the cluster decays and then grows to a system spanning network by $t = 1250$.

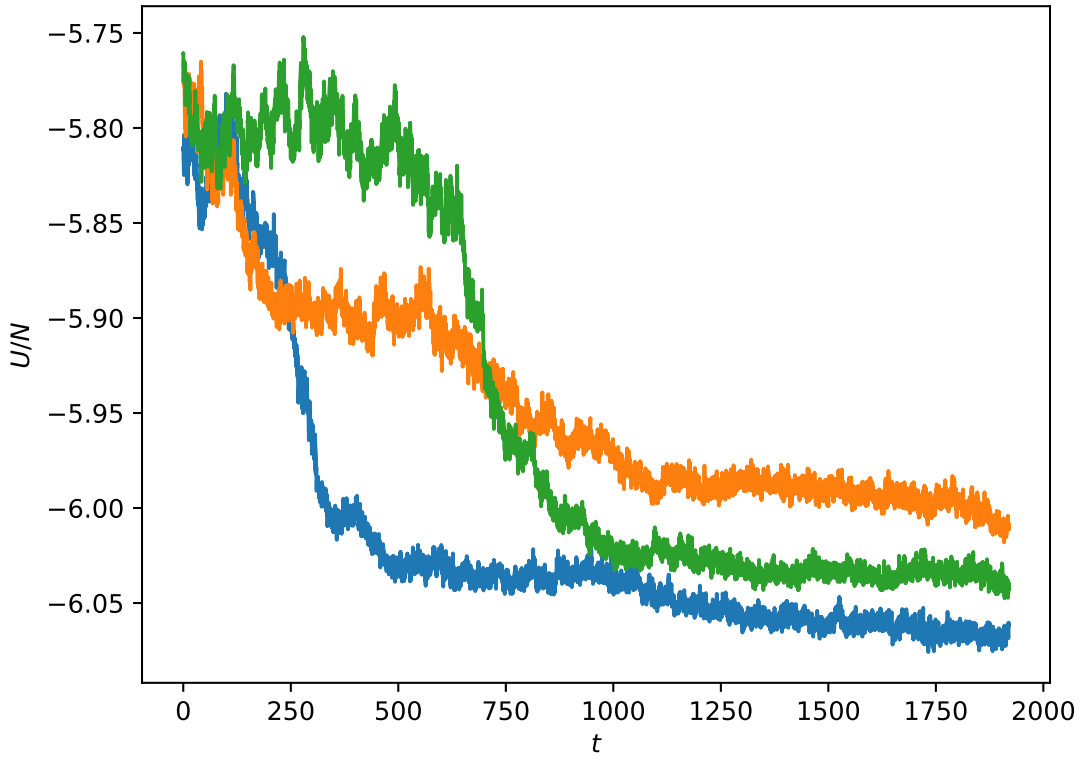

Figure 6.3: Evolution of the potential energy of a system of $N = 864$ triblock patchy particles along three independent dynamical trajectories at $T^* = 0.15, \phi = 0.3$. The blue plot shows the trajectory for which the radial distribution functions are plotted in figure 6.2. The potential energy shown here is a moving average over 500 snapshots of the instantaneous energy, where the value plotted is the average of the previous 249 and next 250 energies.

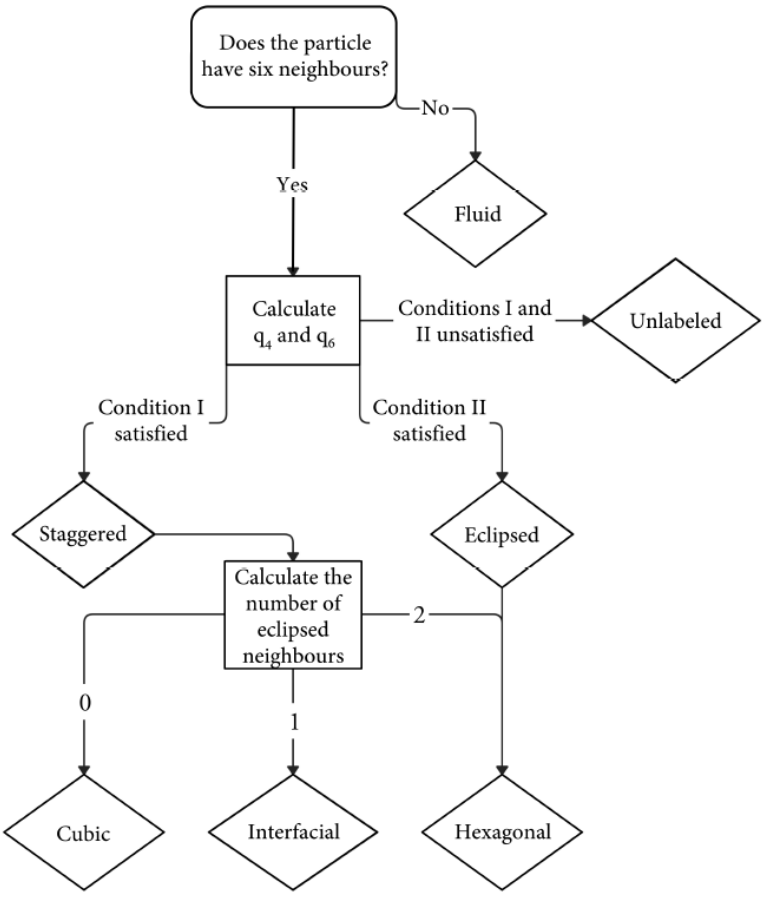

Figure 6.4: Decision tree for tetrastack polymorph identification based on two conditions; Condition I: $0.32 < q_4 < 0.43$ and $0.65 < q_6 < 0.83$ and Condition II: $0.13 < q_4 < 0.23$ and $0.35 < q_6 < 0.47$. This scheme was developed in collaboration with Andreas Neophytou and Dwaipayan Chakrabarti.

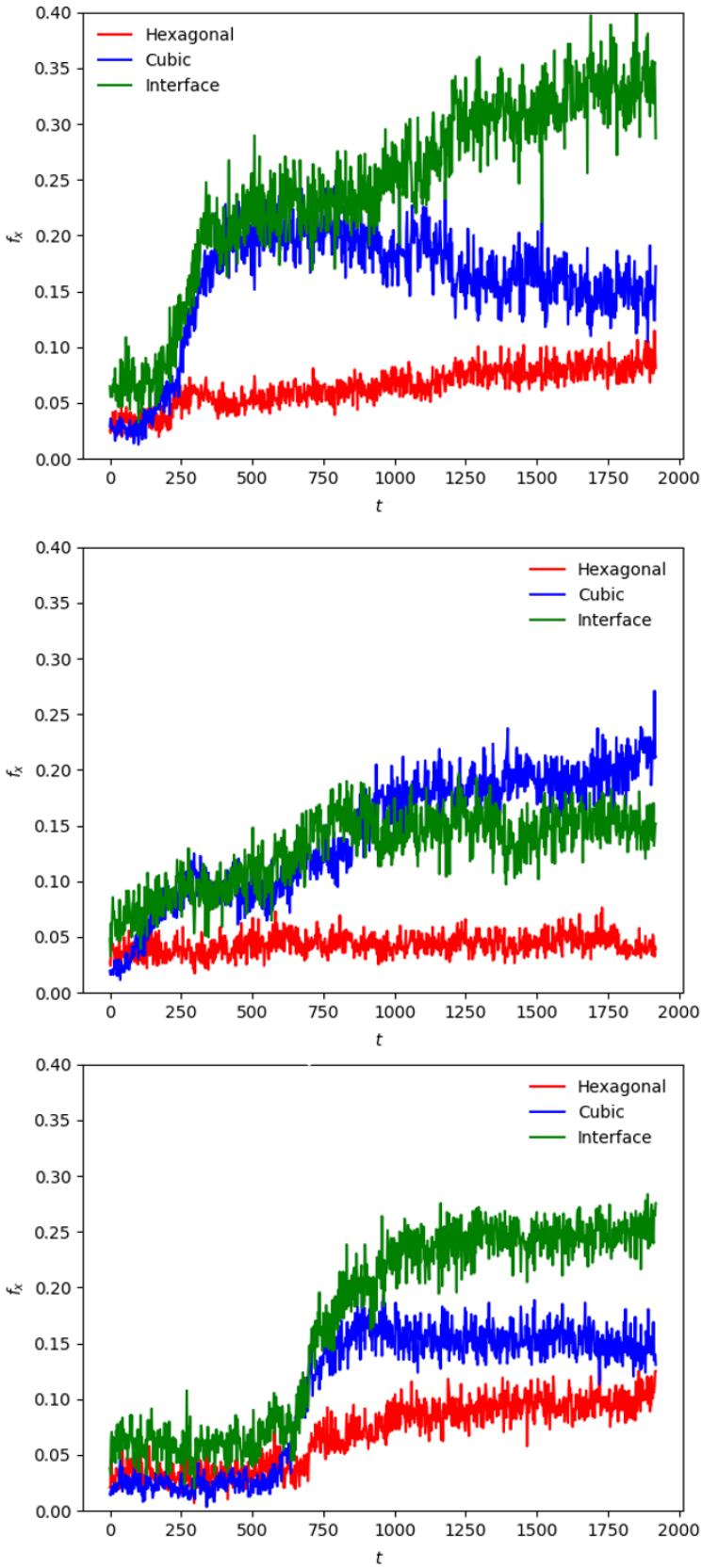

Figure 6.5: Compositions of the self-assembled crystal structures obtained for three dynamical trajectories shown in figure 6.3. Trajectory 1 (top) and 3 (bottom) follow similar pathways while trajectory 2 follows a much slower growth, but clearly develops a bias towards one polymorph over the other.

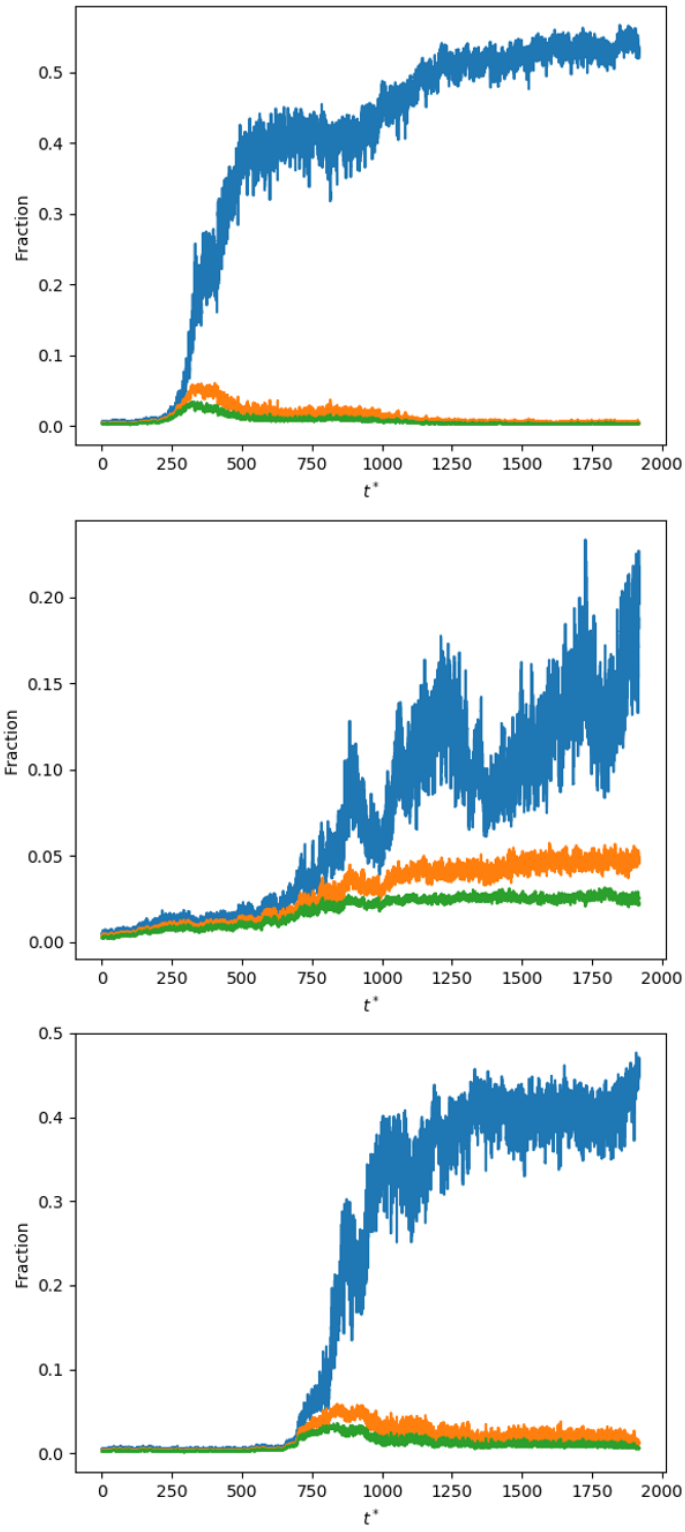

Figure 6.6: The size of the three largest clusters of elementary particles identified in any crystalline (cubic, hexagonal or interfacial) environment for dynamical trajectories 1-3, top-bottom. The clustering is based on distance cutoff of 1.2 σ for elementary particles identified as hexagonal, cubic or interfacial. The pathways shown for trajectories 1 and 3 suggest single nucleation and growth, while trajectory 2 does not grow steadily, with the size of the largest cluster fluctuating.

6.5 Simulation Size Effects

As well as performing the Brownian dynamics simulations for 864 particles, we investigated the nucleation and growth of $N = 4000$ triblock patchy particles into tetrastack via tetrahedral colloidal molecules. This system follows the same annealing protocol as detailed in chapter 5 for $N = 864$. We performed 4 simulations starting from an equilibrated melt of an FCC lattice.

The potential energy and number of tetrahedra as the temperature of the system is lowered for one trajectory is shown in figure 6.7. Here we can see that the plot takes the same form as those shown in chapter 5 where we observe multiple stages, initially forming roughly 1000 tetrahedra then going on to form a larger number. However, for this system we see much fewer tetrahedra forming in the second stage of assembly, and when we compare the radial distribution functions from the centres of tetrahedra in figure 6.8 we can see that we clearly have not reached a crystalline state for the larger particle simulations. We note that the average energy per particle for the N = 4000 system remains around -5.8 ϵ_Y, while the crystalline N = 864 systems all finish below -6 ϵ_Y. Even when we attempt to under-cool the system by dropping the temperature further, we still do not see any signs of crystallisation. For the 4 trajectories we followed after 460 t we lowered the temperature from $T^* = 0.15$ to $T^* = 0.145$ to promote the formation of the second stage of assembly by relatively strengthening the weaker bonds. We ran these simulations in parallel to the ones at $T^*0.15$ and show the plot of potential energy in figure 6.9. We show these under-cooled simulations with dashed lines in the same colour as the simulations that they take their starting configurations from. In this plot we can see that the average energy per particle does fall as time is evolved, particularly for the configuration shown in blue, but that this energy does not reach the -6 ϵ_Y we observe for the $N = 864$ simulations which have crystallised.

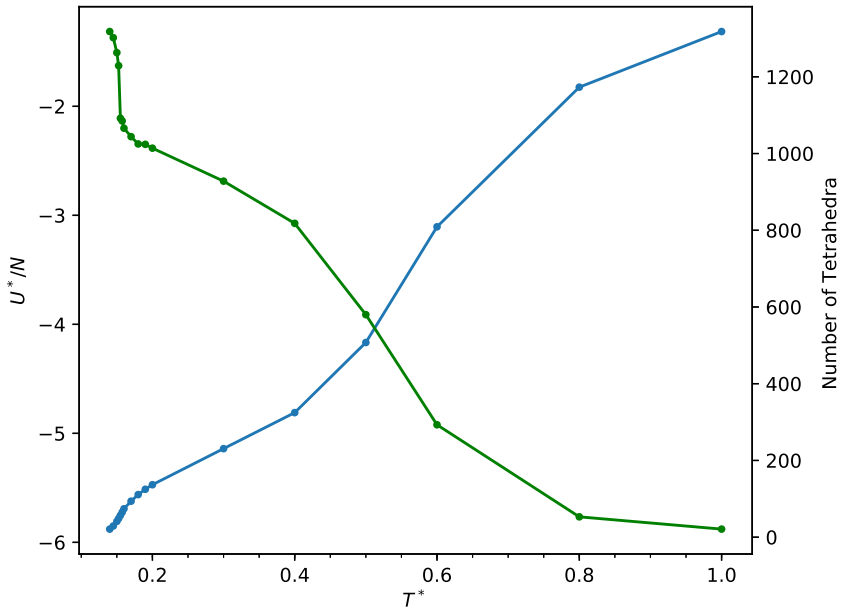

Figure 6.7: Potential energy and number of tetrahedra against temperature for $N = 4000$. Whilst it shows the same characteristics as $N = 864$, the system does not crystallise into a tetrastack lattice.

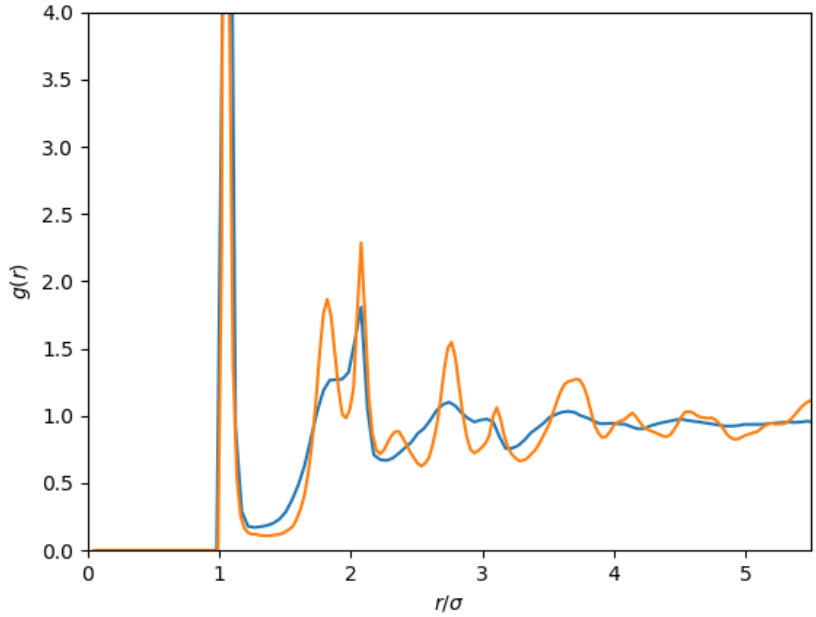

Figure 6.8: Radial distribution function for $N = 864$ (orange) and $N = 4000$ (blue) at $T^* = 0.15$ after $t = 2000$ and 800 respectively. The low intensity of peaks beyond $r = 2$ suggests the system is not crystalline.

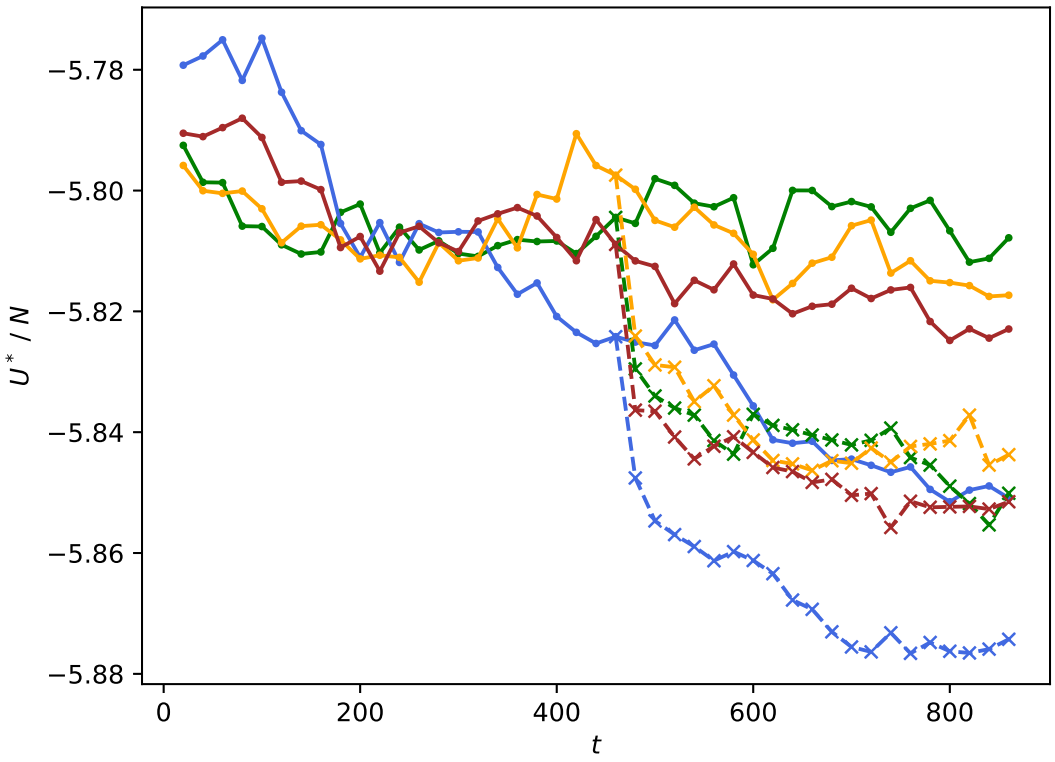

Figure 6.9: Average energy per particle for four trajectories at $N = 4000$ at $T^* = 0.15$. Despite the long simulation time, we do not observe crystallisation throughout these simulations. Under-cooling trajectories are shown with dashed lines where the configuration was dropped in temperature to $T^* = 0.145$ and run in parallel, but still did not reach crystallisation.

6.6 Conclusion

In this chapter, we have investigated the two-stage self-assembly pathways to the tetrastack crystal, which we devised in the previous chapter, in some detail from the perspective of polymorph selection. We observed two distinct crystallisation pathways, one with the nucleation and steady growth of a single large crystalline cluster into a mixed phase of cubic and hexagonal tetrastack with a slight preference towards the cubic environment, and a second pathway, which followed a much slower nucleation process involving the formation of multiple nuclei, many of which were relatively short lived and did not grow enough. We note that this second pathway, observed for trajectory 2, shows a much greater bias towards the cubic polymorph than the hexagonal, with the relative ratio of 4:1 in contrast to comparable proportions of particles locally in cubic and hexagonal environments found for trajectories 1 and 3. It would be of interest to calculate the free-energy barriers for the second stage of assembly in order to glean further mechanistic understanding.

Our analysis would have been much more insightful if we observed crystallisation along the dynamical trajectories simulated for a system of $N = 4000$ triblock patchy particles. Despite our sustained efforts, including under-cooling the system past the temperature at which crystallisation occurred for the system size of $N = 864$, we have not observed crystallisation along these trajectories yet. The relatively short-ranged interactions between patches driving the second stage of self-assembly, as compared to the ones at play with octahedral colloidal molecules studied in Chapter 4, is a likely contributing factor here. Typically (though not exclusively [158, 159]) periodic boundary conditions cause deviations from bulk properties where long-range interaction potentials are used[160, 122], introducing the possibility of particles interacting with themselves or influencing the dynamics of their neighbours - this is not the case

here, where the range of the potential is significantly smaller than the simulation box length. Were longer simulation times feasible, we could test the applicability of Clarke's observation [160] that faster quenching rates used for small samples are equivalent to much slower cooling rates for macroscopic samples. Simulations could also be run in a truncated octahedron or rhombic dodecahedron [122] to investigate the affect of running the simulation in a cubic box.

Chapter 7

Conclusions and Further Work

7.1 Summary

The overall aim of the present thesis was to investigate the versatility of a hierarchical self-assembly scheme encoded in triblock patchy particles in order to form a variety of colloidal open crystals via distinct colloidal molecules. Self-assembly lends itself to targeting open crystals which are inaccessible from traditional top-down approaches. The flexibility available in synthetically realisable triblock patchy particles through patch size, strength and interaction range manipulation provides a wide design space for hierarchical building blocks. By targeting open crystals with interesting optical and mechanical properties, we provide insight into the formation of said crystals through colloidal molecules formed through multiple stages of self-assembly. The task of encoding the appropriate information in the elementary building blocks in order to tackle the challenges arising from multiple time- and length-scales along the two-stage assemblies presented here required the investigation of stable structures as well as navigation of the kinetic pathways.

In **Chapter 3** we detailed the search for colloidal crystals through two-stage assem-

bly, via self-assembled octahedral building blocks. We identified a set of parameters supporting the self-limiting growth of octahedral colloidal molecules in the first stage, where a relatively wide patch size, $\alpha = 85^o$, was able to accommodate up to 5 bonding interactions. By incorporating a significant energy penalty for bonding to the weaker patch we promote the saturation of strong-strong bonds. By designing the weaker patch with a much narrower patch, $\beta = 40^o$, we are able to drive the second stage of assembly to occur by accommodating only a single weak-weak bond, while the geometry of the colloidal molecule assembled in the first stage of assembly dictates the long-range structure adapted by these octahedra yielding a BCC crystal.

Having established two-stage self-assembly pathways for our designer triblock patchy particles via octahedral colloidal molecules, in **Chapter 4** we apply this design route to the targeted growth of a simple cubic crystal. In this chapter, we explored and identified the the phase space that favours the growth of an open lattice. At lower volume fractions, the two-stage self-assembly pathways yielded a simple cubic lattice, in which the coordination number is less as compared to a BCC crystal.

In **Chapter 5** we discussed the targeted assembly of the tetrastack crystal through self-assembled tetrahedral building blocks. Building on earlier work performed by Chakrabarti and co-workers, we devised a two-stage self-assembly route to tetrastack crystals, relying upon the assembly of tetrahedral colloidal molecules in the first stage in a self-limiting manner [79]. Through a patch strength hierarchy of $\epsilon_A = 5\epsilon_B$, once these tetrahedra are formed the second stage of assembly is triggered in which the tetrahedra assemble onto a tetrastack lattice. We highlighted the importance of the patch strength hierarchy by comparing the crystalline growth with non-hierarchy routes where the strength of both patches were equal, which did not lead to crystallisation. Through an application of graph theory enabling cycle analysis, the two-stage assembly

route was observed to promote crystallisation, suppressing the formation of 5- and 7-membered rings as opposed to 6- and 8-membered rings present in the perfect crystals.

Finally, in **Chapter 6** we investigated whether the hierarchical self-assembly pathways that we devised to yield the tetrastack crystal would promote any bias towards the cubic or the hexagonal polymorph. To this end, a prescription for analysing the configurations to distinguish between the local environments in these polymorphs was devised, using the Steinhardt bond order parameters. Our observations revealed that a bias towards one polymorph could develop depending upon the crystallisation pathway followed; in particular, slow crystallisation appeared to promote a bias towards the cubic polymorph, which was known to be slightly more stable polymorph for a related model. However, we did not observe selection of any polymorph exclusively. The work contained within this thesis has contributed towards the publication of two papers [79, 153] in a high impact journal, showcasing the significance of this work, and provides a framework for the investigation of other open crystals and hierarchical self-assembly.

7.2 Outlook

Perovskite structures are of potential interest for numerous applications due to the wide range of functional properties they exhibit. The perovskite framework can be considered as vertex sharing octahedra; we therefore envisage that the hierarchical self-assembly scheme presented in this thesis for the formation of crystal structures via octahedral colloidal molecules could be exploited, by the widening of the second patch.

In the present body of work, we have throughout used the Steinhardt bond order parameters to identify transitions between fluid and crystalline phases and distinguish between local crystalline environments. Whilst these order parameters work well for

close-packed crystals, it is apparent that the introduction of thermal fluctuations can introduce issues when using a fixed-distance cutoff and significant adaptation is required to identify open crystals, as shown in chapters 4 and 6. In fact, the appropriate choice of order parameter and the selection of neighbours and cutoffs has been described as more of an art, than a science [161]. Rather than manually calculating appropriate ranges for order parameters, an alternative approach could involve the application of machine learning techniques to identify local environments [162]. Through unsupervised learning, a number of crystalline matter of interest can be given to a model to train, through which the neural network will identify key descriptors to characterise the local environment of the particles. Further investigations to develop such an approach are expected to offer new insights into distinguishing various crystal polymorphs effectively and characterising early stages of nucleation.

The development of the software simulation package `PASSION` from serial to OpenMPI-compliant code has opened up the possibility to investigate much larger system sizes in a realistic timeframe, as seen in chapter 4 where we were able to investigate nearly 9000 elementary particles through multiple stages of hierarchical assembly. There is, however, still scope for further development. Machine learning has prompted an explosion of innovation in graphics card programming, with the development of Fortran interfaces to the CUDA language opening the door to exploit code that runs on graphical processing units (GPUs) with thousands of cores. An adaptation of `PASSION` to utilise modern GPU hardware could massively expand the number of particles that can be simulated in realistic timeframes or allow simulations to probe much further along the trajectory for current system sizes, e.g. $N = 4000$.

This thesis has investigated designer spherical triblock patchy particles, incorporating a hierarchy of interaction strengths. Here highly directional interactions between

the particles arise from surface chemistry. However, there is much scope further investigations, including shape anisotropy [8]. For example, colloidal rods that can accommodate patches could provide an exciting new route to control porosity of colloidal open crystals [163]. Finally, building on the present body of work, a pursuit for bottom-up routes to multilevel structural hierarchy would be a worthwhile exercise.

Bibliography

[1] T Graham. X. Liquid Diffusion applied to Analysis. *Philosophical Transactions of the Royal Society London*, 151:183–224, 1861.

[2] A Gautieri, S Vesentini, A Redaelli, and M J Buehler. Hierarchical structure and nanomechanics of collagen microfibrils from the atomistic scale up. *Nano Letters*, 11(2):757–766, 2011.

[3] G M Whitesides and B Grzybowski. Self-assembly at all scales. *Science (New York, N.Y.)*, 295(5564):2418–21, 2002.

[4] S Zhang. Fabrication of novel biomaterials through molecular self-assembly. *Nature Biotechnology*, 21:1171–1178, 2003.

[5] L Cademartiri and K J M Bishop. Programmable self-assembly. *Nature Materials*, 14(1):2–9, 2015.

[6] D Wang and H Möhwald. Template-directed colloidal self-assembly -the route to ' top-down' nanochemical engineering. *Journal of Materials Chemistry*, pages 459–468, 2004.

[7] G M Whitesides and B Grzybowski. Beyond molecules: Self-assembly of mesoscopic and macroscopic components. *Proceedings of the National Academy of Sciences of the USA*, 99:4769, 2002.

[8] S C Glotzer and M J Solomon. Anisotropy of building blocks and their assembly into complex structures. *Nature materials*, 6(8):557–62, 2007.

[9] J Zhang, E Luijten, and S Granick. Toward design rules of directional janus colloidal assembly. *Annual Review of Physical Chemistry*, 66:581–600, 2015.

[10] A Einstein. Über die von der molekularkinetischen Theorie der Wärme geforderte Bewegung von in ruhenden Flüssigkeiten suspendierten Teilchen. *Annalen der Physik*, 322(8):549–560, 1905.

[11] J Perrin. *Brownian movement and molecular reality*. London: Taylor and Francis, 1909.

[12] W Poon. Colloids as Big Atoms. *Science*, 304(5672):830–831, 2004.

[13] P N Pusey and W van Megen. Phase behaviour of concentrated suspensions of nearly hard colloidal spheres. *Nature*, 320(6060):340–342, 1986.

[14] E R Weeks, J C Crocker, A C Levitt, A Schofield, and D A Weitz. Three-Dimensional Direct Imaging of Structural Relaxation Near the Colloidal Glass Transition. *Science*, 287(5453):627–631, 2000.

[15] U Gasser, E R Weeks, A Schofield, P N Pusey, and D A Weitz. Real-Space Imaging of Nucleation and Growth in Colloidal Crystallization. *Science*, 292(5515), 2001.

[16] V J Anderson and H N W Lekkerkerker. Insights into phase transition kinetics from colloid science. *Nature*, 416(6883):811–815, 2002.

[17] C P Royall, S R Williams, T Ohtsuka, and H Tanaka. Direct observation of a local structural mechanism for dynamic arrest. *Nature Materials*, 7(7):556–561, 2008.

[18] B J Alder and T E Wainwright. Phase Transition for a Hard Sphere System. *The Journal of Chemical Physics*, 27(5):1208–1209, 1957.

[19] W W Wood and J D Jacobson. Preliminary Results from a Recalculation of the Monte Carlo Equation of State of Hard Spheres. *The Journal of Chemical Physics*, 27(5):1207–1208, 1957.

[20] D Frenkel. Entropy-driven phase transitions. *Physica A*, 263:26–38, 1999.

[21] L Onsager. The Effects of Shape on the Interaction of Colloidal Particles. *Annals of the New York Academy of Sciences*, 51:627–659, 1949.

[22] P B Bolhuis, D Frenkel, S Mau, and D Huse. Entropy difference between crystal phases. *Nature*, 385:235–237, 1997.

[23] P N Pusey, W van Megen, P Bartlett, B J Ackerson, J G Rarity, and S M Underwood. Structure of crystals of hard colloidal spheres. *Physical Review Letters*, 63:2753, 1989.

[24] S Auer and D Frenkel. Prediction of absolute crystal-nucleation rate in hard-sphere colloids. *Nature*, 409(6823):1020–1023, 2001.

[25] W Ostwald. Studien über die Bildung und Umwandlung fester Körper. *Zeitschrift für Physikalische Chemie*, 22:289–330, 1897.

[26] R B Jones and P N Pusey. Dynamics of Suspended Colloidal Spheres. *Annual Review of Physical Chemistry*, 42(1):137–169, 1991.

[27] J L Harland and W van Megen. Crystallization kinetics of suspensions of hard colloidal spheres. *Physical Review E*, 55(3):3054–3067, 1997.

[28] P Tan, N Xu, and L Xu. Visualizing kinetic pathways of homogeneous nucleation in colloidal crystallization. *Nature Physics*, 10(1):73–79, 2014.

[29] C P Royall, W C K Poon, and E R Weeks. In search of colloidal hard spheres, 2013.

[30] M E Leunissen, C G Christova, A P Hynninen, C P Royall, A I Campbell, A Imhof, M Dijkstra, R Van Roij, and A Van Blaaderen. Ionic colloidal crystals of oppositely charged particles. *Nature*, 437(7056):235–240, 2005.

[31] A van Blaaderen. CHEMISTRY: Colloidal Molecules and Beyond. *Science*, 301(5632):470–471, 2003.

[32] V N Manoharan, M T Elsesser, and D J Pine. Dense packing and symmetry in small clusters of microspheres. *Science*, 301(5632):483–7, 2003.

[33] A Malins, S R Williams, J Eggers, H Tanaka, and C P Royall. Geometric frustration in small colloidal clusters. *Journal of Physics Condensed Matter*, 21(42):425103, 2009.

[34] G Meng, N Arkus, M P Brenner, and V N Manoharan. The free-energy landscape of clusters of attractive hard spheres. *Science*, 327(5965):560–3, 2010.

[35] C L Klix, K-I Murata, H Tanaka, S R Williams, A Malins, and C P Royall. Novel kinetic trapping in charged colloidal clusters due to self-induced surface charge organization. *Scientific Reports*, 3:2072, 2013.

[36] R W Perry, M C Holmes-Cerfon, M P Brenner, and V N Manoharan. Two-Dimensional Clusters of Colloidal Spheres: Ground States, Excited States, and Structural Rearrangements. *Physical Review Letters*, 114(22):228301, 2015.

[37] D J Wales. Energy landscapes of clusters bound by short-ranged potentials. *Chemphyschem*, 11(12):2491–4, 2010.

[38] D J Kraft, W S Vlug, C M van Kats, A van Blaaderen, A Imhof, and W K Kegel. Self-Assembly of Colloids with Liquid Protrusions. *Journal of the American Chemical Society*, 131(3):1182–1186, 2009.

[39] S Jiang S Granick and Q Chen. Janus particles. *Physics Today*, 62:68–69, 2009.

[40] L Hong, A Cacciuto, E Luijten, and S Granick. Clusters of amphiphilic colloidal spheres. *Langmuir*, 24(3):621–5, 2008.

[41] Q Chen, J K Whitmer, S Jiang, S C Bae, E Luijten, and S Granick. Supracolloidal Reaction Kinetics of Janus Spheres. *Science*, 331(6014):199–202, 2011.

[42] Y Wang, Y Wang, D R Breed, V N Manoharan, L Feng, A D Hollingsworth, M Weck, and D J Pine. Colloids with valence and specific directional bonding. *Nature*, 491(7422):51–5, 2012.

[43] J T McGinley, Y Wang, I C Jenkins, T Sinno, and J C Crocker. Crystal-Templated Colloidal Clusters Exhibit Directional DNA Interactions. *ACS Nano*, 9(11):10817–10825, 2015.

[44] M E Cates. Patchy colloids: Entropy stabilizes open crystals. *Nature Materials*, 12(3):179–180, 2013.

[45] J D Joannopoulos, P R Villeneuve, and S Fan. Photonic crystals: Putting a new twist on light, 1997.

[46] K Aryana and M B Zanjani. Diamond family of colloidal supercrystals as phononic metamaterials. *Journal of Applied Physics*, 123:185103, 2018.

[47] X Mao and T C Lubensky. Maxwell lattices and topological mechanics. *Annual Review of Condensed Matter Physics*, 9:413–433, 2018.

[48] G von Freymann, V Kitaev, B V Lotsch, and G A Ozin. Bottom-up assembly of photonic crystals. *Chemical Society Reviews*, 42(7):2528–2554, 2013.

[49] K M Ho, C T Chan, and C M Soukoulis. Existence of a photonic gap in periodic dielectric structures. *Physical Review Letters*, 65(25):3152–3155, 1990.

[50] T T Ngo, C M Liddell, M Ghebrebrhan, and J D Joannopoulos. Tetrastack: Colloidal diamond-inspired structure with omnidirectional photonic band gap for low refractive index contrast. *Applied Physics Letters*, 88(24), 2006.

[51] G A Ozin, K Hou, B V Lotsch, L Cademartiri, D P Puzzo, F Scotognella, A Ghadimi, and J Thomson. Nanofabrication by self-assembly. *Materials Today*, 12(5):12–23, 2009.

[52] J C Maxwell. On the calculation of the equilibrium and stiffness of frames. *The London, Edinburgh, and Dublin Philosophical Magazine and Journal of Science*, 27(182):294–299, 1864.

[53] S Chen, Z L Wang, J Ballato, S H Foulger, and D L Carroll. Monopod, Bipod, Tripod, and Tetrapod Gold Nanocrystals. *Journal of the American Chemical Society*, 125(52):16186–16187, 2003.

[54] Y Sun and Y Xia. Shape-controlled synthesis of gold and silver nanoparticles. *Science*, 298(5601):2176–2179, 2002.

[55] M Marechal, U Zimmermann, and H Löwen. Freezing of parallel hard cubes with rounded edges. *Journal of Chemical Physics*, 136(14):144506, 2012.

[56] L Rossi, S Sacanna, W T M Irvine, P M Chaikin, D J Pine, and A P Philipse. Cubic crystals from cubic colloids. *Soft Matter*, 7(9):4139–4142, 2011.

[57] Z Zhang and S C Glotzer. Self-assembly of patchy particles. *Nano Letters*, 44:1407–1413, 2004.

[58] Z Zhang, A S Keys, T Chen, and S C Glotzer. Self-assembly of patchy particles into diamond structures through molecular mimicry. *Langmuir*, 21(25):11547–11551, 2005.

[59] E G Noya, C Vega, J P K Doye, and A A Louis. The stability of a crystal with diamond structure for patchy particles with tetrahedral symmetry. *Journal of Chemical Physics*, 132(23), 2010.

[60] F Romano, E Sanz, and F Sciortino. Crystallization of tetrahedral patchy particles in silico. *Journal of Chemical Physics*, 134(17), 2011.

[61] Q Chen, S C Bae, and S Granick. Directed self-assembly of a colloidal kagome lattice. *Nature*, 469(7330):381–384, 2011.

[62] A B Pawar and I Kretzschmar. Fabrication, assembly, and application of patchy particles. *Macromolecular Rapid Communications*, 31(2):150–68, 2010.

[63] F Romano and F Sciortino. Two dimensional assembly of triblock janus particles into crystal phases in the two bond per patch limit. *Soft Matter*, 7:5799–5804, 2011.

[64] X Mao, Q Chen, and S Granick. Entropy favours open colloidal lattices. *Nature materials*, 12(3):217–22, 2013.

[65] T Vissers, Z Preisler, F Smallenburg, M Dijkstra, and F Sciortino. Predicting crystals of Janus colloids. *The Journal of Chemical Physics*, 138(16):164505, 2013.

[66] W F Reinhart and A Z Panagiotopoulos. Equilibrium crystal phases of triblock Janus colloids. *The Journal of Chemical Physics*, 145(9):094505, 2016.

[67] F Romano and F Sciortino. Patterning symmetry in the rational design of colloidal crystals. *Nature Communications*, 3(1):975, 2012.

[68] M B Zanjani, I C Jenkins, J C Crocker, and T Sinno. Colloidal Cluster Assembly into Ordered Superstructures via Engineered Directional Binding. *ACS Nano*, 10(12):11280–11289, 2016.

[69] K Miszta, J De Graaf, G Bertoni, D Dorfs, R Brescia, S Marras, L Ceseracciu, R Cingolani, R Van Roij, M Dijkstra, and L Manna. Hierarchical self-assembly of suspended branched colloidal nanocrystals into superlattice structures. *Nature Materials*, 10(11):872–876, 2011.

[70] S Deka, K Miszta, D Dorfs, A Genovese, G Bertoni, and L Manna. Octapod-shaped colloidal nanocrystals of cadmium chalcogenides via "one-Pot" cation exchange and seeded growth. *Nano Letters*, 10(9):3770–3776, 2010.

[71] A Gröschel, F Schacher, H Schmalz, O Borisov, E Zhulina, A Walther, and A Müller. Precise hierarchical self-assembly of multicompartment micelles. *Nature Communications*, 3(1):1–10, 2012.

[72] Y Ma and A L Ferguson. Inverse design of self-Assembling colloidal crystals with omnidirectional photonic bandgaps. *Soft Matter*, 15(43):8808–8826, 2019.

[73] Q Chen, E Diesel, J K Whitmer, S C Bae, E Luijten, and S Granick. Triblock Colloids for Directed Self-Assembly. *Journal of the American Chemical Society*, 133(20):7725–7727, 2011.

[74] Q Chen, S C Bae, and S Granick. Staged self-assembly of colloidal metastructures. *Journal of the American Chemical Society*, 134:11080–11083, 2012.

[75] M Grünwald and P L Geissler. Patterns without patches: hierarchical self-assembly of complex structures from simple building blocks. *ACS nano*, 8(6):5891–7, 2014.

[76] D Morphew and D Chakrabarti. Hierarchical self-assembly of colloidal magnetic particles into reconfigurable spherical structures. *Nanoscale*, 7(18):8343–8350, 2015.

[77] D Morphew and D Chakrabarti. Supracolloidal reconfigurable polyhedra via hierarchical self-assembly. *Soft Matter*, 12:9633–9640, 2016.

[78] D Morphew and D Chakrabarti. Programming hierarchical self-assembly of colloids: matching stability and accessibility. *Nanoscale*, 10(29):13875–13882, 2018.

[79] D Morphew, J Shaw, C Avins, and D Chakrabarti. Programming Hierarchical Self-Assembly of Patchy Particles into Colloidal Crystals via Colloidal Molecules. *ACS Nano*, 12(3):2355–2364, 2018.

[80] D Frenkel and D J Wales. Design Principles for Self-Assembling Colloids. *Nature Materials*, 10(6):410–411, 2011.

[81] R Brown. A brief account of microscopical observations made in the months of June, July and August 1827, on the particles contained in the pollen of plants; and on the general existence of active molecules in organic and inorganic bodies . *Philosophical Magazine Series 2*, 4(21):161–173, 1828.

[82] B V Derjaguin and L D Landau. Acta Physicochimica. *URSS*, 14:633, 1941.

[83] E J W Verwey and J T G Overbeek. Theory of the stability of lyophobic colloids. *The Journal of Physical Chemistry*, 51(3):631–636, 1947.

[84] S Asakura and F Oosawa. On Interaction between Two Bodies Immersed in a Solution of Macromolecules. *The Journal of Chemical Physics*, 22(7):1255–1256, 1954.

[85] N Kern and D Frenkel. Fluid–fluid coexistence in colloidal systems with short-ranged strongly directional attraction. *The Journal of Chemical Physics*, 118(21):9882–9889, 2003.

[86] G Trefalt and M Borkovec. Overview of DLVO theory, 2014.

[87] K Binder, P Virnau, and A Statt. Perspective: The Asakura Oosawa model: a colloid prototype for bulk and interfacial phase behavior. *The Journal of Chemical Physics*, 141(14):140901, 2014.

[88] M F Hagan R L Jack and D Chandler. Fluctuation-dissipation ratios in the dynamics of self-assembly. *Physical Review E - Statistical, Nonlinear, and Soft Matter Physics*, 76(2):021119, 2007.

[89] R L Jack D Klotsa. Predicting the self-assembly of a model colloidal crystal. *Soft Matter*, 7(13):6294–6303, 2011.

[90] D C Rapaport. Role of reversibility in viral capsid growth: A paradigm for self-assembly. *Physical Review Letters*, 101(18), 2008.

[91] M F Hagan and D Chandler. Dynamic pathways for viral capsid assembly. *Biophysical Journal*, 91(1):42–54, 2006.

[92] R Zwanzig. *Nonequilibrium Statistical Mechanics* . Oxford University Press, 2001.

[93] D Klotsa and R L Jack. Controlling crystal self-assembly using a real-time feedback scheme. *Journal of Chemical Physics*, 138(9):094502, 2013.

[94] D Wales. *Energy Landscapes*. Cambridge University Press, 2004.

[95] C M Dobson, A Šali, and M Karplus. Protein Folding: A Perspective From Theory and Experiment. *Angewandte Chemie (International ed. in English)*, 37(7), 1998.

[96] V K de Souza and D J Wales. The potential energy landscape for crystallisation of a Lennard-Jones fluid. *Journal of Statistical Mechanics: Theory and Experiment*, 2016(7):074001, 2016.

[97] A Reinhardt and J P K Doye. Free energy landscapes for homogeneous nucleation of ice for a monatomic water model. *Journal of Chemical Physics*, 136(5):054501, 2012.

[98] O M Becker and M Karplus. The topology of multidimensional potential energy surfaces: Theory and application to peptide structure and kinetics. *The Journal of Chemical Physics*, 106(4):1495, 1997.

[99] D J Wales, M A Miller, and T R Walsh. Archetypal energy landscapes. 394(6695):758–760, 1998.

[100] R Radhakrishnan and B L Trout. Nucleation of Crystalline Phases of Water in Homogeneous and Inhomogeneous Environments. *Physical Review Letters*, 90(15):4, 2003.

[101] R Radhakrishnan and B L Trout. Nucleation of hexagonal ice (Ih) in liquid water. *Journal of the American Chemical Society*, 125(25):7743–7747, 2003.

[102] D Quigley and P M Rodger. Metadynamics simulations of ice nucleation and growth. *Journal of Chemical Physics*, 128(15):154518, 2008.

[103] D Frenkel and B Smit. *Understanding Molecular Simulation*. Elsevier, 2 edition, 2001.

[104] A Z Panagiotopoulos. Direct determination of phase coexistence properties of fluids by monte carlo simulation in a new ensemble. *Molecular Physics*, 61(4):813–826, 1987.

[105] D A Kofke. Gibbs-duhem integration: A new method for direct evaluation of phase coexistence by molecular simulation. *Molecular Physics*, 78(6):1331–1336, 1992.

[106] A-P Hynnien and A Z Panagiotopoulos. Phase diagrams of charged colloids from thermodynamic integration. *Journal of Physics: Condensed Matter*, 21(46), 2009.

[107] M Müller and K C Daoulas. Calculating the free energy of self-assembled structures by thermodynamic integration. *Journal of Chemical Physics*, 128(2):024903, 2008.

[108] M G Noro and D Frenkel. Extended corresponding-states behavior for particles with variable range attractions. *Journal of Chemical Physics*, 113(8):2941–2944, 2000.

[109] G Foffi and F Sciortino. On the possibility of extending the Noro-Frenkel generalized law of correspondent states to nonisotropic patchy interactions. *Journal of Physical Chemistry B*, 111(33):9702–9705, 2007.

[110] M S Wertheim. Fluids with highly directional attractive forces. I. Statistical thermodynamics. *Journal of Statistical Physics*, 35(1-2):19–34, 1984.

[111] J Taffs, S R Williams, H Tanaka, and C P Royall. Structure and kinetics in the freezing of nearly hard spheres. *Soft Matter*, 9(1):297–305, 2013.

[112] T Cosgrove. *Colloid Science Principles, methods and applications Second Edition.* 2010.

[113] S T Milner. Polymer brushes. *Science*, 251(4996):905–914, 1991.

[114] K J M Bishop, C E Wilmer, S Soh, and B A Grzybowski. Nanoscale Forces and Their Uses in Self-Assembly. *Small*, 5(14):1600–1630, 2009.

[115] Q Chang. *Colloid and Interface Chemistry for Water Quality Control.* Elsevier Inc., 2016.

[116] E Dickinson. Milk protein interfacial layers and the relationship to emulsion stability and rheology. *Colloids and Surfaces B: Biointerfaces*, 20(3):197–210, 2001.

[117] D J Shaw. *Introduction to Colloid and Surface Chemistry*. Butterworths, Liverpool, third edit edition, 1980.

[118] H Ohshima. Chapter 1 - Interaction of colloidal particles. In Hiroyuki Ohshima and Kimiko Makino, editors, *Colloid and Interface Science in Pharmaceutical Research and Development*, pages 1–28. Elsevier, Amsterdam, 2014.

[119] Y Monovoukas and A P Gast. The experimental phase diagram of charged colloidal suspensions. *Journal of Colloid And Interface Science*, 128(2):533–548, 1989.

[120] N Arkus, V N Manoharan, and M P Brenner. Minimal Energy Clusters of Hard Spheres with Short Range Attractions. *Physical Review Letters*, 103(11):118303, 2009.

[121] D Chakrabarti and D J Wales. Simulations of rigid bodies in an angle-axis framework. *Physical Chemistry Chemical Physics : PCCP*, 11(12):1970–6, 2009.

[122] M P Allen and D J Tildesley. *Computer Simulation of Liquids*. 1990.

[123] I Snook. *The Langevin and generalised Langevin approach to the dynamics of atomic, polymeric and colloidal systems*. Elsevier, 2006.

[124] N Heptner. *Dynamics and non-equilibrium structure of colloidal dumbbell-shaped particles in dense suspensions*. PhD thesis, 2016.

[125] D Chakrabarti. PaSSion - A Package for Soft Matter Simulation.

[126] D C Liu and J Nocedal. On the limited memory BFGS method for large scale optimization. *Mathematical Programming*, 45(1-3):503–528, 1989.

[127] D Morphew. *Programming Hierarchical Self-assembly of Anisotropic Colloids*. PhD thesis, University of Birmingham, 2018.

[128] J Shaw. UniVis - Unity-based Visualisation package.

[129] Persistence of Vision (TM) RayTracer, 2004.

[130] P J Steinhardt, D R Nelson, and M Ronchetti. Bond-orientational order in liquids and glasses. *Physical Review B*, 28(2):784–805, 1983.

[131] P R ten Wolde, M J Ruiz-Montero, and D Frenkel. Numerical Evidence for bcc Ordering at the Surface of a Critical fcc Nucleus. *Physical Review Letters*, 75(14):2714–2717, 1995.

[132] P R tenWolde, M J Ruiz-Montero, and D Frenkel. Numerical calculation of the rate of crystal nucleation in a Lennard-Jones system at moderate undercooling. *The Journal of Chemical Physics*, 104(24):9932, 1996.

[133] H Wang, H Gould, and W Klein. Homogeneous and heterogeneous nucleation of Lennard-Jones liquids. *Physical Review E - Statistical, Nonlinear, and Soft Matter Physics*, 76(3), 2007.

[134] W Mickel, S C Kapfer, G E Schroder-Turk, and K Mecke. Shortcomings of the bond orientational order parameters for the analysis of disordered particulate matter. *The Journal of Chemical Physics*, 138:044501, 2013.

[135] W Lechner and C Dellago. Accurate determination of crystal structures based on averaged local bond order parameters. *The Journal of Chemical Physics*, 129(11):114707, 2008.

[136] S Caravati, M Bernasconi, T D Kühne, M Krack, and M Parrinello. Coexistence of tetrahedral- and octahedral-like sites in amorphous phase change materials. *Applied Physics Letters*, 91(17):171906, 2007.

[137] D Morphew and D Chakrabarti. Clusters of anisotropic colloidal particles: From colloidal molecules to supracolloidal structures, 2017.

[138] J Russo and H Tanaka. Crystal nucleation as the ordering of multiple order parameters. *The Journal of Chemical Physics*, 145(21), 2016.

[139] H S Sözüer and J W Haus. Photonic bands: simple-cubic lattice. *Journal of the Optical Society of America B*, 10(2):296, 1993.

[140] S Matthias, R Hillebrand, F Müller, and U Gösele. Macroporous silicon: Homogeneity investigations and fabrication tolerances of a simple cubic three-dimensional photonic crystal. *Journal of Applied Physics*, 99(11):113102, 2006.

[141] K P Velikov, C G Christova, R P A Dullens, and A Van Blaaderen. Layer-by-layer growth of binary colloidal crystals. *Science (New York, N.Y.)*, 296(5565):106–9, 2002.

[142] J R Errington and P G Debenedetti. Relationship between structural order and the anomalies of liquid water. *Nature*, 409(6818):318–21, 2001.

[143] S Auer and D Frenkel. Quantitative Prediction Of Crystal-Nucleation Rates For Spherical Colloids: A Computational Approach. *Annual Review of Physical Chemistry*, 55(1):333–361, 2004.

[144] Z Zhang, A S Keys, T Chen, and S C Glotzer. Self-Assembly of Patchy Particles into Diamond Structures through Molecular Mimicry. *Nature materials*, 2005.

[145] P Rein ten Wolde and D Frenkel. Homogeneous nucleation and the Ostwald step rule. *Physical Chemistry Chemical Physics*, 1(9):2191–2196, 1999.

[146] M Maldovan, C K Ullal, W C Carter, and E L Thomas. Exploring for 3D photonic bandgap structures in the 11 f.c.c. space groups. *Nature Materials*, 2(10):664–667, 2003.

[147] A-P Hynninen, J H J Thijssen, E C M Vermolen, M Dijkstra, and A van Blaaderen. Self-assembly route for photonic crystals with a bandgap in the visible region. *Nature Materials*, 6(3):202–205, 2007.

[148] É Ducrot, M He, G R Yi, and D J Pine. Colloidal alloys with preassembled clusters and spheres. *Nature Materials*, 16(6):652–657, 2017.

[149] S Whitelam and R L Jack. The Statistical Mechanics of Dynamic Pathways to Self-Assembly. *Annual Review of Physical Chemistry*, 66(1):143–163, 2015.

[150] F Smallenburg and F Sciortino. Liquids more stable than crystals in particles with limited valence and flexible bonds. *Nature Physics*, 9(9):554–558, 2013.

[151] N A Mahynski, L Rovigatti, C N Likos, and A Z Panagiotopoulos. Bottom-Up Colloidal Crystal Assembly with a Twist. *ACS Nano*, 10(5):5459–5467, 2016.

[152] H Pattabhiraman, G Avvisati, and M Dijkstra. Novel Pyrochlorelike Crystal with a Photonic Band Gap Self-Assembled Using Colloids with a Simple Interaction Potential. *Physical Review Letters*, 119(15), 2017.

[153] A B Rao, J Shaw, A Neophytou, D Morphew, F Sciortino, R L Johnston, and D Chakrabarti. Leveraging Hierarchical Self-Assembly Pathways for Realizing Colloidal Photonic Crystals. *ACS Nano*, 14(5):5348–5359, 2020.

[154] J C Reepmeyer, M O Rhodes, D C Cox, and J V Silverton. Characterization and crystal structure of two polymorphic forms of racemic thalidomide. *Journal of the Chemical Society, Perkin Transactions 2*, 1(9):2063, 1994.

[155] T Bartels-Rausch, V Bergeron, J H E Cartwright, R Escribano, J L Finney, H Grothe, P J Gutiérrez, J Haapala, W F Kuhs, J B C Pettersson, S D Price, C I Sainz-Díaz, D J Stokes, G Strazzulla, E S Thomson, H Trinks, and N Uras-Aytemiz. Ice structures, patterns, and processes: A view across the icefields. *Reviews of Modern Physics*, 84(2):885–944, 2012.

[156] P G Vekilov. Nucleation. *Crystal Growth and Design*, 10:5007–5019, 2010.

[157] A Stukowski. OVITO User Manual, 2020.

[158] M J Mandell. On the properties of a periodic fluid. *Journal of Statistical Physics*, 15(4):299–305, 1976.

[159] L R Pratt and S W Haan. Effects of periodic boundary conditions on equilibrium properties of computer simulated fluids. II. Application to simple liquids. *The Journal of Chemical Physics*, 74(3):1873–1876, 1981.

[160] J H R Clarke. Molecular dynamics studies of glass formation in the Lennard-Jones model of argon. *Journal of the Chemical Society, Faraday Transactions 2: Molecular and Chemical Physics*, 75(0):1371–1387, 1979.

[161] J Sethana. *Statistical Mechanics: Entropy, Order Parameters, and Complexity — James Sethna*. Oxford University Press, 2006.

[162] C S Adorf, T C Moore, Y J U Melle, and S C Glotzer. Analysis of self-assembly pathways with unsupervised machine learning algorithms. *The Journal of Physical Chemistry B*, 124(1):69–78, 2020. PMID: 31813215.

[163] A Neophytou. *Hierarchical self-assembly of elongated patch colloids into photonic crystals* . PhD thesis, University of Birmingham, 2019.